Active deformation over multiple earthquake cycles in the southern Junggar fold and-thrust belt, NW China and fractured reservoir characterization using 3D geomechanical restorations

Citation

Stockmeyer, Joseph M. 2016. Active deformation over multiple earthquake cycles in the southern Junggar fold and-thrust belt, NW China and fractured reservoir characterization using 3D geomechanical restorations. Doctoral dissertation, Harvard University, Graduate School of Arts & Sciences.

Active deformation over multiple earthquake cycles in the southern Junggar fold-and-thrust belt, NW China and fractured reservoir characterization using 3D geomechanical restorations

A dissertation presented by

Joseph M. Stockmeyer

to

The Department of Earth and Planetary Sciences

in partial fulfillment of the requirements for the degree of

Doctor of Philosophy

in the subject of

Earth and Planetary Sciences

Harvard University

Cambridge, Massachusetts

April 2016

Advisor: Professor John H. Shaw Joseph M. Stockmeyer

Active deformation over multiple earthquake cycles in the southern Junggar fold-and-thrust belt, NW China and fractured reservoir characterization using 3D geomechanical restorations

Abstract

This dissertation investigates natural deformation processes over multiple earthquake cycles in the seismically active, southern Junggar basin, NW China and additionally explores the capabilities of 3D geomechanical restoration as an effective tool for fractured reservoir characterization. Chapter 1 presents a detailed 3D fault model of the active Southern Junggar Thrust (SJT) – constrained by seismic reflection data – in the southern Junggar basin. This work demonstrates the significance of mid-crustal detachments as a physical mechanism to accommodate destructive, multi-segment earthquakes in active thrust sheets. Moreover, it highlights the efficacy of surface folds to delineate fault geometries at depth in the absence of subsurface data constraints. Chapter 2 describes active thrust sheet deformation across the Tugulu anticline, which sits in the hanging wall of the SJT, from Late Quaternary to present. Holocene terrace deformation records of surface faulting and folding yield consistent fault slip rates. We develop a quantitative method for extracting fault slip rates from terrace fold geometries using a mechanical modeling approach, yielding a 250 kyr history of SJT slip. This study provides new insights into natural fold growth associated with fault slip. Moreover, it addresses several shortcomings of traditional seismic hazards assessment methodologies. Chapter 3 characterizes the styles, timing, and sequence of deformation across southern Junggar. Southern Junggar underwent extension followed by tectonic inversion and shortening, forming a series of imbricate structural wedges. A kinematic model for the evolution of shear fault-bend fold wedges is presented. We discuss the implications of structural style, fold growth and thrusting sequence on the ~175 Myr evolution of this fold-and-thrust belt and its petroleum system. Chapter 4 investigates the impact of natural fold strains on fractured reservoir properties in the Permian Basin, West Texas. This study details the ability of 3D geomechanical restorations to accurately model natural strain distributions associated with fold growth. Modeled strains from geomechanical restorations are integrated with proxies for natural deformation and production data to describe how tectonic strain impacted observed gas production, water cuts and reservoir temperatures. When used in conjunction with additional datasets, geomechanical restoration shows promise for predictive abilities in characterizing conventional and unconventional fractured reservoir properties.

Active deformation over multiple earthquake cycles in the southern Junggar fold and-thrust belt, NW China and fractured reservoir characterization using 3D geomechanical restorations

Acknowledgments

I express my sincere gratitude to my advisor, John Shaw. John's insights and guidance are spread throughout this thesis, which I could not have completed without. The experiences gained from my times with John over the past five years – at our workstations, in lecture halls and across the Kananaskis Valley – were many of the most rewarding aspects of my academic training, which I anticipate will remain with me throughout my professional career. I also thank my committee members – Brendan Meade and Jerry Mitrovica – for, at times, pushing me to extend my limits as a researcher, but mostly for their constant encouragement and engaging conversations. Andreas Plesch taught me the value of patience when working with 3D geologic models and provided his expertise for velocity and structural modeling throughout this work. Chapters 1-3 of this thesis could not have been completed without the support and collaborative efforts of Shuwei Guan. Similarly, Lee Billingsley made chapter 4 of this thesis possible, and I enjoyed working with Lee throughout those efforts.

I have had two additional mentors during my training as a structural geologist. Chris Guzofski oversaw my internship at Chevron Corporation in 2013 and collaborated on related projects in the following years. Chris remains remains a very good friend whom I hope to work with again in the near future. Chris Connors was my undergraduate research advisor at Washington and Lee University. His passion for structural and petroleum geology formed the foundations of my career aspirations. Chris is also responsible for me pursuing this PhD; I will forever be indebted to him for seeing the potential when I could not.

There are a number of additional individuals who have helped me in various capacities get to this point in my career. In particular, I am quite grateful for conversations, insight and opportunities provided by: Rick Vierbuchen, Bill Pritchard, Chris Whitten, Doug Goff, Kevin Doyle, Dave Houseknecht, Nathan Benesh, Lisa Greer, Jeff Rahl, Paul Low, Dave Harbor, Elizabeth Knapp, Alex Burpee, Nick Fox and David Howlett.

I had many great experiences at Harvard, most of which I attribute to my graduate student colleagues in the structure group: Kristian Bergen, Maomao Wang, Yanpeng Sun, Jessica Don, and

Benjamin Chauvin. Notable officemates also include Justin Strauss and Shublik, who both always encouraged the continued grind. Kevin Matthews was a great friend during graduate school, providing several technical (and some bizarre) energy system discussions after long nights at our respective offices. Tadd Hatcher provided much-needed industry-related conversations throughout and was a generous host during several visits to the great state of Texas.

I would not have written this thesis without the support of my family. Bob and Kelly Galvin welcomed me with open arms into their wonderful home and family, always making sure I took long overdue breaks from my office. Rena, Simon, Ed, Holly, Katie, Karla, Todd, Maggie and Milo were all in my thoughts throughout the past five years of my life, despite how it may have seemed by a lack of phone calls and emails. Throughout my life, my father, Bill, has been my primary source for wisdom and encouragement when it tackling the difficult and trying times of life; those lessons proved their value every single day I was at Harvard. I attribute any and all interest I have in science to my mother, Mary: in May 1994 my mother woke me up from nap time, signed me out of class and took me to watch a solar eclipse, a sight that forever sparked my interest in the world around me.

Most notably, however, during graduate school I was lucky enough to meet the love of my life, Meghan. Meghan's ability to always make me laugh was essential during times when research was not progressing. Her constant love and support – even if she didn't quite understand what I was doing all those hours – are two of her *many* qualities that allowed me to successfully complete this work, and do so proudly. I am blessed to have Meghan in my life.

for Meghan.

INTRODUCTION

This thesis integrates quantitative structural interpretations of geologic and geophysical datasets with forward models and restorations of natural structures to investigate the nature of deformation associated with fold growth and fault activity in Earth's upper, brittle crust. Better understanding of these deformational processes on both earthquake cycle and geologic timescales has a breadth of applications in structural geology, active tectonics, and resource characterization. The following chapters present studies investigating folding and related faulting strains in the context of regional tectonic studies, seismic hazards assessment, petroleum exploration and fractured reservoir characterization methodologies.

The destructive nature of convergent tectonics is manifest by large magnitude earthquakes that occur along subduction zones and within fold-and-thrust belts. Seismogenic faults in convergent margins pose some of the most significant natural hazards to human life and property. While the threats of subduction zone earthquakes are often well-appreciated, the hazards posed by ruptures in continental fold-and-thrust belts are often underestimated in regional hazard assessments. Contemporary events in these geologic settings (e.g. 1999 Mw 7.6 Chi-Chi, Taiwan; 2008 Mw 7.9 Wenchuan, China; 2015 M_w 7.8 Gorkha, Nepal) have led to tens of thousands of deaths and tens of billions of dollars in damage to infrastructure. Prior to such destructive events, earthquake hazards assessments attempt to quantify the activity of thrust faults, constraining paleo-event magnitudes, recurrence intervals between successive ruptures and fault slip rates. These often serve as the basis for estimating the size and potential timing of future earthquakes. Such assessments traditionally rely on surface ruptures to define fault activity, slip rates, and paleoearthquake magnitudes. As a result, assessments of past and future event magnitudes are often based on the lengths of surface fault traces, with large offsets between surface traces defining the limits of potential rupture patches. However, earthquakes in fold-and-thrust belts commonly involve rupture along multiple fault splays and breach lateral segment boundaries. These fault networks pose significant seismic hazards as they have the potential to produce large, multi-segment earthquakes. Traditional seismic hazards assessments methodologies have additionally relied on measures of slip along these surface ruptures to constrain paleoearthquake magnitude and total fault slip rates. However, deformation associated with thrust fault earthquakes can be multifaceted, often involving components of coseismic folding as well as coseismic faulting. In fact, many active thrust faults – or portions of these faults – are blind, such that surface deformation is characterized exclusively by folding. Thus, estimating fault slip rate and moment magnitude exclusively from uplift measures across surface ruptures will be inadequate if folding consumes a significant portion of the slip budget at depth. For blind faults and other structures with limited fault exposures, geologic folds provide the most direct means of constraining fault activity.

Addressing these challenges is critical to improving our ability to assess the seismic hazards in active fold-and-thrust belts and, thus, allow us to reduce the risk to life and property of future earthquakes. Moreover, deciphering the interplay of folding and faulting is central to our understanding of how geologic structures grow and accommodate shortening in the crust over multiple earthquake cycle timescales. To this end, the first two chapters of this dissertation investigate the complex nature of active thrust faulting and associated folding with case studies in the southern Junggar basin, NW China. In Chapter 1, we present methods to constrain 3D fault geometries and delineate mid-crustal detachments that may serve as a physical link at depth for highly segment surface fault splays, thereby enabling large (M_w ~8), multi-segment thrust fault earthquakes. We use 2D and 3D seismic reflection and seismicity data to build a 3D fault model of the Southern Junggar Thrust (SJT), a highly-segmented, active fault system that ruptured during the 1906 M_w ~8 Manas, China earthquake. Despite strike-perpendicular offsets of up to 10 km, our 3D fault model reveals the three major south-dipping surface splays of the SJT merge along a common detachment at ~3-4 km depth. This detachment steps down-to-the-south as a single thrust ramp below the northern Tian Shan ranges, extending to the base of the seismogenic crust. This study provides a well-constrained example of a crustal detachment acting as the physical link for offset surface fault splays that are known to have ruptured in a large, multi-segment earthquake. Moreover, we document the utility of mapping axial surfaces – which define regions of constant fold limb dip – to identify prominent fault bends at depth and delineate subsurface fault geometries and surface areas when subsurface data constraints are limited. These methods will enable improved 3D mapping and hazards assessments of segmented faults in other active fold-and-thrust belts.

Chapter 2 follows with a case study investigating the nature of active deformation over multiple rupture cycles on the SJT. This structure offers an ideal natural laboratory, as the fault and hanging wall fold geometries are constrained at depth by seismic reflection data and a series of fluvial terraces provide a ~250 kyr record of deformation. We integrate our subsurface interpretation of the SJT fault geometry defined in Chapter 1 with high-resolution records of surface folding and surface faulting strains, captured by terraces that have been preserved across the entire transect of the thrust sheet. The terrace geometries across the structure – mapped using a 1-m vertical resolution digital elevation model – indicate surface folding occurs abruptly across active synclinal axial surfaces. In addition, the structural relief developed by folding of Holocene terraces across bends on the SJT is fully consistent with the uplift recorded by these same terraces across the fault scarp. These observations support that folding in this thrust sheet is coseismic, and allow us to develop a method based on fault-bend fold theory to constrain fault slip and slip rates from terrace fold geometries. The fold dips of older Quaternary terraces progressively increase with terrace age, indicating fold growth in part by limb rotation. We replicate a fault-bend fold which grows by a combination of kink-band migration and limb rotation using a mechanical modeling approach, consistent with our subsurface interpretations and terrace analysis. Using our mechanical model, we develop a robust method for relating terrace limb dip to fault slip and – when combined with terrace geochronology – to slip rate. Our analysis indicates slip rate on the SJT has decelerated from the Late Quaternary (~7.0 mm/yr) to the Holocene (~1.3 mm/yr). These results highlight importance of considering spatiotemporal variations in slip and slip rate when assessing seismic hazards of active faults. Considering surface faulting *and* surface folding strains for multiple time markers will yield more accurate estimates of fault activity, paleo-event magnitudes, fault slip and slip rates and thus, improve regional seismic hazards assessments.

In addition to posing significant seismic hazards, structures in fold-and-thrust belts often form prolific petroleum traps, accumulating economic volumes of hydrocarbons in relatively small regions. Moreover, structural growth of such traps may deform viable conventional or unconventional reservoirs, significantly altering reservoir properties (e.g. porosity, permeability, fracture patterns, and compartmentalization). As exploration and production efforts target increasingly complex structures to supply energy demands, there is a pressing need to develop new, quantitative methods for defining trap geometries and reservoir properties, which may impact business decisions related to exploratory drilling and field development plans. In the final two chapters of this dissertation, we provide examples of advanced seismic interpretation and geomechanical restoration methodologies that deliver new insight into petroleum fields in China and West Texas. Notably, our results directly relate exploration and production trends to subsurface structure. These methods can be similarly applied for trap and reservoir characterizations in other fold-and-thrust belts.

In Chapter 3, we define the history of deformation across the present-day southern Junggar fold-and-thrust belt. Our interpretations of 2D and 3D seismic reflection data throughout the basin indicate the presence of early-middle Jurassic rift structures that were subsequently inverted in the late Mesozoic. Convergence continued throughout the Tertiary, developing a series of complex structural wedges that appear to be localized above the pre-existing inversion structures. These wedge structures continued to grow throughout the Cenozoic and serve as structural traps for the local petroleum system. Since the late Quaternary, deformation in southern Junggar appears to be localized dominantly – or perhaps exclusively – on the SJT, the active structure characterized in the first two chapters of this thesis. We present a new kinematic model for how the structural wedges in southern Junggar formed, and develop a new tectonic model for the timing of structural growth throughout the southern Junggar fold-and-thrust belt. Finally, we discuss the implications of this deformation timing and sequence of deformation on hydrocarbon charge, structural trap formation, and reservoir compartmentalization in the context of past and future petroleum exploration attempts.

In Chapter 4, we employ a new, 3D geomechanical restoration method to model strain patterns associated with fault displacement and fold growth across a naturally fractured gas reservoir in the Permian Basin, West Texas, USA. 3D restoration models are built from detailed structural interpretations of prominent thrust faults and overlying structural traps imaged by 3D seismic reflection data. Gradients in the displacement field of restoration models yield strain patterns and distributions predicted by our geomechanical approach. To assess the predicted strain patterns from our geomechanical structural restorations, we develop quantitative comparisons to independent measures of natural rock deformation. For this, we generate a semblance volume from the 3D seismic data – a coherence-based geophysical attribute measuring the similarity between adjacent stacked seismic traces – to illuminate secondary faults and prominent fractures zones that were not explicitly represented in our 3D restorations models. Our analyses indicate strong correlations between low semblance and elevated strains throughout the target reservoir in the studied field, indicating regions of discontinuous seismic reflectors are associated with regions of higher tectonic strain predicted by our restorations. These correlations suggest strains from geomechanical restorations have the ability to effectively define the distribution of secondary faults and fractures that are not explicitly represented in a restoration model. Thus, the geomechanical method employed here may provide predictive capabilities for defining reservoir properties. To assess this prospect, we integrate strain and semblance volumes with production data from the studied field to evaluate these correlations at the borehole scale for vertical and deviated wells. We describe how localized, tectonic strain likely produced secondary permeability, directly impacting the observed production trends from the studied reservoir, such as gas production, water cuts, and reservoir temperatures. This study demonstrates the ability to accurately predict strain distributions with 3D geomechanical restorations where structure has played a significant role in the development of reservoir permeability. Thus, we suggest these methods show promise as a fractured reservoir characterization tool for development operations where reservoir properties have been significantly impacted by structural growth.

CHAPTER 1

Seismic hazards of multi-segment thrust fault ruptures: insights from the 1906 M 7.4-8.2 Manas, China earthquake[1]

Introduction

Recent destructive earthquakes, such as the 2008 M_w 7.9 Wenchuan, China event, have demonstrated the complex nature of thrust fault ruptures, which commonly involve slip along multiple fault splays and breach lateral segment boundaries (e.g. Yeats et al., 1997; Hubbard and Shaw, 2009; Hubbard et al., 2010; Li et al., 2010b). These characteristics pose significant challenges when assessing the seismic hazards of active thrust faults. In many regions of active faulting, earthquake forecasts rely primarily on surface ruptures to define previous fault activity, slip rates, and paleoearthquake magnitudes. As a result, assessments of past and future event magnitudes are often based on the lengths of surface fault traces, with large offsets between thrust fault traces being used to define the limits of rupture patches (e.g. Magistrale & Day, 1999; Zhang et al., 1999; Wesnousky, 2006; 2008). However, many active thrust fault systems consist of multiple fault splays that merge or interact at depth (e.g. Shaw et al., 2002; Yue et al., 2005; Plesch et al., 2007; Hubbard et al., 2010). These fault networks pose significant seismic hazards as they have the potential to produce large, multi-segment earthquakes.

This study examines the subsurface geometry of a highly segmented thrust system in the southern Junggar basin, northwest China, which generated the 1906 M 7.4-8.2 Manas, China earthquake (Avouac et al., 1993; Burchfiel et al., 1999; Wang et al., 2004). This rupture has been interpreted to breach multiple surface fault trace offsets of 5-10 km (e.g. Avouac et al., 1993).

---

[1] A version of this chapter was published in *Seismological Research Letters* in 2014

Using high-quality two- and three-dimensional (3D) seismic reflection surveys, seismicity, and surface geology, we develop a 3D model of the faults that sourced this large magnitude rupture in order to investigate the relationship between the highly segmented surface ruptures and the fault system at depth. Our goal is to use this well-documented case study of the 1906 Manas earthquake to develop insights into the 3D geometries of active, segmented thrust faults that may facilitate the potential for large multi-segment ruptures in active thrust sheets worldwide.

Geologic and Seismotectonic Setting of the Southern Junggar Basin, China

The Tian Shan orogenic belt in northwest China (Figure 1.1A) began to accommodate crustal shortening at in late Oligocene to early Miocene (e.g. Hendrix et al., 1994; Yin et al., 1998; Sobel et al., 2006; Charreau et al., 2009), associated with convergence between the Indian and Eurasian plates (e.g. Molnar and Tapponnier, 1975) and possibly the Arabia-Asia collision as well (Yin et al., 2010). Regional seismicity, geodetic data, and field observations indicate the primary mode of tectonic motion in the Tian Shan is north-south contraction accommodated by thrust faulting (e.g. Nelson et al., 1987; Avouac et al., 1993; Abdrakhmatov et al., 1996; Thompson et al., 2002). Thrust faults throughout the Tian Shan region have generated several M ≥ 7 earthquakes over the past 200 years (Molnar and Ghose, 2000), highlighting that significant shortening in the region persists to the present. This active intracontinental mountain belt is flanked to the south by the Tarim basin, and to the north by the Junggar basin. The northernmost deformation front associated with the Tian Shan lies within southern Junggar, where a series of fold trends produce low hills that rise from the basin floor.

The most prominent structural trend of the southern Junggar basin consists of the Tugulu, Manas and Huoerguosi anticlines (Figure 1.1A). Multiple south-dipping thrust splays underlying

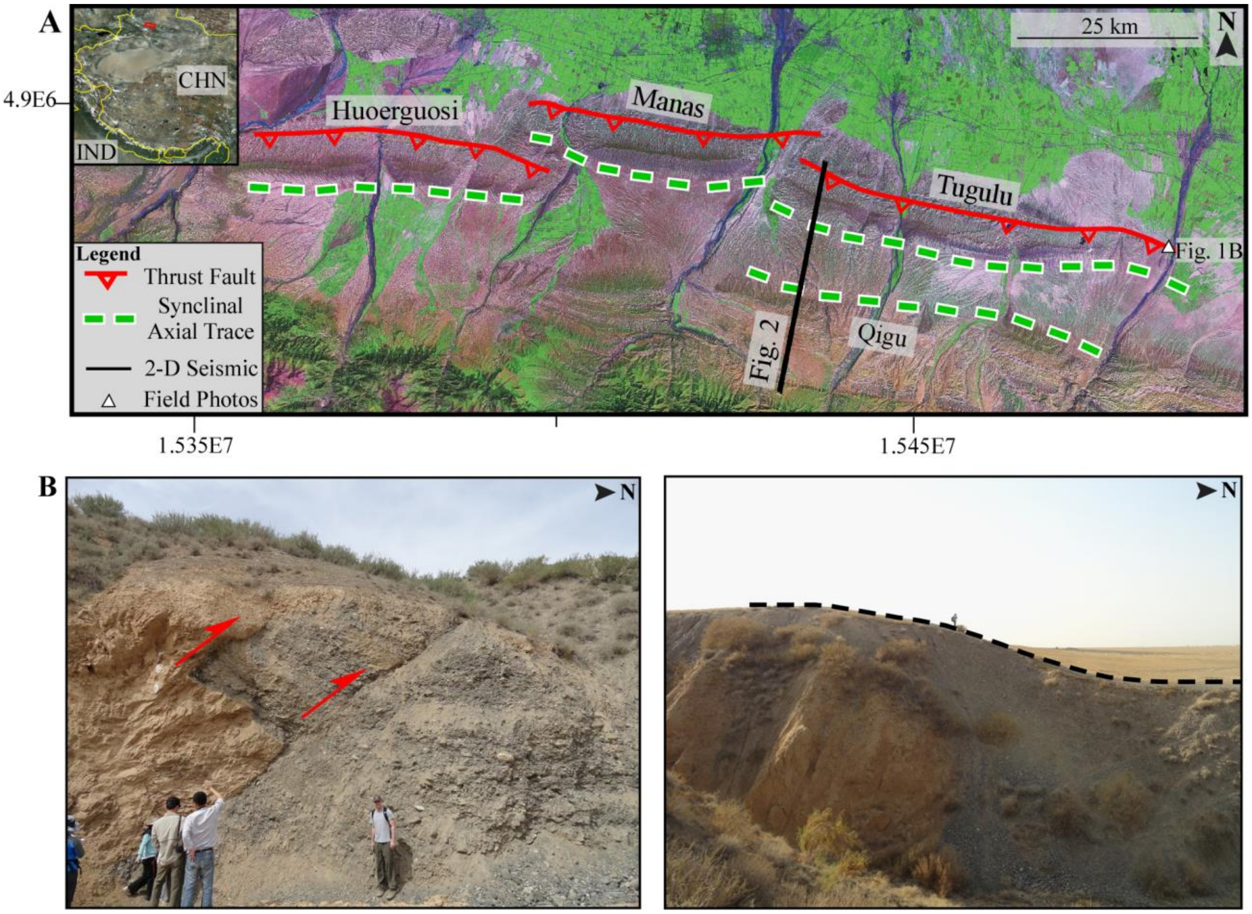

Figure 1.1: A) Location map of western China (inset) and Landsat imagery of the southern Junggar basin (red in inset). The two primary lateral fault segment boundaries are offset by ~5 km and ~10 km at the surface. Inset imagery from Google Earth. Landsat shown in bands 7-4-1 (R-G-B). CHN = China; IND = India. B) A road cut along the eastern flank of the Tugulu anticline reveals at least two fault splays of the Southern Junggar Thrust (SJT) reaching the surface (left), which directly underlie a prominent fault scarp (right). Scarp geometry outlined by black hashes.

each of these structures have outcrop exposure within fluvially incised valleys and along the flanks of the anticlines (Figure 1.1B). These thrusts have been identified in the field and with Landsat imagery (Avouac et al., 1993), providing constraints on the surface location of each splay. In addition, the subsurface of southern Junggar is well imaged with 2D and 3D industry seismic reflection data, which constrain the fault and fold geometries to ~10 km below sea level. Interpretations of these seismic reflection data reveal all three structures have evolved as imbricate stacks of fault-related folds (Li et al., 2010a). The shallowest thrust system that underlies this fold row, which we will refer to as the Southern Junggar Thrust (SJT), consists of three prominent fault splays, each of which consist of planar fault ramps that reach the surface (Avouac et al., 1993; Wang et al., 2004; Charreau et al., 2008; Li et al., 2010a). Holocene surface ruptures on SJT faults are well-preserved as fault scarps that offset several fluvial terraces in most of the river valleys across the study area, where each fault splay reaches the surface (Figure 1.1B) (Avouac et al., 1993). Fluvial terraces within multiple fold trends across southern Junggar also show broadly warped and folded profiles (e.g. Molnar et al., 1994; Poisson & Avouac, 2004), indicative of deformation within the hanging walls of these thrust sheets in the late Quaternary.

The most recent rupture along the SJT thrust sheet was the 1906 M_w 7.4-8.2 Manas earthquake, which has been interpreted to have ruptured most, if not all, of the SJT (Avouac et al., 1993; Deng et al., 1996; Burchfiel et al., 1999; Wang et al., 2004). In order to constrain the magnitude of the 1906 event, Avouac et al. (1993) surveyed the vertical offset of fluvial terraces across the fault scarp associated with the 1906 Manas earthquake. Measurements of this surface faulting, combined with estimates of the subsurface fault geometry, correspond to an M_w 7.4-8.2 for the 1906 rupture (Avouac et al., 1993). Other studies of the Manas earthquake using alternative methodologies inferred paleoearthquake magnitude estimates within this range (e.g. Burchfiel et al., 1999; Wang et al., 2004).

Three-Dimensional Fault Model of the Southern Junggar Thrust

The 1906 Manas earthquake rupture breached several large geometric segment boundaries, including strike-perpendicular offsets of ~5 and ~10 km at the boundaries of the Huoerguosi, Manas and Tugulu fault segments (Figure 1.1A). Using two 3D and several dozen 2D seismic reflection surveys across the southern Junggar basin, we have a unique opportunity to constrain the subsurface geometries of these active fault segments. By doing so, we hope to understand how these faults interact at depth and would allow them to rupture together, despite their significant surface trace segmentation.

Figure 1.2 shows an interpreted seismic reflection profile across the Tugulu anticline and Tian Shan range front that is characteristic of the SJT fault geometry along this structural trend. The upper SJT ramp dips down-to-the-south from its surface fault trace at ~45°, generally parallel to the dip of Tertiary strata that are in its hanging wall. At a depth of ~3.5 km below sea level, the SJT soles to a horizontal detachment that is localized near the base of the upper Eocene Anjihai Formation. This Eocene unit is composed of siltstones and mudstones, which we interpret to act as weak intervals that have localized the detachment. The transition from ramp to detachment is marked by the location of an axial surface that defines the southern limit of the Tugulu fold, consistent with fault-bend fold theory (Suppe, 1983; Medwedeff and Suppe, 1997; Suppe et al., 1997). This horizontal detachment extends roughly 10 km to the south of the Tugulu anticline, where we interpret the fault cuts down-section as a south-dipping thrust ramp. The location and dip of this ramp is constrained by the truncations of seismic reflectors that we interpret as hanging wall and footwall cutoffs, as well as the presence of folds in the hanging wall of the ramp that do not extend below the fault (Shaw et al., 2005). These folds in the hanging wall of the SJT involve Jurassic through Tertiary stratigraphy and form the northern Tian Shan range front. The geometries of these structures are constrained from surface outcrop, well penetrations, and seismic reflection profiles (Li et al., 2010a; Fan et al., 2012). In general, these folds involve north-dipping strata that are locally folded into south-vergent anticlines. The northern limit of the north-dipping Tertiary strata in this fold limb is defined by a synclinal axial surface that extends down to the Eocene detachment and is coincident with a structural wedge tip formed by the lower SJT fault ramp and a prominent north-dipping backthrust that steps up

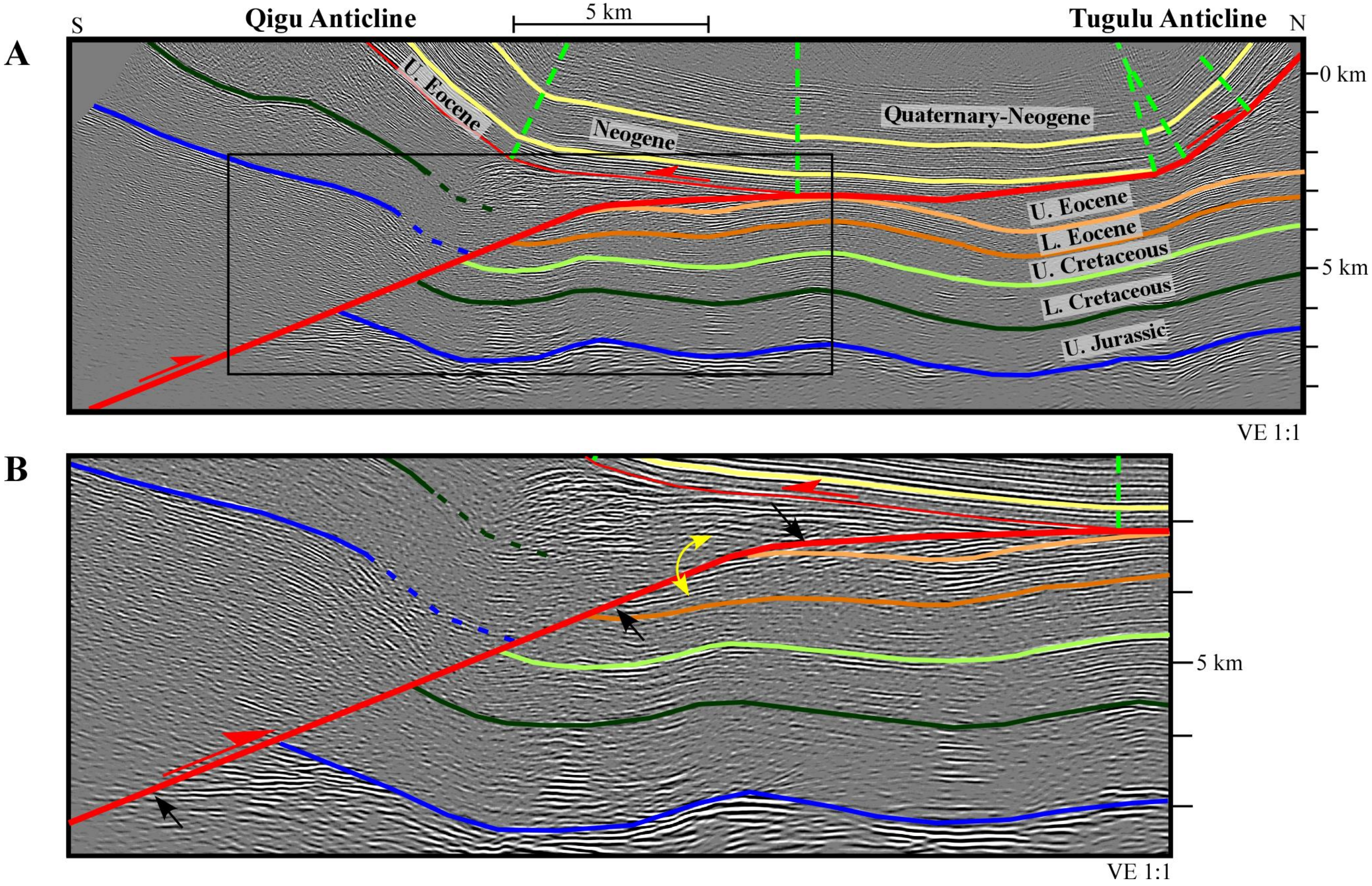

Figure 1.2: Seismic reflection profile across the Tugulu and Qigu anticlines. A) The Southern Junggar Thrust (SJT) dips ~45° south from the surface and soles to a detachment within the Upper Eocene interval. B) The SJT steps down-to-the-south from the Eocene detachment level, consistent with abrupt seismic reflector terminations (black arrows), changes in seismic reflector dip (yellow arrows) and the structural relief of the Mesozoic strata. See text for details. See Figure 1 for line location.

from the Eocene detachment (Figure 1.2A). The geometries of these folds, as well as the significant structural relief of the Mesozoic strata across the range front (Figure 1.2B), are consistent with our interpretation of a deep, south-dipping ramp in the SJT that is overlain by a series of north-dipping backthrusts forming structural wedges (Medwedeff, 1989; Shaw et al., 2005). These interpretations are generally consistent with previous models of the near-surface SJT fault geometry (e.g. Avouac et al., 1993; Burchfiel et al., 1999; Wang et al., 2004; Charreau et al., 2008). However, improved velocity modeling and detailed interpretations of more subsurface data suggest the lower ramp dip of the SJT is 22° ± 5°, shallower than previous interpretations of ~30°-45° (Avouac et al., 1993; Burchfiel et al., 1999; Wang et al., 2004).

In the footwall of the SJT ramp and Eocene detachment, the seismic reflection data reveal folding of Jurassic-Eocene strata. These structures are generally interpreted as detachment or fault-bend folds that formed above detachment levels localized within the Mesozoic section (e.g. Avouac et al., 1993; Li et al, 2010a). The seismic reflection data show that the SJT is not folded significantly by these deeper structures (e.g. Figure 1.2). This indicates a sequence of break-back thrusting across southern Junggar, where the SJT is younger than the underlying faults within the Mesozoic section (e.g. Avouac et al., 1993; Burchfiel et al., 1999; Charreau et al., 2008; Li et al., 2010a).

Using a dense grid of 2D and 3D seismic reflection data, we mapped the SJT and the associated fold trends across the study area. These seismic reflection data were migrated and subsequently depth converted using a velocity model derived from stacking velocities and sonic logs (Li et al., 2010a). Our interpretations of the SJT indicate the shallow SJT ramp beneath the Tugulu, Manas, and Huoerguosi folds each sole at depth to a common detachment level within the Eocene section (Figure 1.2; Appendix A). This shared detachment level provides direct structural linkage among the three fault ramps that have offset surface fault traces (Figure 1.3). Moreover, our seismic interpretations of the SJT and associated folds to the south along the range front suggest that the deep ramp of the SJT that we described south of the Tugulu fold extends along strike over the full extent of the Tugulu-Manas-Huoerguosi fold trend (Figure 1.2; Appendix A). The continuity of this deep fault ramp along strike is reflected by the continuity of the synclinal axial surface that marks the top of this lower fault ramp (Figure 1.4). Thus, our interpretations suggest that the deep portion of the SJT within the seismogenic crust effectively represents a single seismic source, despite the significant along-strike segmentation of the fault at and near the surface (e.g. Avouac et al., 1993).

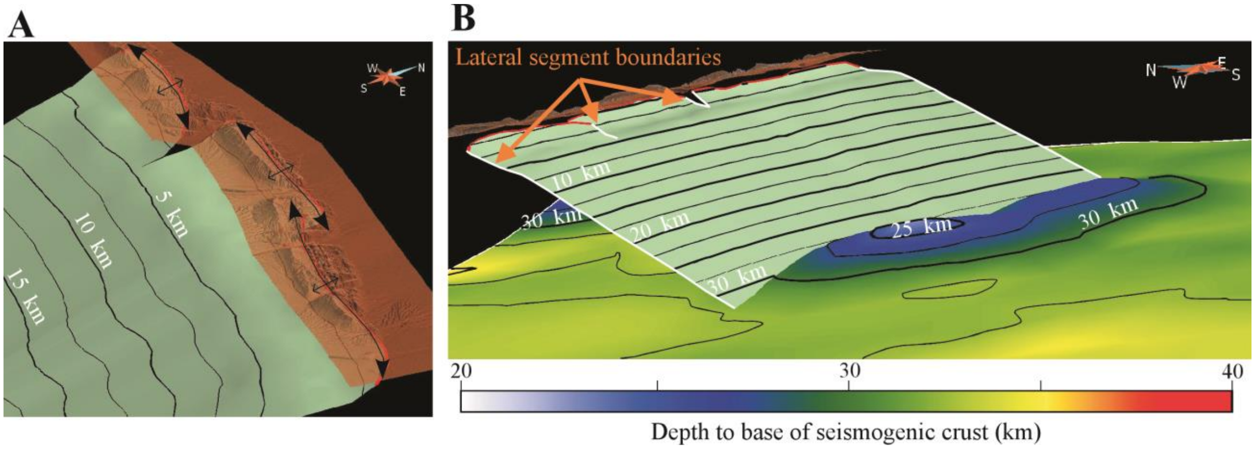

Figure 1.3: 3D fault model of the Southern Junggar Thrust (SJT). A) Three surface splays merge to a common detachment at ~3.5-4 km depth, south of the Tugulu-Manas-Huoerguosi fold row. The increase in along-fault distance between the 2.5 km and 5 km contours indicates the decrease in fault dip associated with the Eocene detachment. SJT surface shown in teal; fault tips highlighted in red; vertical exaggeration (VE) is 1:1. Semi-transparent 30-m digital elevation model VE is 5:1. Black contours are depth below sea level. B) Perspective view of the entire SJT fault model and base of seismicity in southern Junggar. Lateral segment boundaries (white) clearly illustrate the segmentation of the upper fault splay ramps directly beneath this structural trend. The base of SJT intersects the modeled base of the seismogenic crust at an anomalously shallow region (see text for discussion).

In order to complete our subsurface interpretation of the SJT, we modeled the base of the seismogenic crust following the workflow developed by Nazareth and Hauksson (2004) using regional seismicity data from the China Seismograph Network (CSN) spanning 1970-2011 (Appendix A). Lacking subsurface constraints below the imaging depth of the seismic reflection data, we assumed that the lower ramp of the SJT continued down to the base of the seismogenic crust at a constant dip of 22° ± 5° (Figure 1.3B). This model of the SJT yields a total fault area of 10,500 km^2 +1,500/-1,300 km^2. From a seismic hazards standpoint, empirical relations between thrust fault rupture area and moment magnitude estimate that this fault area corresponds to a potential earthquake magnitude (M_{MAX}) of 7.9-8.2 (Table 1.1; Wells and Coppersmith, 1994; Leonard, 2010). An event of this magnitude is consistent with the higher range of estimates for the size of the 1906 Manas earthquake (Avouac et al., 1993). However, this may be underestimating M_{MAX} for the SJT, as it has been shown that empirical relationships used to calculate earthquake magnitude may underestimate the size of $M_w \geq 7$ events (e.g. Hanks and Bakun, 2002). Additionally, the lateral extents of our fault model are limited by the available seismic reflection data constraints and may potentially extend farther along strike in either direction.

TABLE 1.1. Calculations of M_{MAX} Scenarios for the SJT

Base of Seismicity 1 (original)	**Lower Ramp Dip (°)**	**Fault Area (km^2)**	**Leonard, 2010**	**W&C, 1994**
	17	12000	8.3	8.0
	22	10500	8.2	7.9
	27	9200	8.2	7.9
Base of Seismicity 2 (raise 5 km)	**Lower Ramp Dip (°)**	**Fault Area (km^2)**	**Leonard, 2010**	**W&C, 1994**
	17	10500	8.2	7.9
	22	9500	8.2	7.9
	27	8200	8.1	7.9
Base of Seismicity 3 (lower 5 km)	**Lower Ramp Dip (°)**	**Fault Area (km^2)**	**Leonard, 2010**	**W&C, 1994**
	17	15100	8.4	8.1
	22	12000	8.3	8.0
	27	10000	8.2	7.9

The CSN seismicity catalog does not report uncertainties associated with each hypocenter location and depth, making it difficult to formally assess the uncertainty associated with our modeled base of seismicity surface. However, we calculate that raising or lowering the depth for the base of seismicity surface by 5 km yields fault areas for the SJT of 9,500 km^2 +1,000/-1,300 km^2 and 12,000 km^2 +3,100/-2,000 km^2, respectively, where the upper and lower bounds are defined by the ±5° uncertainty associated with the lower SJT fault ramp dip (Table 1.1). This, in turn, yields estimated M_{MAX} scenarios of 7.9-8.2 and 7.9-8.4, respectively (Wells & Coppersmith, 1994; Leonard, 2010). This larger range of event magnitudes (M_{MAX} = 7.9-8.4) continues to encompass the high end of the previously reported estimates (M 7.4-8.2) for the 1906 Manas earthquake (Avouac et al., 1993; Burchfiel et al., 1999; Wang et al., 2004). Thus, we conclude that our interpreted geometry of the SJT is a viable source for this 1906 event, and is generally consistent with the event estimates of Avouac et al., (1993).

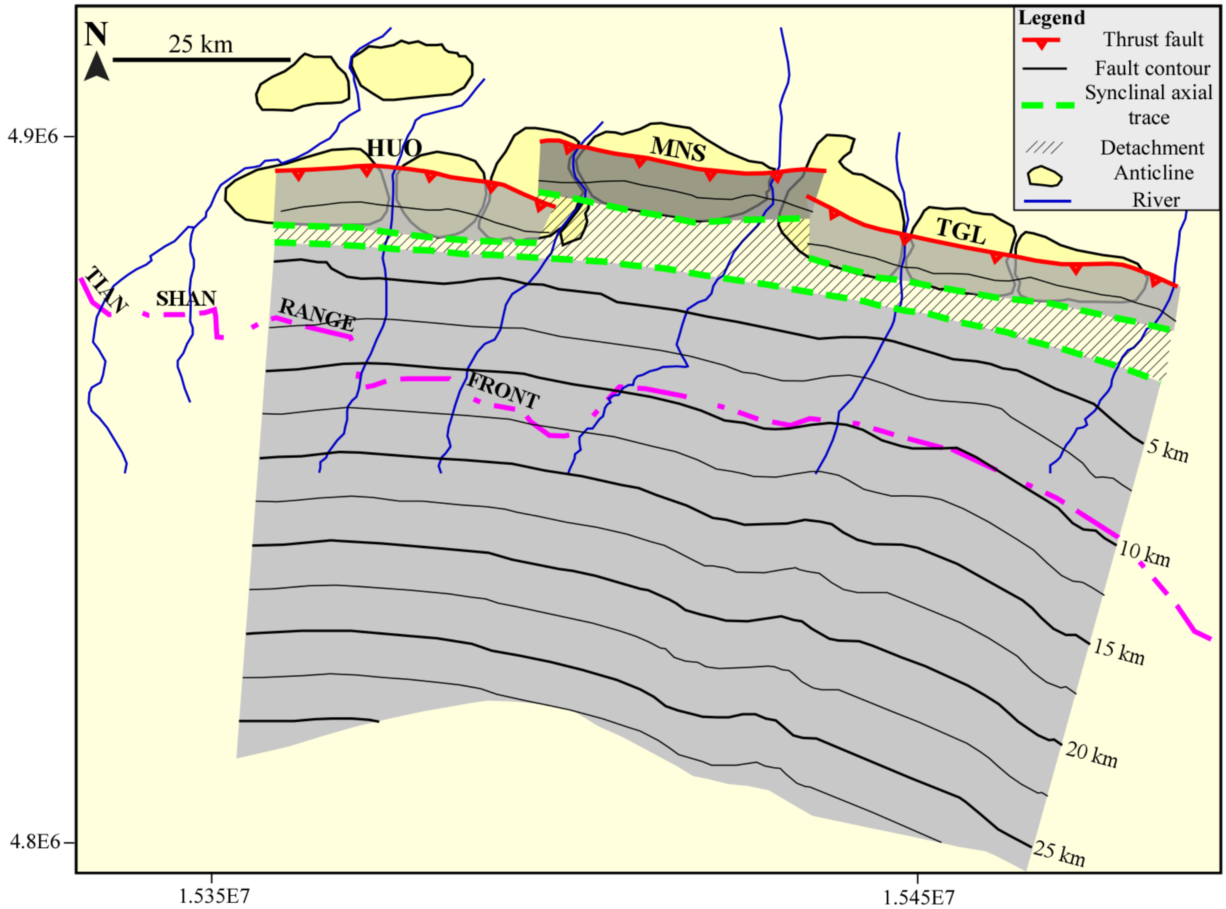

Figure 1.4: Fault contour map of the southern Junggar Thrust (SJT). The discontinuity of the 2.5 km contour is due to the segmentation of the SJT above the Eocene detachment. Note the continuity of the southernmost axial surface trace (see text for details). Fault ramps are shown in gray. Eocene detachment depicted as hashed lines. Tian Shan range front shown as dashed purple line. Fault contours are depth below sea level.

Examining the base of our fault model, we see that the SJT intersects a local high along the base of the seismogenic crust (Figure 1.3B). This could be interpreted to reflect stress relaxation effects following the 1906 Manas earthquake. In this interpretation, the immediate area at the base of the fault may lack sufficient seismicity to accurately model the true depth to the base of the seismogenic crust. This interpretation of recent tectonic quiescence at the base of the SJT would strengthen the argument that most, if not all, of this fault, including its down-dip extent, ruptured during the 1906 Manas earthquake (e.g. Avouac et al., 1993).

Seismic Hazards of Multi-Segment Thrust Faults

Three-dimensional models of active fault systems are critical for accurate seismic hazards assessment. These types of fault models allow for a comprehensive understanding of the potential size of past and future earthquakes by defining complete fault geometries and thus potential rupture areas (e.g., Shaw et al., 2002; Carena et al., 2004; Yue et al., 2005; Plesch et al., 2007; Hubbard et al., 2010). In addition, these models allow for a more robust understanding of fault connectivity by providing insight into the geometric relationships of faults at depth, which may differ significantly from those apparent at the surface (e.g. Figure 1.3, 1.4).

Previous studies of surface fault segmentation have observed relationships between map-view distance separating surface fault traces and the ability for a rupture to continue across the fault offset. Wesnousky (2006, 2008) observed that strike-slip fault jumps are limited to a maximum of 3-4 km, whereas dip-slip ruptures do not appear to continue across steps that exceed 5-7 km. Similarly, Zhang et al. (1999), observed a maximum discontinuity distance of ~5 km for normal fault rupture jumps in the Basin and Range Province. Furthermore, numerical models have shown there may be an upper limit to strike-slip fault jumps of approximately 5 km (e.g. Harris and Day, 1999). Similar numerical models of blind-thrust fault ruptures have shown maximum strike-perpendicular rupture steps of approximately 2 km when a tear fault is present, and an order of magnitude less in the absence of a tear fault (Magistrale & Day, 1999).

The strike-perpendicular step between the Tugulu and Manas surface fault traces in southern Junggar is ~5 km, and the discontinuity between the Manas and Huoerguosi surface fault traces is ~10 km (Figure 1.4). Our fault model demonstrates that, despite this surface segmentation, these fault splays merge at a common detachment in the Eocene stratigraphic section at ~3.5-4 km depth (Figure 1.3, 1.4), providing a physical mechanism for the entire SJT to rupture and generate large magnitude, multi-segment earthquakes. Consequently, the SJT is large enough to generate a $M_w \geq 8.0$ event, consistent with the higher end of the estimate range for the 1906 Manas earthquake (Avouac et al., 1993).

The ability of thrust fault ruptures to propagate across large strike-perpendicular fault trace offsets have also been observed in more recent events (e.g. Yue et al., 2005; Hubbard and Shaw, 2009; Hubbard et al., 2010; Li et al., 2010b). For example, the 2008 M_w 7.9 Wenchuan earthquake ruptured two fault segments that are offset by 9-10 km at the surface (Hubbard and Shaw, 2009; Hubbard et al., 2010). A 3D fault model of this thrust sheet, constrained by seismic reflection data, illustrates how these highly segmented surface fault traces are part of an imbricate thrust stack and merge at depth. This physical connection presumably allowed the two faults to rupture together and generate a large earthquake (Hubbard et al., 2010). Our analysis of the SJT uses a more precisely constrained fault model to establish a similar physical connection at depth between fault traces that are separated at the surface. In the case of the SJT, the connection is provided by a common detachment level. Such hard-linkage of thrust faults via mid-crustal detachments may allow coseismic ruptures to breach lateral segment boundaries of much greater distances than are often interpreted in the field (e.g. Zhang et al., 1999; Wesnousky, 2006; 2008) or predicted by numerical models (Magistrale & Day, 1999). This consequence highlights the importance of identifying crustal detachments, due to their ability to join fault segments at depth, when conducting seismic hazards assessments. In hindsight, the linkage of the fault segments at depth in this thrust sheet is clearly reflected in the locations and geometries of the axial surfaces that define the base and top of the upper and lower thrust ramps, respectively (Figure 1.4). Thus, the utilization of 3D fault models that incorporate fold geometries may improve our understanding of the geometric relationships of active faults at depth, even in cases where subsurface data are lacking (e.g. Shaw and Suppe, 1994; Shaw et al., 1994). We suggest that similar fault modeling approaches can improve assessments of the likelihood and potential size of multi-segment ruptures on active faults in seismically active regions around the world.

Conclusion

The southern Junggar basin provides a unique opportunity to relate a well-preserved, highly segmented surface rupture to the corresponding fault geometries at depth. Our fault model of this thrust sheet illustrates how subsurface data and fold geometries improve constraints on fault connectivity and total fault area, two important parameters used in seismic hazards assessments worldwide. For the southern Junggar case study presented here, our 3D fault model of the SJT provides a well-constrained example of a crustal detachment acting as a physical link by which faults with distinct surface offset may rupture together. Additionally, our SJT fault model provides estimates for an M_{MAX} scenario (M_w 7.9-8.4) that is compatible with the higher end of the estimate magnitude range for the 1906 Manas earthquake (e.g. Avouac et al., 1993). The ability to utilize axial surfaces to identify prominent fault bends in the absence of subsurface data constraints should provide confidence to improve existing and future seismic hazards assessments in region that may lack subsurface datasets.

CHAPTER 2

Active thrust sheet deformation over multiple rupture cycles: a quantitative basis for relating terrace folding to fault slip rates[2]

INTRODUCTION

The destructive nature of convergent tectonics is manifest by large magnitude earthquakes that occur both along subduction zones and within fold-and-thrust belts. Contemporary events of this latter type (e.g., 1999 Mw 7.6 Chi-Chi, Taiwan; 2008 Mw 7.9 Wenchuan, China; 2015 M_w 7.8 Gorkha, Nepal) have led to tens of thousands of deaths and billions of dollars of damage to infrastructure. These earthquakes have also demonstrated some of the ongoing challenges associated with assessing the hazards posed by active thrust faults. Specifically, surface deformation associated with thrust fault earthquakes is multifaceted, often involving components of coseismic folding as well as surface faulting (e.g., Chen et al., 2007). Many active thrust faults - or portions of these faults – are blind, such that surface deformation is characterized exclusively by folding (e.g., Stein and King, 1984; Shaw and Suppe, 1994; Dolan et al., 2003). However, traditional, geologic methods of inferring fault activity, slip rate, and paleoearthquake magnitudes are based exclusively on characterizations of surface faulting deformation (e.g. Wells and Coppersmith, 1994; Wesnousky, 2006; 2008; Leonard, 2010). These methods prove inadequate, in cases where all or a portion of subsurface fault slip is manifest by folding at the surface. Thus, recent studies have made progress in adapting traditional paleoseismic methods to recover more accurate records of fault activity on blind thrust faults (e.g., Mueller et al., 1999; Pratt et al., 2002; Shaw et al., 2002; Dolan et al., 2003; Leon et al.,

---

[2] A version of this chapter was submitted for publication in *GSA Bulletin* in 2016

2007; 2009). These methods generally require kinematic fault-related folding models in order to quantitatively relate surface folding strains to fault activity.

Despite the challenges of constraining deformation in active thrust sheets, coupled faulting and folding deformation accumulated over geologic timescales has been recognized for decades (e.g., Rich, 1934; Dahlstrom, 1970) and their direct relationships are now well-established by fault-related folding theories (e.g. Suppe, 1993; Suppe and Medwedeff, 1990; Hardy and Poblet, 1995; Suppe et al., 2004; Shaw et al., 2005). The fundamental basis for these theories underscores the oft-observed occurrence of folds with faults: folding is driven by slip across fault-bends, at propagating fault tips, and along detachments – reflecting displacement gradients within a thrust sheet (Figure 2.1). This fault-related folding concept is central to our understanding of how shortening is accommodated in Earth's brittle crust over geologic time scales. Moreover, it has critical implications for seismic hazards assessment as it describes a range of ways that folding may reflect fault slip at depth. For example, a classic fault-bend fold (Suppe, 1983) predicts that fault slip remains constant as it is transmitted up a planar thrust ramp (Figure 2.1A). Thus, a measure of surface slip (SS) along an emergent thrust ramp of a fault-bend fold will yield an accurate estimate for the amount of fault slip at depth (SD). However, other classes of fault-related folds form due to fault slip gradients along a thrust ramp. In the case of a simple shear fault-bend fold (Suppe et al., 2004; Hardy and Connors, 2006), slip increases linearly up a planar ramp through the shear interval. In this scenario, measures of surface slip would likely overestimate the displacement on a deeper portion of the thrust ramp (Figure 2.1B). In contrast, fault-propagation folds (e.g. Suppe and Medwedeff, 1990) consume slip during thrust tip propagation, producing a linearly decreasing slip gradient up a thrust ramp (Figure 2.1C). If the thrust is surface-emergent, measures of surface slip would likely underestimate estimates of slip, and thus paleoearthquake magnitude or long-term slip rates. Finally, despite the wide utility of fault-related folding theories to characterize natural structures (e.g. Shaw et al., 2005), several analog and mechanical modeling studies have provided insights into natural folding deformation that cannot be described using current kinematic formulations. For example, mechanical models of fault-bend folds have been shown to accommodate shortening involving components of structural growth limb rotation, whereas the kinematic theory predicts folding exclusively by kink-band migration. These examples highlight the importance of properly defining faulting and folding relations when employing surface deformation patterns to infer fault activity at depth along thrust sheets.

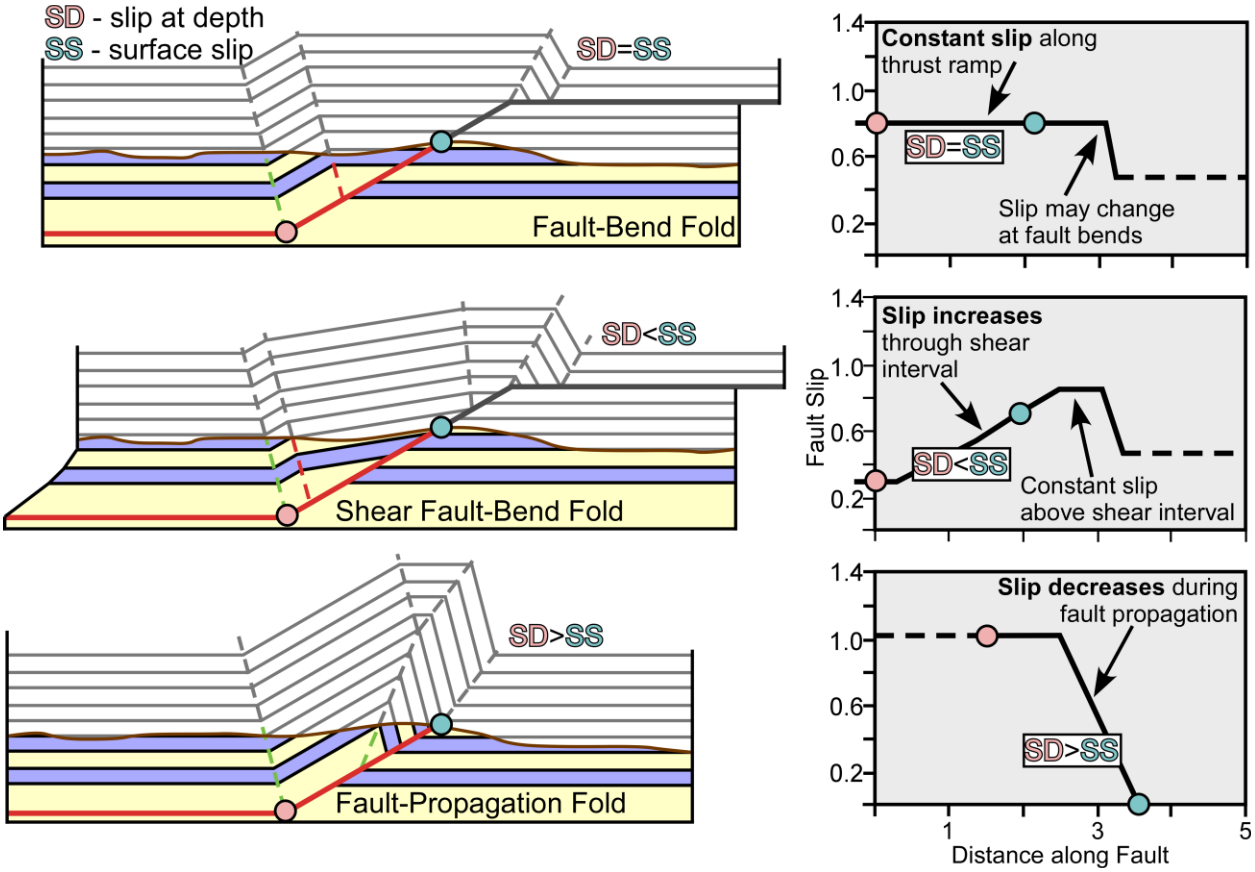

Figure 2.1: Fault-related fold models and their corresponding distance-displacement plots, including measures of surface slip (SS) and fault slip at depth (SD). A) Fault-bend folds (Suppe, 1983) predict constant fault slip up a thrust ramp. B) Simple shear fault-bend folds (Suppe et al., 2004) produce a wide, gentle fold limb above the pre-growth shear interval, where slip increases linearly up the thrust ramp. C) Fault propagation folds consume fault slip during fault tip propagation. The resultant slip gradient decreases linearly up a thrust ramp. See text for details. Figure modified from Hughes and Shaw (2014).

In this article, we describe new methods to quantitatively relate surface faulting and surface folding strains across active thrust sheets over multiple rupture cycles. Our techniques are based on established fault-related folding concepts and new geomechanical models, which we employ to study earthquake deformation and active fold kinematics across the seismically active Southern Junggar Thrust (SJT) in the southern Junggar fold-and-thrust belt, northwest China. When combined with geochronological constraints, these methods have the ability to elucidate detailed records of fault-related folding from individual ruptures to one hundred thousand year timescales. Using high-resolution digital elevation models, subsurface seismic reflection data, and feldspar luminescence geochronological dating methods, we extract detailed records of fluvial terraces deformation and directly relate these to subsurface structure. We quantify SJT fault slip implied by Holocene fold scarps and compare these estimates to independent measures implied by Holocene fault scarp uplift records. We describe how these complete records of surface deformation can be effective tools for evaluating – and informing – interpretations of subsurface structure and folding kinematics. Finally, we define new faulting and folding relations implied by mechanical fault-related fold models to quantify fault slip from measures of terrace uplift and folding patterns. Using these techniques, we define a detailed record of fault slip and slip rate across the SJT extending from the most recent rupture in 1906 through the Late Quaternary. We confidently establish a record of fault slip deceleration on the SJT over this timeframe, yielding perhaps the most detailed record of fault slip history of any thrust sheet over a 100 kyr+ timescale.

STYLES OF ACTIVE THRUST SHEET DEFORMATION

Sediments deposited across actively growing structures (i.e. growth stratigraphy) record natural folding kinematics (e.g. Suppe et al., 1992; 1997), cumulative fault slip histories (e.g.

Shaw and Suppe; 1994; 1996) and discrete coseismic events (e.g., Dolan et al., 2003; Leon et al., 2009). In a similar vein, terraces that extend across an active fold or fault can be passively deformed and record earthquake deformation from one or several ruptures. This has led to significant advancements in tectonic geomorphology utilizing deformed marine or fluvial terrace geometries to constrain active deformation (e.g. Mueller et al., 1999; Lavé and Avouac, 2000; Thompson et al., 2002; Gold et al., 2006; Scharer et al., 2006; Amos et al., 2007; Hubert-Ferrari et al., 2007; Ishiyama et al., 2007; Yue et al., 2011; Le Béon et al., 2014). These methods utilize terrace fold geometries as records of fold kinematics that can be described by fault-related folding theories, or variants of these existing methods (Figure 2.2). These models make different predictions for folding of growth strata or terraces that are governed by the kinematics of the underlying structure. For example, fault-bend folds (Suppe, 1983; Suppe et al., 1992; 1997) and certain classes of fault-propagation folds (Suppe and Medwedeff, 1990) grow by kink-band migration, a folding process where folds develop a constant dip and continue to widen with increasing fault slip. These kinematic models predict terrace folds to be localized across fault bends (Figure 2.2A-B) and above blind thrust tips. In contrast, structures that grow by limb rotation exhibit fold limbs that progressively increase fold dip with increasing fault slip. Limb rotation is a common folding mechanism in the presence of hanging wall shear (Suppe et al., 2004; Hardy and Connors, 2006; Yue et al., 2011) and is predicted across some listric fault geometries (e.g., Seeber and Sorlien, 2000; Amos et al., 2007; Hu et al. 2015). As a result, fault-related folds growing primarily by limb rotation produce distributed terrace fold signatures (Figure 2.2C-E).

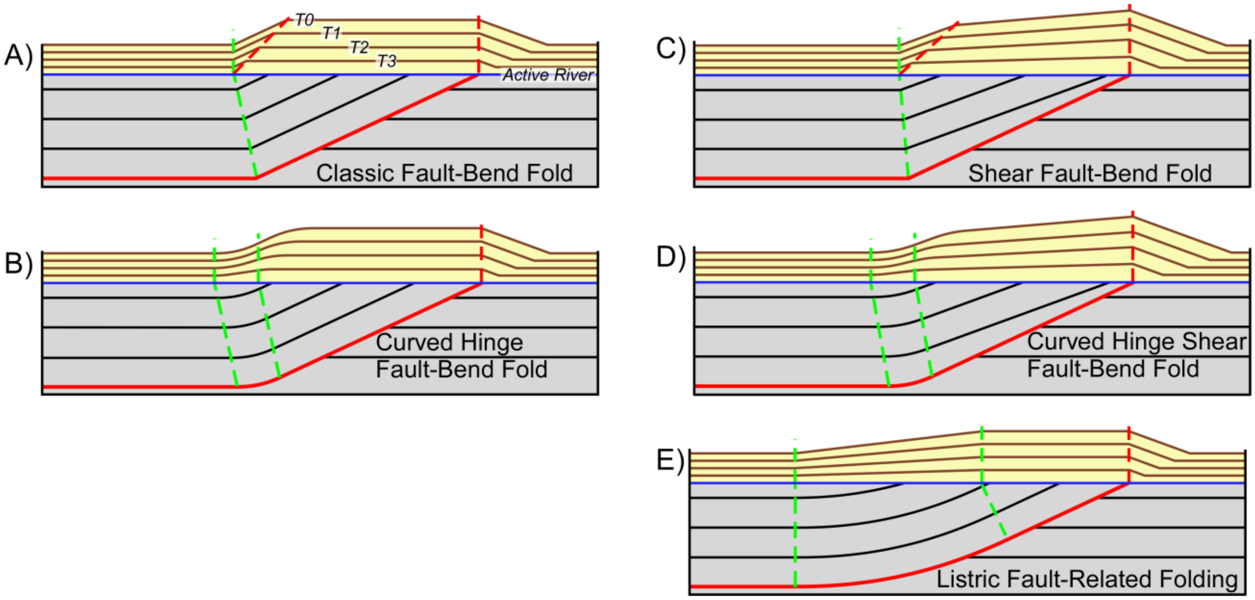

Figure 2.2: Kinematic models of terrace deformation. A) Classic fault-bend folding (Suppe, 1983) localizes folding across fault bends. Terrace folds develop by kink-band migration. B) Curved hinge fault-bend folds (Suppe et al., 1997) produce fold scarps due to differential uplift localized through a curved fault bend. Terrace folds grow by kink-band migration. C) Simple shear fault bend folds (Suppe et al., 2004) are characterized by intense folding across the fault bend, which grows by kink-band migration. Outboard of this zone and across the pre-growth shear interval, more distributed folding occurs by limb rotation. D) Simple shear curved hinge fault-bend folds (Suppe et al., 2004) produce folds of similar styles as described in C but differ only due to kink-band migration across a curved fault zone of finite width, as described in B. E) Listric fault-related folds (Seeber and Sorlien, 2000) exhibit distributed folding by limb rotation across a listric fault ramp. In E, the region undergoing limb rotation is localized to the listric fault segment. See text for details.

An accurate classification of the deformation style present in a thrust sheet is necessary to confidently relate surface deformation to subsurface fold kinematics and fault slip at depth. In many active thrust sheets, this is not a straightforward assessment: subsurface structure – and the implied folding kinematics – must often be inferred from a combination of surface geology, subsurface geophysical data, and terrace deformation constraints. Structures that grow exclusively by kink-band migration or limb rotation yield distinct patterns of fold dips and limb widths recorded by growth strata or terraces (Figure 2.2). However, several records of growth strata and terrace geometries across natural structures exhibit components of both kink-band migration and limb rotation (e.g. Dolan et al., 2003; Benesh et al., 2007; Yue et al., 2011), making it difficult to discriminate between competing kinematic fold models. In addition, the ability to resolve modest differences between competing kinematic models (e.g. curved shear fault-bend fold versus listric fault-bend fold; Figure 2.2 D-E) with natural terraces – subject to incomplete preservation, subsequent dissection and potentially anthropogenic modifications – can prove challenging. Moreover, without independent data on fault slip and slip rate, it generally remains unclear how accurately even the most suitable of these kinematic models can be used to relate surface folding to fault slip at depth. In the following section, we describe the geologic setting of our study area – the southern Junggar basin, NW China –, which provides a unique opportunity to quantify fault slip from independent measures both folding and faulting strains over multiple earthquake cycles. We take advantage of this ideal natural laboratory for developing and applying general methods of quantifying folding across an active thrust sheet and relating it to fault slip and slip rate at depth on active thrust sheets.

SOUTHERN JUNGGAR BASIN

Structural Setting

The southern Junggar basin is the northeastern foreland fold-and-thrust belt of the Tian Shan ranges (Figure 2.3A). Southern Junggar is characterized by three rows of fault-related folds, which are underlain by surface-emergent and blind thrust faults (Figure 2.3B). Many of these structures originated as Jurassic-aged rift structures that were subsequently inverted in the Late Jurassic or Early Cretaceous (Guan et al., 2016). These inversion structures localized the development of complex fault related folds involving coeval activity on linked forethrusts and backthrusts, a class of fault-related fold termed a structural wedge (Medwedeff, 1989). Much of the Cenozoic deformation history has been localized on deep-seated detachments within the Jurassic and Cretaceous stratigraphic intervals that ramp up from their detachment levels into the cores of the wedge structures. However, most recently, the active Southern Junggar Thrust (SJT) broke through to the surface in a break-back sense of thrusting sometime in the Quaternary

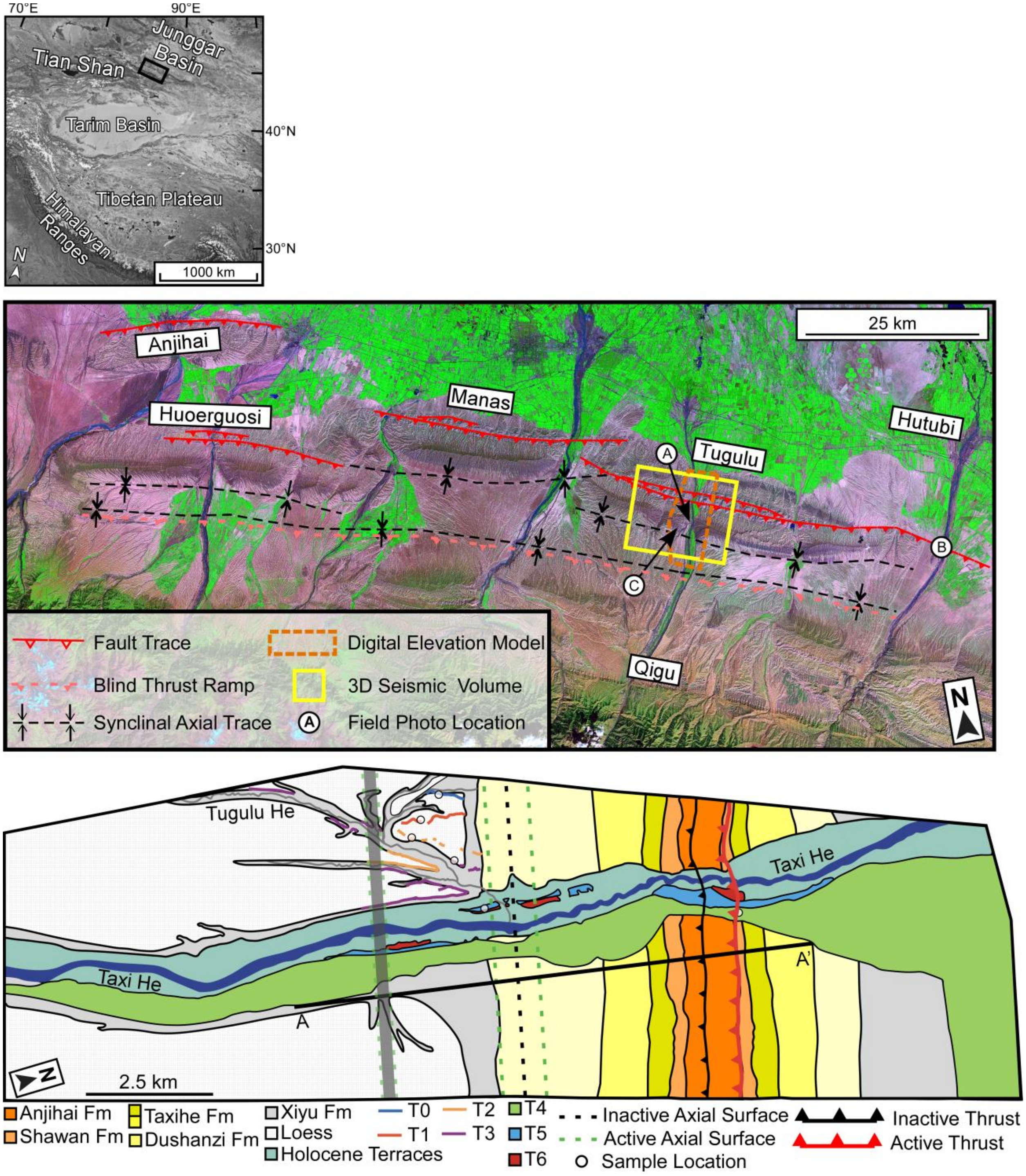

Figure 2.3: A) Western China and major tectonic provinces. Black box outlines the southern Junggar basin. Imagery from Google Earth. B) False-color Landsat imagery of the southern Junggar basin study area. Imagery is displayed with bands 7-5-1 (R-G-B). C) Geologic map of surface geology and mapped terraces along the Taxi He valley, across the Tugulu anticline, mapped in the digital elevation model. Section A-A' is shown in Figure 2.5.

(Guan et al., 2016). Continued activity on the SJT has amplified the emergence of a prominent fold trend in the southern Junggar basin, composed of the Tugulu, Manas and Huoerguosi anticlines (Figure 2.3B), which expose Quaternary and Neogene strata along the flanks of each structure and expose Eocene rocks in the anticlinal cores (e.g. Figure 2.3C). These anticlines also form structural traps for petroleum fields (Guan et al., 2016), which motivated the collection of 2-D and 3-D seismic reflection data used in this study.

Seismotectonic Setting

Present-day geodetic observations suggest ~11 mm/yr of shortening is accommodated across the central Tian Shan, decreasing to ~5 mm/yr ~86° E in the southern Junggar basin and to ~0 mm/yr at ~90° E longitude (Meade, 2007). Geodetic shortening is consistent with focal mechanism solutions throughout the Tian Shan ranges (Nelson et al., 1987) and the persistence of $M_w \geq 7$ earthquakes across the Tian Shan over the past two centuries (Molnar and Ghose, 2000). Indeed, measureable Quaternary-Holocene fault slip along discrete thrust faults throughout the ranges associated with earthquake deformation accounts for much, if not all, of the total shortening across the Tian Shan (e.g. Avouac et al., 1993; Burbank et al., 1999; Thompson et al., 2002; Hubert-Ferrari et al., 2007).

Continued fault activity throughout the Holocene on the SJT is recorded by progressive uplift of fluvial terraces across prominent fault scarps where the SJT is surface-emergent (Avouac et al., 1993; Deng et al., 1996). The SJT is a highly-segmented thrust sheet, exhibiting strike-perpendicular offsets of up to 10 km along the forelimbs of the Tugulu-Manas-Huoerguosi fold row (Figure 2.3B). Despite this segmentation at the surface, it has been interpreted that all three surface splays of the SJT ruptured coseismically during the most recent rupture, the 1906 M_w 74.-8.2 Manas, China earthquake (Avouac et al., 1993; Deng et al., 1996). A 3-D fault model of the SJT – constrained by 2- and 3-D seismic reflection data – reveals that, despite these significant lateral segment boundaries at the surface, the three major south-dipping surface splays of the SJT merge at depth along an Eocene detachment horizon as a continuous thrust sheet (Stockmeyer et al., 2014). The SJT extends farther to the south before ramping down below the northern Tian Shan rangefront, likely extending to the base of the seismogenic crust (Stockmeyer et al., 2014). This 3-D characterization of the SJT suggests it is capable of sourcing $M_w>8$ earthquakes, consistent with the magnitude estimates of the 1906 rupture.

Fluvial Terrace Records

The Tugulu-Manas-Huoerguosi folds are dissected by an internally drained fluvial system, fed by glacial melt in the northern Tian Shan. Cycles of lateral and vertical incision within several fluvial networks have produced suites of fluvial terraces throughout the basin (e.g. Figure 2.4A), many of which are preserved across entire fold transects (e.g. Molnar et al., 1994; Poisson and Avouac, 2004). These fluvial terraces serve as passive strain markers, recording faulting deformation where the SJT is surface-emergent as well as surface folding strains. Holocene fault activity along the SJT recorded by progressive uplift of several terrace treads was well-documented in the seminal study of Avouac et al. (1993). These records of surface faulting – recording >15 m of relief in places – were unambiguous during field reconnaissance (Figure 2.4B). In addition, warping of terrace treads due to distributed surface folding has been documented across the anticlinal cores of the Dushanzi and Tugulu anticlines (Molnar et al. 1994; Poisson and Avouac, 2004). These surface strains reflect subtle components of surface folding that can be readily documented. Finally, our field reconnaissance documented abrupt, localized terrace folds in the backlimb of the Tugulu fold (Figure 2.4C). These terraces exhibit up to hundreds of meters of structural relief, likely reflecting a significant magnitude of fault slip at depth. Thus, we have a unique opportunity to quantify deformation across the entire hanging wall of the surface-emergent SJT, from its Eocene detachment south of the Tugulu backlimb,

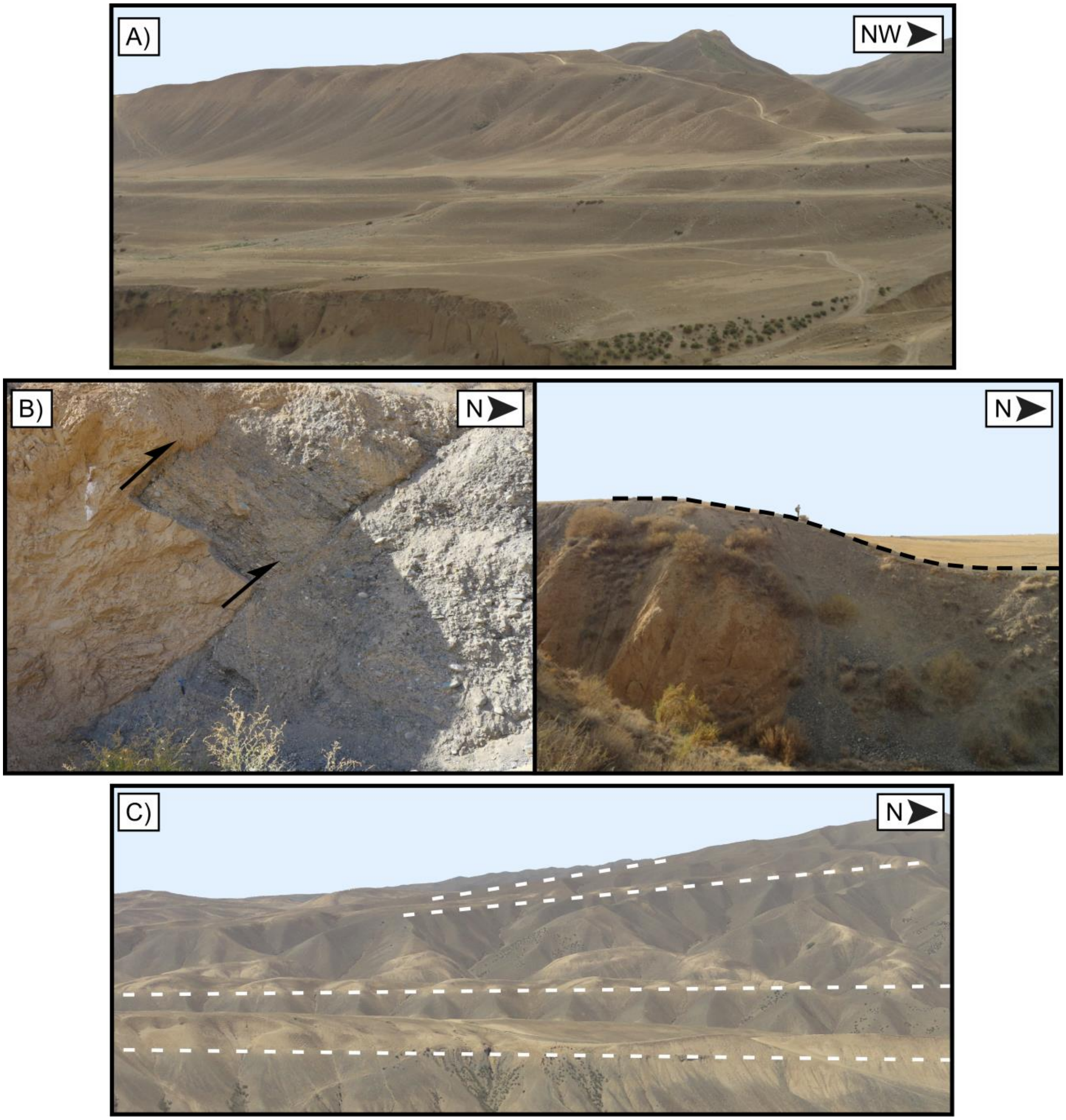

Figure 2.4: A) Several flights of fluvial terraces are preserved across the entire extent of the Taxi He. B) A prominent fault scarp marks the surface-emergent SJT (Avouac et al., 1993). This provides a record of surface faulting deformation. C) Older, discontinuous terraces in the backlimb of Tugulu record surface folding deformation. Terrace treads marked by loess-conglomerate (tan-grey) contact.

across the core of the structure and continuing to the prominent fault scarp where the SJT is surface-emergent (Figure 2.3C). Quartz luminescence geochronological methods have proven well-suited for obtaining absolute age constraints for terraces across the southern Junggar basin, yielding reliable dates of terrace abandonment through the Holocene (e.g. Poisson, 2002; Poisson and Avouac, 2004; Gong et al., 2014). In this study, we apply recently developed methods of feldspar luminescence geochronology (e.g. Brown et al., 2015; Rhodes, 2015) that extends the range of reliable ages for terrace abandonment to the Late Quaternary.

An Ideal Natural Laboratory

The southern Junggar basin presents a unique opportunity to apply quantitative methods of extracting thrust sheet deformation and natural fold kinematics from records of active terrace faulting and folding. Specific aspects of the study area that produce such a unique location include: 1) an active thrust sheet that ruptures in large earthquakes, likely $M_w \geq 8$; 2) the availability of high-quality 2- and 3-D seismic reflection data imaging subsurface fault geometries and folding kinematics; 3) several records of both surface faulting and surface folding strains, captured by deformed fluvial terrace records across the entire hanging wall of the active thrust sheet; and 4) the ability to obtain reliable, absolute age constraints of surface strain markers to constrain fault slip rates over >100 kyr timescales.

SUBSURFACE DEFORMATION

The Southern Junggar Thrust (SJT) is thought to be the most active structure in southern Junggar; it most recently ruptured during the 1906 M_w 7.4-8.2 Manas, China earthquake (Avouac et al., 1993; Burchfield et al., 1999). Due to active petroleum exploration and development in the region, the SJT and hanging wall fold geometries are well-constrained by high-quality 2- and 3-D seismic reflection surveys (Stockmeyer et al., 2014; Guan et al., 2016). The SJT is particularly well-imaged in the upper 3-4 km of the crust due to the presence of direct footwall cutoffs, terminating hanging wall axial surfaces, and direct fault plane reflections (Stockmeyer et al., 2014). These data provide tight constraints on the geometry and location of each segment of the SJT. Our interpretation of the SJT in section A-A' (Figure 2.5) depicts the thrust sheet stepping up from its mid-crustal Eocene detachment (Stockmeyer et al., 2014). This Eocene detachment has a modest dip of 3.4° ± 1.5° south (θ_0). The SJT rises from this detachment across multiple synclinal fault bends, achieving a dip of 27.4° ± 1.5° south (θ_2). To generate this steeper ramp dip, we interpret three principal fault bends that are associated with synclinal axial surfaces in the hanging wall strata. The axial surfaces for the latter two bends interfere in the near-subsurface producing a single axial surface trace representing the transition from the fault segments labeled θ_1 to θ_2 in Figure 2.5 (e.g. Medwedeff and Suppe, 1997). The relationship of this fault geometry to the hanging wall folds is consistent with classic fault-bend folding theories (Suppe, 1983; Medwedeff & Suppe, 1997). Another viable interpretation for this 24° increase in fault dip could invoke a curved fault geometry (Suppe et al., 1997). The well-defined planar geometries for the detachment (θ_0=3.4°) and the thrust ramp beyond the bend (θ_2=27.4°) observed in the 2D and 3D seismic data limit the horizontal extent of this zone of curvature to a maximum dip-parallel distance of ~2000 m. In such a case, the axial surfaces accommodating folding in the hanging wall would have a comparable finite width (Suppe et al., 1997). In either case, terrace deformation caused by displacement across these fault bends is expected to occur along – or at least in the vicinity of – surface projections of active synclinal axial surfaces (Figure 2.2A-B; Shaw et al., 1994). A third interpretation we explored invoked a listric fault-bend fold interpretation (e.g. Figure 2.2E; Seeber and Sorlien, 2000; Amos et al., 2007). We document why such an interpretation is not viable for the SJT in Appendix B.

Farther to the north in section A-A’, we interpret the SJT further increases its dip across a series of fault bends associated with synclinal axial surfaces in the hanging wall stratigraphy (Figure 2.5). We observe direct fault plane reflections indicating that the SJT branches into two fault splays across this series of fault bends. The northern surface splay of the SJT has a strictly planar geometry and is surface-emergent where Avouac et al. (1993) documented a prominent fault scarp in the Taxi He valley (Figure 2.5). This finding has two primary implications. First, the planar geometry of the SJT across the structural crest of an underlying imbricated structural wedge (Figure 2.5) implies the SJT is the only active structure at present (Lu et al., 2010; Guan et al., 2016), and thus, all terrace deformation is due to fault-bend folding along the SJT. If the deeper structures were active, the shallow segments of the SJT would be folded where they cross the footwall fold crest. This is the primary evidence to suggest the SJT reflects a period of break-back thrusting regionally across the southern Junggar thrust belt (Guan et al., 2016). Second, as there is only a fault scarp across the northern surface trace of the SJT, the near-surface splays of the thrust sheet appear to have developed in a locally break-forward sequence of thrusting. The lack of any differential uplift across the southern surface splay of the SJT implies it has been inactive since at least the start of the Holocene. In addition, this suggests the black axial surface in Figure 2.5 is inactive; we should not expect any terrace deformation across the surface projection of this synclinal axis. Thus, our detailed constraints on the SJT seems to reflect a rather complex evolution of thrusting sequences. Regionally, the SJT reflects break-back thrusting as it truncates older, inactive structures in its footwall. Locally, however, near-surface splays imply a break-forward thrusting sequence. This complex thrusting sequence adds to the structural complexity of the southern Junggar fold-and-thrust belt (Guan et al., 2016). However, our subsurface interpretations yield a rather straightforward expectation for our records of surface deformation: any terrace folding can be attributed to fault slip on the SJT across active (i.e. green) axial surfaces and terrace faulting should be exclusive to the northern surface splay (Figure 2.5). Thus, records of surface deformation can be used as a rather effective tool to evaluate our subsurface interpretations of fault-bend folding, regional break-back thrusting (Guan et al., 2016) and local break-forward thrusting at Tugulu (Figure 2.5).

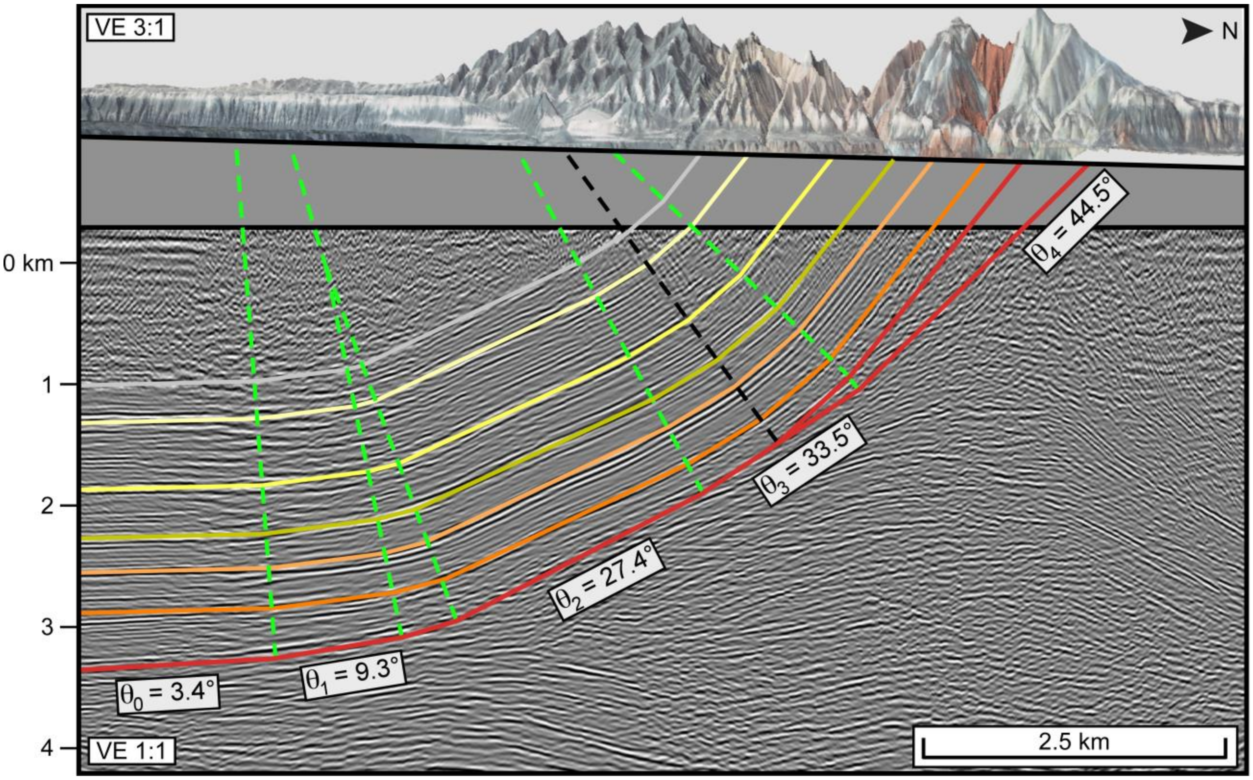

Figure 2.5: Structural interpretation of the SJT fault geometry and hanging wall fold structure across section A-A'. The geometry of the interpreted fault and hanging wall folds are consistent with a fault-bend fold (Suppe, 1983). Projecting axial surfaces to the Earth's surface provide a straightforward method for relating surface deformation observations to subsurface structure (e.g. Shaw and Suppe, 1994b). See text for details. Satellite imagery and digital elevation model are displayed at 3:1 vertical exaggeration.

Altogether, we interpret the SJT as a series of south-dipping fault ramps that increase in dip from 3.4° ± 1.5° (θ_0) along its Eocene detachment to 44.5° ± 1.5° (θ_4) at the surface (Figure 2.5). The planar geometry of the SJT splays across the crests of the footwall anticlines indicates the deeper structures are inactive. The fault bends along the the active segments of the SJT yield active synclinal axial surfaces, which, when projected to the surface, provide locations where surface folding is expected to occur (e.g. Shaw et al., 1994), if our interpretations of fault-bend folding and thrusting sequences are accurate. Similarly, terrace uplift from surface faulting is predicted to be limited to the northern SJT surface trace, which would be consistent with our thrust sequence interpretation and the work of Avouac et al. (1993). In the following section, we assess our subsurface interpretation by comparing terrace deformation to the predictions implied by our subsurface interpretation (e.g. Figure 2.2A). We then quantify fault slip using terrace folds and compare these to slip estimates implied by the fault scarp record. In this way, we seek to validate the method of using surface fold relief to quantify fault slip by establishing a direct comparison to independent slip constraints from the fault scarp. Moreover, we continue to critically evaluate our subsurface interpretation of fault-bend folding by comparing fault slip gradients across the SJT implied by the terrace deformation to the predictions from fault-bend fold theory (Figure 2.1A).

SURFACE DEFORMATION

Terrace Mapping with High-Resolution Topographic Data

Preserved terraces along the Taxi He valley have recorded localized and distributed deformation across the SJT (Avouac et al., 1993; Molnar et al., 1994; this study). We acquired a 5-m vertical resolution digital elevation model across the Taxi He Valley to correlate terraces across the entire transect of the Tugulu fold (Figure 2.3C). The vertical resolution was improved to 70 cm using 10 differential Global Position System (dGPS) ground truth points. This high-resolution topographic data is capable of precisely defining fault uplift and folding signatures across the entire hanging wall of the SJT over multiple rupture cycles. Based on field observations and various methods of interpreting fluvial terraces (e.g. location, elevation, geometry) we mapped seven distinct terraces in the topography data across the Taxi He valley (Figure 2.6A). In our study, T6 is the youngest mapped terrace and T0 is the oldest. The youngest of these (T4-T6) are present across the entire transect of the thrust sheet, providing three records of both surface folding and surface faulting. Younger terraces are present in isolated remnant locations throughout the valley, but are too discontinuous to confidently correlate over large distances of non-preservation. One of these terraces, T8, provides a lower age constraint for T6. The older terraces (T0-T3) are less continuous, limited to the southernmost dip domains (θ_0-θ_2) along the SJT. However, these markers exhibit significant uplift and folding deformation, providing a long record of SJT fault slip activity.

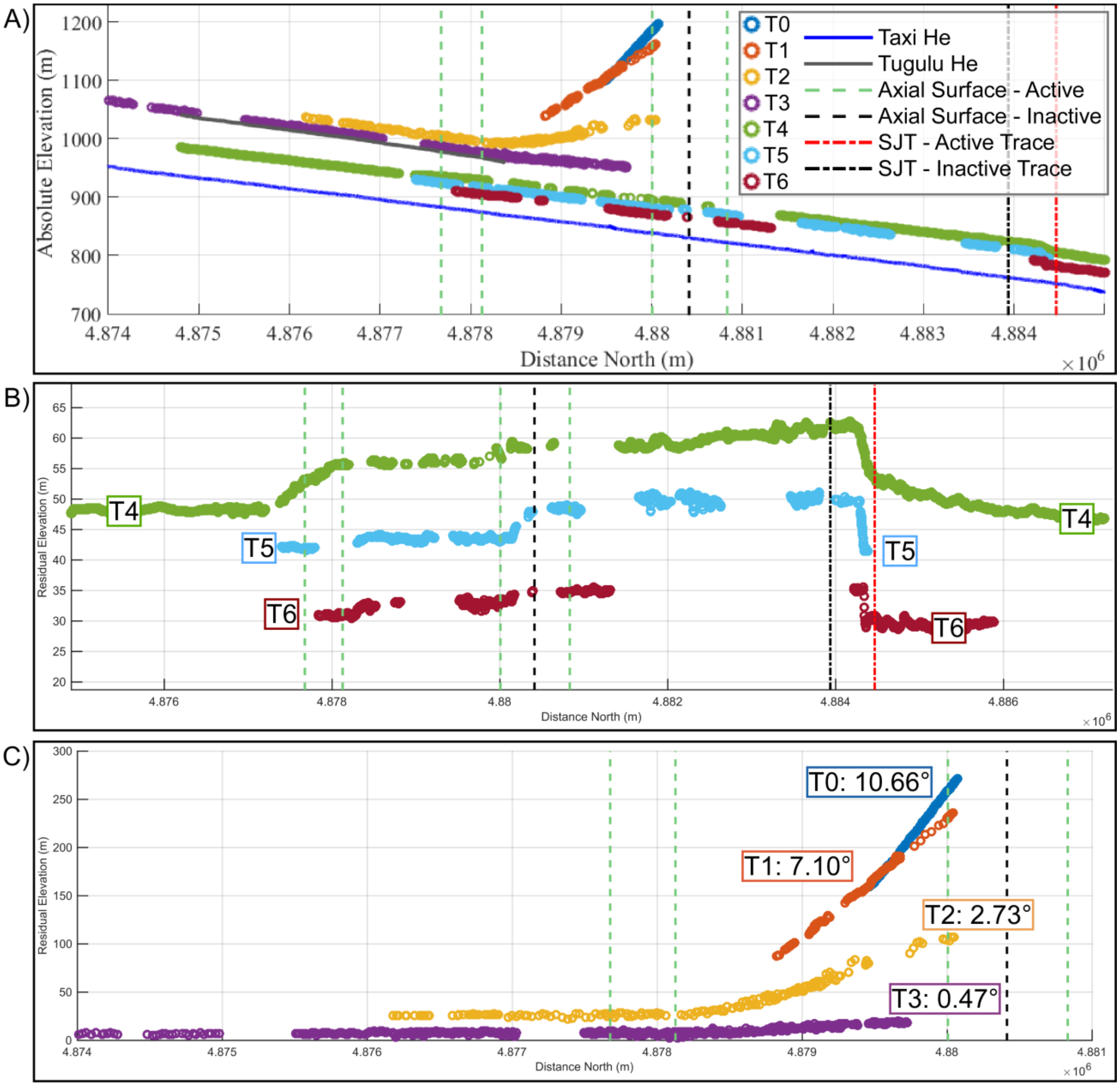

Figure 2.6: A) Raw terrace profiles mapped in digital elevation model (Figure 2.3C). T0 is the oldest mapped terrace; T6 is the youngest. B) Residual profiles of Holocene terraces (T4-T6). Note that each Holocene terrace records surface folding *and* surface faulting deformation. C) Residual profiles of Quaternary terraces (T0-T3). The preserved Quaternary terrace profiles only records surface folding strains. See text for details.

In subsequent sections, our structural analysis utilizes residual terrace profiles, which have had their original depositional gradients removed (Figure 2.6B-C). A brief description of how we mapped terraces and removed the original depositional gradients is provided in Appendix C. We document our assessment of uncertainties related to measurements used to quantify fault slip (e.g. terrace elevation, fault dip) in Appendix D. We note that the loess cap, which often defines terrace treads in southern Junggar (e.g. Figure 2.4C), has been completely eroded from our T0 terrace, suggesting T0 has undergone at least modest amounts of erosion. Thus, any measure of fault slip implied by our T0 profile reflects a minimum estimate of SJT slip since the time of T0 abandonment.

Terrace Geochronology

Ages of terrace abandonment are required in order to obtain rates of surface deformation and associated fault slip rates. Luminescence geochronological methods have proved capable of obtaining reliable absolute age constraints for the lower elevation terraces across southern Junggar, analogous to our T4-T6 terraces (e.g. Poisson, 2002; Poisson and Avouac, 2004; Lu et al., 2010a; Gong et al., 2014). We employ the recently developed post-infrared, infrared stimulated luminescence (pIR-IRSL) methods (Brown et al., 2015; Rhodes, 2015) to date fluvial deposits in each terrace used for our structural analysis. Fluvial deposits are composed of very fine grain to boulder sized clasts. In most locations, the fluvial deposit is overlain by a light tan loess cap. For each terrace we collect 2-5 samples at least 25 cm below the loess cap by driving a 50cm aluminum tube into the fluvial deposit and capping the ends of the full tube, shielding the inner 40+ cm of sample from exposure to sunlight. Samples for T0-T6, T8 terraces were collected in the backlimb of the Tugulu fold with an additional set of samples collected for T4 near the fault scarp in the forelimb of the fold (Figure 2.3C).

Samples were prepared and analyzed using standard procedures for feldspar luminescence in order to obtain the natural luminescence signal of each terrace sample. Single-aliquot regenerative (SAR) dose curves (Murray and Wintle, 2000) were generated for each sample to determine the total radiation dose required to produce the natural luminescence signal measured originally. Bulk and trace element analysis of the surrounding material yields the rate at which samples have been indurated with radiation. This last step provides an approximate age of terrace abandonment. However, we can improve the uncertainties on terrace ages by using knowledge of the depositional environment and the sequential development of terraces. Using standard age estimate methods (e.g. Galbraith et al., 1999), we produce an a priori distribution of probable terrace ages (Figure 2.7). We then run a simulation that assumes stratigraphic consistency between adjacent terraces. The model randomly selects any of the T0-T6, T8 terraces and begins by randomly selecting an age from the prior age distribution. The simulation repeats this step for an adjacent terrace. If the age of the adjacent terrace maintains stratigraphic consistency with the preceding terrace age, the model progresses, repeating the process with subsequent terraces in the model. If an age is not stratigraphically consistent (e.g. T5 > T4), the model repeats the age selection until it either selects a stratigraphically consistent age or it fails a pre-determined number of iterations. Each model run continues until ages for T0-T6 and T8 are obtained, or the model fails. We run 10,000 simulations of this process to produce a posterior age distribution from the successful model simulations (Figure 2.7). This process provides tight age constraints for Holocene-aged terraces. The T0-T3 terraces have higher uncertainties due to fading of the luminescence signal. Moreover, in our posterior simulation described above, present-day is an implicit lower bound for the terrace age; the terrace cannot have a negative age. However, there is not a similar upper-bound for the older terraces, resulting in two effects on our preferred (posterior) age distributions. First, it increases uncertainties for the Quaternary terraces (T0-T3). Second, it skews standard deviations in the positive direction (Figure 2.7). The posterior age probabilities establish terrace ages that are fairly distinguishable from adjacent terraces, with modest 1-σ overlap (Figure 2.7). We note that independent age constraints from alternative geochronological methods (e.g. terrestrial cosmogenic nuclides) would aid in further uncertainty reduction.

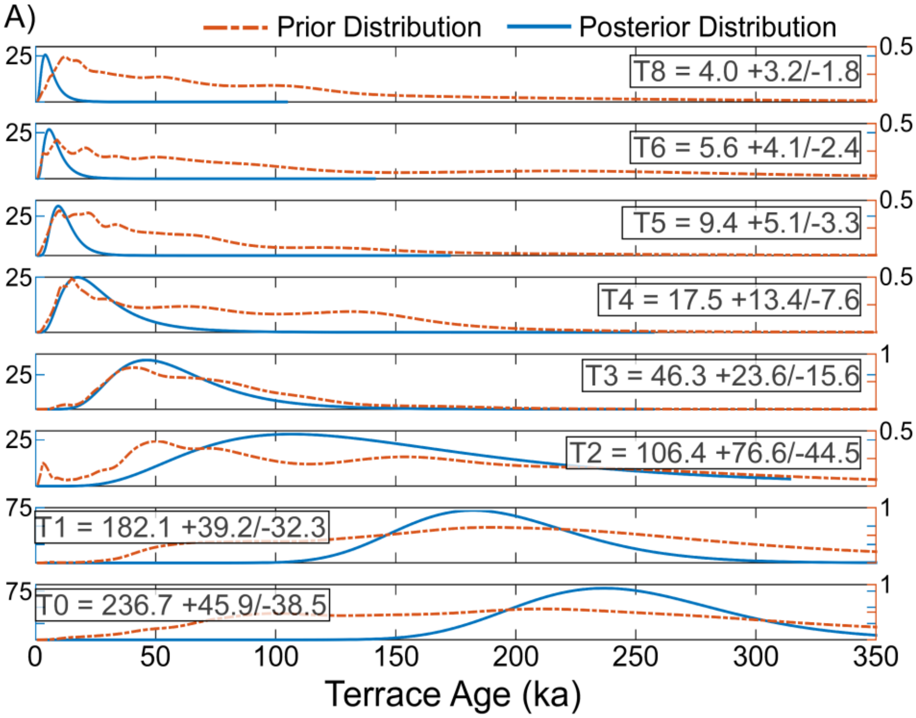

Figure 2.7: Terrace geochronology across the Taxi He valley. See text for details.

Fault Slip Estimates from Surface Deformation

Surface Faulting

As documented by Avouac et al. (1993), there is a prominent fault scarp delineating the surface trace of the active SJT splay along the forelimb of the Tugulu anticline. The surface fault dip slip (u_j) required to produce the observed amount of terrace uplift relative to the footwall position (h_j) is given by:

$$\boldsymbol{u_j} = \frac{\boldsymbol{h_j}}{\boldsymbol{\sin\theta_j}} \qquad (1)$$

where θ_j is the dip of the underlying fault segment relative to horizontal, measured in degrees, and h_j is the total structural relief above dip domain j, given by:

$$\boldsymbol{h_j} = \boldsymbol{z_j} - \boldsymbol{z_{fw}} \qquad (2)$$

where z_x is the elevation of the unfolded terrace within dip domain j, and z_{fw} is the footwall elevation of the terrace (Figure 2.8).

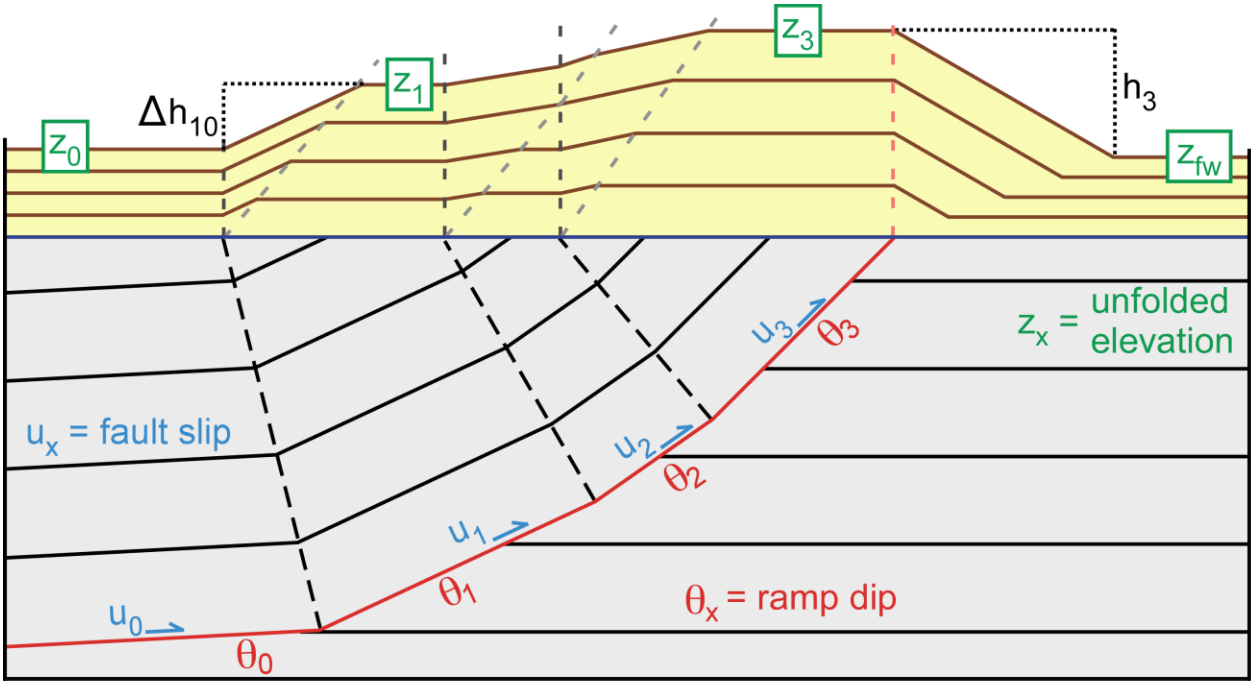

Figure 2.8: Schematic illustration of deformed fluvial terraces across a fault-bend fold and the measurements taken of each terrace for estimating the magnitude of fault slip since the time of terrace abandonment. See text for details.

Surface Folding

Actively uplifting structures often do not have a preserved record footwall terraces due to footwall aggradation (Lavé and Avouac, 2000; Yue et al., 2011; Le Béon et al., 2014). Without a footwall level, estimates of fault slip from surface faulting require assumptions about base level changes and sedimentation rates to estimate the burial depth of the footwall terrace relative to the present-day stream bed. This method has been shown to yield reasonable estimates of fault slip when base level changes have been considered thoroughly (e.g. Lavé and Avouac, 2000).

However, the traditional method of quantifying fault slip from surface fault uplift by (1) can be generalized to yield estimates of fault slip at depth from fold scarps or fault scarps. This method is independent of base level changes when applied to fold scarps (e.g. Yue et al., 2011; Le Béon et al., 2014), avoiding additional uncertainties associated with estimates of z_{fw} if a terrace is not preserved in the footwall (e.g. e.g. Lavé and Avouac, 2000). The structural relief produced across two dip domains, *i* and *j*, provides an estimate of slip by:

$$\boldsymbol{u_j = \frac{\Delta h_{ji}}{\sin\theta_j - \sin\theta_i}} \qquad (3)$$

where

$$\boldsymbol{\Delta h_{ji} = z_j - z_i} \qquad (4)$$

The generalized forms in (3) and (4) reduce to (1) and (2) when dip domain *i* refers to the footwall of the fault (i.e. $\theta_i = 0°$). The generalized formula for quantifying fault slip from terrace relief in (3) is applicable across one or multiple fault bends across a thrust sheet; *j-i* need not equal 1. Thus, if a thrust sheet has several fault bends, such as the SJT (Figure 2.5), (3) may yield several estimates of fault slip.

We have precise constraints on the footwall positions of the Holocene terraces, T4-T6 (Figure 2.6B), but the Quaternary terraces, T0-T3, are only preserved as fold scarps (Figure 2.6C). In the following section, we test the accuracy of (3) for estimating magnitudes of fault slip from only fold scarp relief by directly comparing it to measures of fault slip implied by the fault scarps using (1).

INTEGRATED RECORDS OF ACTIVE THRUST SHEET DEFORMATION

Holocene Fault Activity

Fault Scarp Estimates of Fault Slip

Structural relief of the T4 terrace across the Taxi He fault scarp suggests ~15 m ± 1.2 m of vertical throw on the SJT (Figure 2.6B) since it was abandoned in the early Holocene (Figure 2.7). The progressive decrease in structural relief with decreasing terrace age implies a record of multiple rupture events on the SJT throughout the Holocene. We use (1) to calculate total fault slip on the SJT since the time of terrace abandonment for each Holocene terrace and our constraints of subsurface fault dip to (Table 2.1). This surface faulting record suggests at least 21.4 m ± 2.4 m of fault slip on the SJT during the Holocene.

TABLE 2.1. Surface Faulting Deformation

	T4	T5	T6
Age (ka)	17.50	9.40	5.60
z_4 (m)	61.80	50.02	35.13
z_{fw} (m)	46.83	41.52	29.72
h_4 (m)	14.97	8.50	5.41
θ_4 (°)	44.50	44.50	44.50
u_4 (m)	**21.4**	**12.1**	**7.7**

Fold Scarp Estimates of Fault Slip

We calculate the fault slip required to produce the measured structural relief across all possible combinations of dip domains for the T4-T6 using (3). As discussed above, our interpretation of the SJT geometry and its hanging wall fold reflects fault-bend folding (Suppe, 1983). For our case of ~parallel hanging wall strata and underlying fault dip, fault-bend folding predicts no change in slip across a synclinal fault bend (Suppe, 1983). Therefore, we should expect a single magnitude of fault slip to explain all of our measures of structural relief and change in fault dip used in (3) for a given terrace. In Figure 2.9A, we plot structural relief versus change in fault geometry and apply a linear regression to each terrace dataset that runs through the origin, reflecting no relief for no slip. The slope of each best-fit function yields the magnitude of slip that best describes the terrace fold scarps and fault dip data. The low variance between the linear models and the data implies no change in fault slip across the entire hanging wall of the SJT among the fold scarps (Figure 2.9A), indicating that a single magnitude of fault slip can readily explain all of the observed fold scarps for each Holocene terraces (T4-T6).

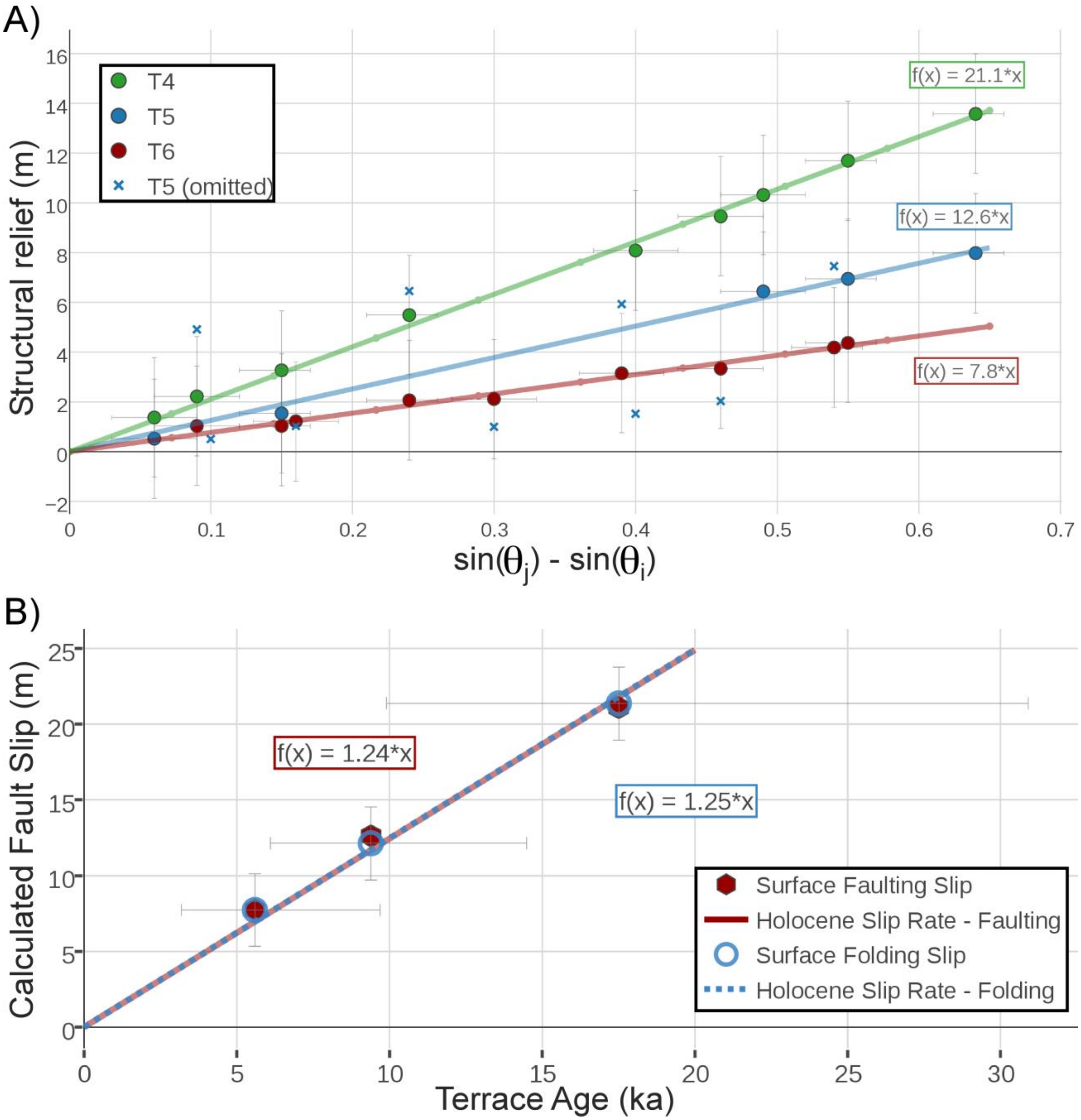

Figure 2.9: A) Fault slip estimates from Holocene terrace fold scarps across the Tugulu structure using (3). The slope of the best-fit linear regression line yields an estimate of total fault slip experienced by that terrace. The goodness of fit of each regression to the terrace folding data implies a single magnitude of fault slip readily explains all of the fold scarp deformation, consistent with the prediction from fault bend folding (Suppe, 1983). B) Estimates of Holocene fault slip and slip rates from terrace faulting and terrace folding are indistinguishable, yielding an estimate for Holocene slip rate of ~1.2-1.3 mm/yr.

The fold scarps preserved in the T5 record yield consistent fault slip values across dip domains x=0, 3 and 4 (Figure 2.9A). We note that the uplift preserved across the T5 fold scarps corresponding to dip domains 1 and 2 is less than the relief preserved for T6 in the same dip domains (Figure 2.6B). As T5 is older than T6 in both an absolute (Figure 2.7) and relative (Figure 2.6A) sense, T5 must have experienced at least as much fault slip as T6. However, the regions where relief is greatest suggests T5 has been deformed by more SJT fault slip than T6 (Figure 2.6B), consistent with the result from the fault scarp data (Table 1). This suggests some of the uplift experienced by T5 has been removed in dip domains 1 and 2. Potential mechanisms to remove terrace fold relief may require lateral erosion, perhaps slake-driven lateral incision (Johnson and Finnegan, 2015), or, if the Taxi He was transporting sufficiently erosive bedload at that time, downstream sweep erosion (Cook et al., 2014). Whatever the mechanism may have been, the consistency of fault slip suggested by all of the slip measures by T4 and T6 as well as the T5 data used in Figure 2.9A suggest the two depressed uplift signals in the T5 profile are likely underestimating total SJT fault slip.

When we compare the magnitudes of fault slip derived using (1) and (3) using the fault scarp and fold scarp data, respectively, the results are indistinguishable (Figure 2.9B). This is further consistency with our fault-bend folding interpretation for the hanging wall of the SJT. A linear regression to these data suggest a fairly constant Holocene slip rate on the SJT of 1.2-1.3 mm/yr (Figure 2.9B).

We have established that quantifying fault slip from terrace folds can accurately reflect total fault slip at depth (Figure 2.9). We suggest this provides confidence for using folding recorded by growth strata or terraces to quantify fault slip on blind thrust sheets (e.g. Dolan et al., 2003; Benesh et al., 2007). When possible, seismic hazards assessments should employ this method using as many different measures of fold relief as available in order to evaluate the potential for spatial gradients in slip along an active thrust sheet (e.g. Figure 2.1). In our case, a fault-bend fold, we can state confidently that a single measure of fault slip anywhere in the hanging wall would have been yielded an accurate measure of fault slip at depth. Yet, we could not have stated this with confidence if we only used a single fold scarp in our analysis. We only validate the lack of slip variation by producing a complete record of surface folding and surface faulting deformation across the entire SJT in our study area.

Quaternary Fault Activity

The T0-T3 terraces provide a record of Late Quaternary surface folding across the Tugulu backlimb (Figure 2.6C; 2.7). While the Holocene terraces would only record a few earthquakes equivalent to the 1906 Manas, China event, these older terraces provide long-term records of uplift due to fold growth and fault activity on the SJT – likely the products of hundreds of 1906-equivalent ruptures. Given the discontinuous nature of these older terraces, they do not record fault offset. Therefore, we use (3) to constrain the fault slip required to produce the observed fold relief for T0-T3 (Table 2.2). The z_0 elevation – the residual elevation above the detachment – for both T2 and T3 is preserved in our terrace records (Figure 2.6C). To estimate z_0 for T1 and T0, we assume the rate of incision implied from T2 to T3 has been constant since the abandonment of T0. Although we do not have evidence for a constant incision rate from ~250-100 ka, this method should yield a reasonable approximation for the structural relief developed before T1 abandonment. As described previously, the magnitude of fault slip from the T0 profile is likely a minimum constraint, given the evidence for erosion. Our calculations from (3) suggest a minimum of ~525 m of fault slip on the SJT over the past ~250 kyr (Table 2.2). Before we discuss the long-term slip rate history on the SJT implied by our terrace data, we discuss the folding kinematics implied by the T0-T3 terrace geometries (Figure 2.6B), which appear to deviate from the predictions of kinematic fault-bend fold theories (Figure 2.2A-B). In doing so, we attempt to develop a method for quantifying fault slip from terrace fold dips, which, if successful, will provide a more accurate estimate for fault slip implied by the T0 terrace profile.

TABLE 2.2. Quaternary Folding Deformation

	T0	T1	T2	T3
Age (ka)	256.7	182.1	106.4	46.3
z_2 (m)	271.30	234.47	104.97	19.19
z_0 (m)	66.04	49.26	26.16	7.44
Δh_2 (m)	205.26	185.21	78.81	11.75
$\sin(\theta_2) - \sin(\theta_0)$	0.40	0.40	0.40	0.40
u_4 (m)	**512.0**	**462.0**	**197.1**	**29.31**

Quaternary Terrace Fold Kinematics

The Quaternary terraces preserved across the backlimb of the Tugulu fold exhibit a fanning of limb dips, with older terraces dipping more steeply than younger terraces (Figure 2.6C). Where preserved, these terraces acquire their dips over a region of finite width, coincident with synclinal axial surfaces that reflect the SJT increasing its dip from 3.4° to 27.4°. The variable limb dips exhibited by these Quaternary terrace folds are remarkably planar. These observations suggest T0-T3 folds have developed – at least in part – by limb rotation. Limb rotation is a folding mechanism that describes fold limbs which progressively increase their dip with increasing fault slip. Fault-bend folding theories (Suppe, 1983; Suppe et al., 1997) predict these structures grow exclusively by kink-band migration (Figure 2.2A-B). Kink-band migration is a folding mechanism whereby folds acquire a constant dip after passing over a fault bend – instantaneously (Figure 2.2A) or over some region of finite width (Figure 2.2B) – and widen at this constant dip with increasing fault slip.

Observations of progressive limb rotation across fault-related folds have led to the development of numerous fault-related fold variants based in part on the original fault-bend fold theory. These commonly invoke an axial surface zone of some finite width (e.g. Erslev, 1986; Suppe et al., 1997; Seeber and Sorlien, 2000), and may invoke additional folding mechanisms that involve limb rotation, such as trishear (Erslev, 1993; Allmendinger, 1998; Cristallini and Allmendinger, 2002; Brandenburg, 2014). Simple and pure shear fault-bend folding models describe structures that grow by a combination of kink-band migration and limb rotation (Suppe et al., 2004; Hardy and Connors, 2006).

More recently, studies have explored the possibility that structures may deviate from the strict kinematics of fault-bend folding theory under certain conditions (Benesh et al., 2007; Benesh, 2010). These studies have employed mechanical forward models using the discrete element modeling (DEM) technique. These models readily produce fault-bend folds that grow by a combination of kink-band migration and limb rotation – referred to herein as hybrid folding– as strata are displaced across a discrete fault bend (Benesh et al., 2007; Benesh, 2010). This behavior offers the prospect of reconciling our observations that Holocene slip on the SJT is consistent with fault-bend folding kinematic predictions of slip magnitudes across the entire hanging wall (Figure 2.1A, 2.5, 2.9B) while the fanning of limb dips in the Quaternary terrace record implies a component of folding by limb rotation (Figure 2.6C).

A MECHANICAL MODEL OF THRUST SHEET DEFORMATION

Model Description

Following the work of Benesh et al. (2007) and others (e.g., Strayer et al., 2004; Benesh, 2010; Hughes and Shaw, 2015; Morgan, 2015), we produced a mechanical model of deformation within a thrust sheet using a discrete element model (DEM) to help guide our interpretations of folding kinematics for the hanging wall of the SJT, including the T0-T3 terraces. The DEM method is able to replicate natural brittle-plastic deformation processes such as folding, frictional sliding, fracture growth, and the influence of mechanical stratigraphy (e.g., Cundall and Strack, 1979; Morgan, 1999; Strayer et al., 2004) that likely influence the manner of deformation during natural fault-related folding. We created our model using the 2-D Particle Flow Code (PFC) numerical modeling package, which describes granular behavior of linear elastic particles with frictional contacts. The code employs a method by which circular balls interact at an infinitesimally small contact. These contacts can replicate both shear and tensional bonding between particles. If bonds are broken, balls will interact and can slide, governed by Coulomb frictional sliding behavior. In addition, physical rock properties such as density, elastic moduli, and friction can be prescribed. Moreover, forces are implemented to models, such as gravity and translating boundary walls. Translating walls are often employed as displacement boundary conditions to drive deformation. For a more detailed description of the DEM method and PFC code applied to studies of active deformation and folding kinematics, we direct the reader to Benesh (2010); Hughes et al. (2014); and Morgan (2015).

We define a 24° dip change along the fault in our mechanical model to replicate folding of the T0-T3 Quaternary terraces across the SJT, where they are preserved (e.g. Figure 2.5, 2.6C). The model includes a 12 km long detachment that steps up to a thrust ramp dipping 24° (Figure 2.10A). We deposit pre-growth strata to the hanging wall of our fault model in 500 m thick layers, following the same settling procedure of Benesh et al. (2007), allowing each layer to reach a state of static equilibrium following deposition. Between pre-growth layers, we deposit 125 m thick sections that have smaller ball radii, no friction and lack bonding. These weak layers are employed to promote flexural slip during deformation, which enables the structure to deform in a manner consistent with fault-bend folding (Suppe, 1983; Benesh, 2010). We deposit seven layers of pre-growth and six flexural slip surfaces (Figure 2.10A). A boundary condition is applied to the leftmost boundary wall to translate along the detachment fault at a constant rate of 1 m/s. After each 250 m interval of fault slip, we deposit a layer of growth strata to a thickness that is 100 m higher than the mean elevation of the structural crest. Growth strata aid in recording the kinematics of the fold growth and also serve to limit effects such as slumping and minor extension that can develop at the top of the hanging wall. The material properties prescribed for our model are summarized in Table 2.3.

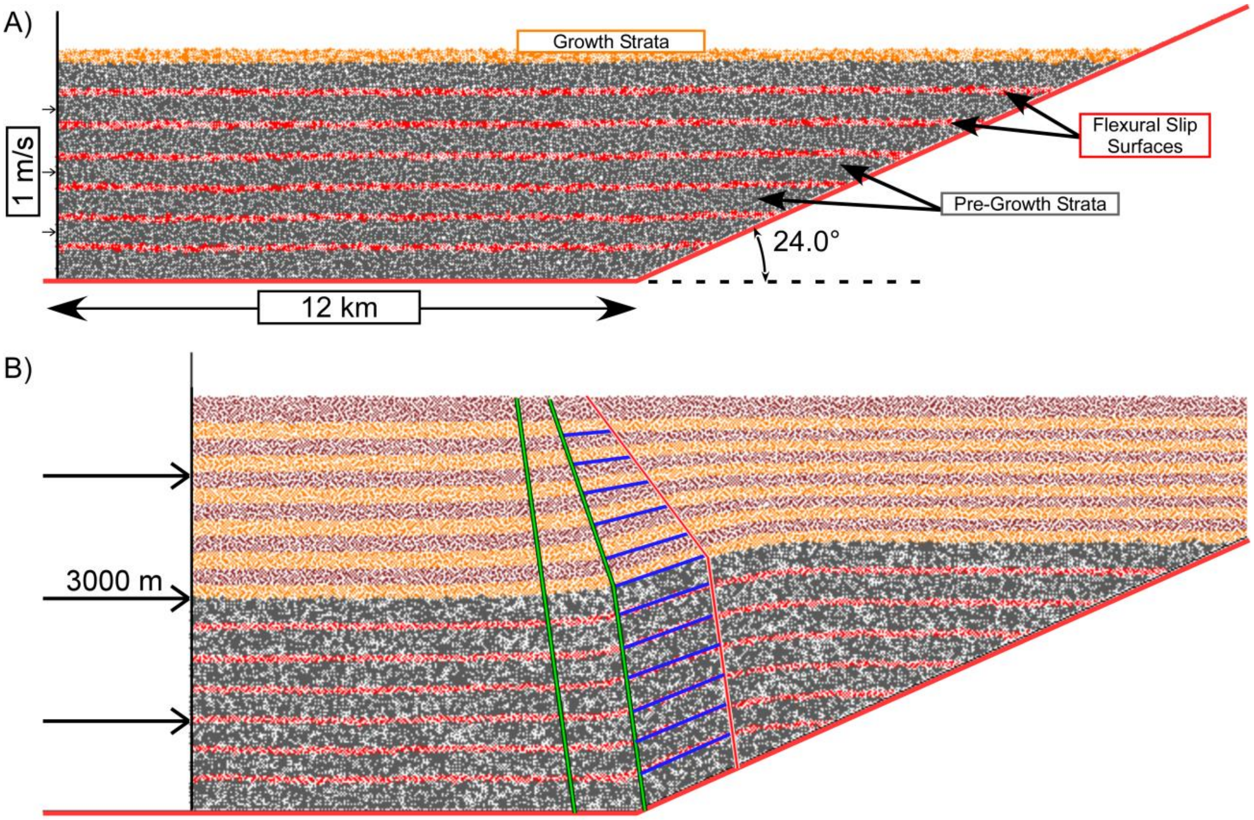

Figure 2.10: Mechanical model of a fault-bend fold (Benesh et al., 2007; Benesh, 2010). A) Set-up of the model geometry. Note the change in fault dip is consistent with the dip change across the southern most fault bends of the SJT (Figure 5). Model parameters summarized in Table 2.3. B) Final result of the mechanical model after 3000 m of fault slip. Noteworthy observations include 1) pre-growth strata that parallel the fault ramp, consistent with kinematic prediction; 2) an upward narrowing growth fold triangle, which indicates folding by kink-band migration, consistent with the kinematic predictions; 3) uplift and folding is consistently initiated before reaching the fault bend, which is not predicted by the kinematic theory; and 4) a fanning of limb dips, indicating folding by limb rotation, which is not predicted by fault-bend folding theories. See text for details.

There are many similarities between our mechanical model result and kinematic fault-bend fold theory (Suppe, 1983). In the final state of deformation (Figure 2.10B), pre-growth strata parallel the underlying thrust ramp, which is the kinematic prediction for our initial model geometry. As a result, slip on the fault ramp is generally constant and consistent with the structural relief across the fold in its hanging wall. This behavior further validates (3) to calculate slip on the SJT from the fold scarp relief of deformed terraces. In the growth strata of our model, we observe a narrowing upward growth triangle (Figure 2.10B), which is diagnostic of fold growth by kink-band migration - the mechanism invoked by fault-bend folding theory (Suppe et al., 1992; Shaw and Suppe, 1994). However, we observe additional details that reflect important departures from the kinematic expectations, consistent with similar studies (Benesh et al., 2007). Most notably, there is a shallowing upward of limb dips in growth strata, suggesting the hanging wall has deformed by a component of limb rotation. Moreover, we observe a distributed zone of folding that has developed to accommodate fault slip across the discrete bend in the thrust sheet at depth. This results in a much wider region of folding than generally is described by the kinematic theory.

TABLE 2.3. PHYSICAL PROPERTIES OF THE MECHANICAL FAULT-BEND FOLD MODEL

Physical property	Pre-growth strata	Flexural slip surfaces	Growth strata	Fault surfaces	Boundary wall
Density (kg/m^3)	2500	2500	2500	n/a	n/a
Ball radii (m)[†]	30-40	22.5-30	22.5-30	n/a	n/a
kn (N/m)	$6.0*10^9$	$6.0*10^9$	$6.0*10^9$	$6.6*10^9$	$6.6*10^9$
ks (N/m)	$6.0*10^9$	$6.0*10^9$	$6.0*10^9$	n/a	n/a
μ[§]	0.30	0.00	0.30	0.10	0.45
E (GPa)	3.0	3.0	3.0	3.3	3.3
σ_c (MPa)[#]	10	0	10	n/a	n/a
τ_c (MPa)[#]	600	0	600	n/a	n/a
Layer thickness (m)	500	125	~250	n/a	n/a

[†] Radii are randomly generated from a uniform distribution bounded by prescribed max and min.

[§] Contact friction.

[#] Contact bond strength; selected from a Gaussian distribution about the prescribed mean value.

Our mechanical fault-bend fold model accommodates shortening during structural growth in part by limb rotation (Figure 2.10B). Thus, the fanning of dips exhibited by T0-T3 (Figure 2.6C) remains consistent with fault-bend folding when stresses and mechanical stratigraphy are considered. To quantify how bed dips evolve in the model, we record fold dip and total slip experienced for each bed in both growth and pre-growth sections following each 250 m slip interval. For each strata type, we calculate the average dip for a given amount of fault slip (Figure 2.11A). We find that both pre-growth and growth layers develop their dips incrementally (Benesh, 2010), reflecting a component of fold growth by limb rotation throughout the hanging wall of our mechanical fault-bend fold model (Figure 2.11A). This pattern of dip evolution was a robust feature for growth and pre-growth strata in all of the models we tested. We find that these relationships are generalized by a second-order polynomial functions that passes through the origin, reflecting zero slip and dip (Figure 2.11A). The precise nature the dip evolution – governed by the two constants in the functional form – will vary as a function of layer strength, thickness, and the spacing of flexural slip surfaces. However, all of the models we tested – in addition to those of Benesh et al. (2007) and Benesh (2010) – involve a component of fault-bend folding by limb rotation in both growth and pre-growth strata, similar to the implied kinematics of the T0-T6 terraces in our study area (Figure 2.5, 2.6, 2.9).

Deriving Fault Slip from Terrace Dips

The pre-growth strata generally develop folds much faster than growth strata in this DEM approach (Benesh et al., 2007). In addition, variations in mechanical stratigraphy of a DEM model can yield changes in the precise form the quadratic dip-slip functional relation described above. This variability presents a challenge for determining the appropriate way to relate bed dips to fault slip in natural structures, given that we generally lack precise knowledge of these mechanical properties. Thus, we suggest an approach that employs fitting a second-order polynomial function to data from the natural structure. Specifically, terraces that preserve both limb dip and structural relief can be used directly in this fitting procedure. For the SJT, this information is available for the T1-T4 terraces (Figure 2.6). We omit T0 from the fitting procedure due to the potential it has undergone significant erosion, as described above. In addition, we supplement our natural terrace dataset with an upper constraint on the critical slip value required to produce the maximum allowable dip, which in our model and the SJT is limited by the ramp dip. The critical slip for the SJT is constrained by pre-growth fault offset across the SJT to be ~2800 m (Guan et al., 2016; their Figure 4). Thus, the Tugulu pre-growth strata require no more than ~2800 m of fault slip to achieve their maximum dip. By incorporating this critical slip and maximum pre-growth dip relation, along with the other direct constraints from terraces that preserve both dip and uplift, we suggest that it’s possible to develop a robust relationship between terrace dip and slip.

We note that growth strata may have a different critical slip than pre-growth, as discussed above (Figure 2.11A). However, terraces are merely passive strain markers. Thus, it seems reasonable that they will be governed by the dip-slip relation of whichever stratigraphic interval they reside within. In our case, the SJT has incised into the pre-growth strata, leaving behind terraces within the Tugulu pre-growth section. Thus, we suggest the pre-growth critical slip value serves as an effective constraint for our terrace data. Our work here, as well as that of Benesh (2010), consistently found that growth layers acquire fold dips more gradually than pre-growth. Thus, magnitudes of fault slip we define by the functional form derived using the pre-growth critical slip value will yield a minimum slip estimate for the terrace data. This reflects uncertainty in how the mechanical stratigraphy of the fluvial deposits overlying the pre-growth may fold precisely. Regardless of this effect, it’s reasonable to suggest the pre-growth critical slip is not greater than the critical slip for the terrace folds.

We define a dip-slip relationship for the Quaternary folds in the backlimb of the Tugulu structure. The constraints for this relationship include dip and slip for the T1-T4 terraces, the pre-growth strata, and the origin, with the origin reflecting no dip for zero fault slip. The functional form of the 2nd-order polynomial describing the terrace dip-slip relation yields a tight fit to the data, suggesting it is a viable path to describe the history of fold growth for the terrace data. In addition, this dip-slip relation confirms our observation that the slip derived from the T0 structural relief will underestimate total slip. However, we can use the observed T0 dip magnitude to estimate the total amount of slip that has occurred on the SJT since the time of T0 abandonment (Figure 2.11B). Finally, the tight fit to the terrace data using the pre-growth critical slip magnitude implies that this is a reliable measure for the critical slip for our terrace folds.

We conclude the slip estimates from uplift of Holocene terraces (T4-6) – which are consistent with kinematic fault-bend fold theory (Suppe, 1983) – can be reconciled with the fanning of limb dips in Quaternary terraces (T0-T3) – which deviate from kinematic fault-bend fold theory (Suppe, 1983) – through a mechanical fault-bend fold model that grows by a combination of limb rotation and kink-band migration (Figure 2.11B). We do not advocate that any specific mechanical model can be used to uniquely define the dip-slip relation for a specific natural structure. In contrast, we suggest that the general functional form of this relationship can be effectively described by a second-order polynomial relation that fits through the origin. This offers a generalized approach by which limited data from natural folds – surface folds or buried growth strata– may be used to develop a quantitative relation between fold geometry and fault slip at depth (Figure 2.11).

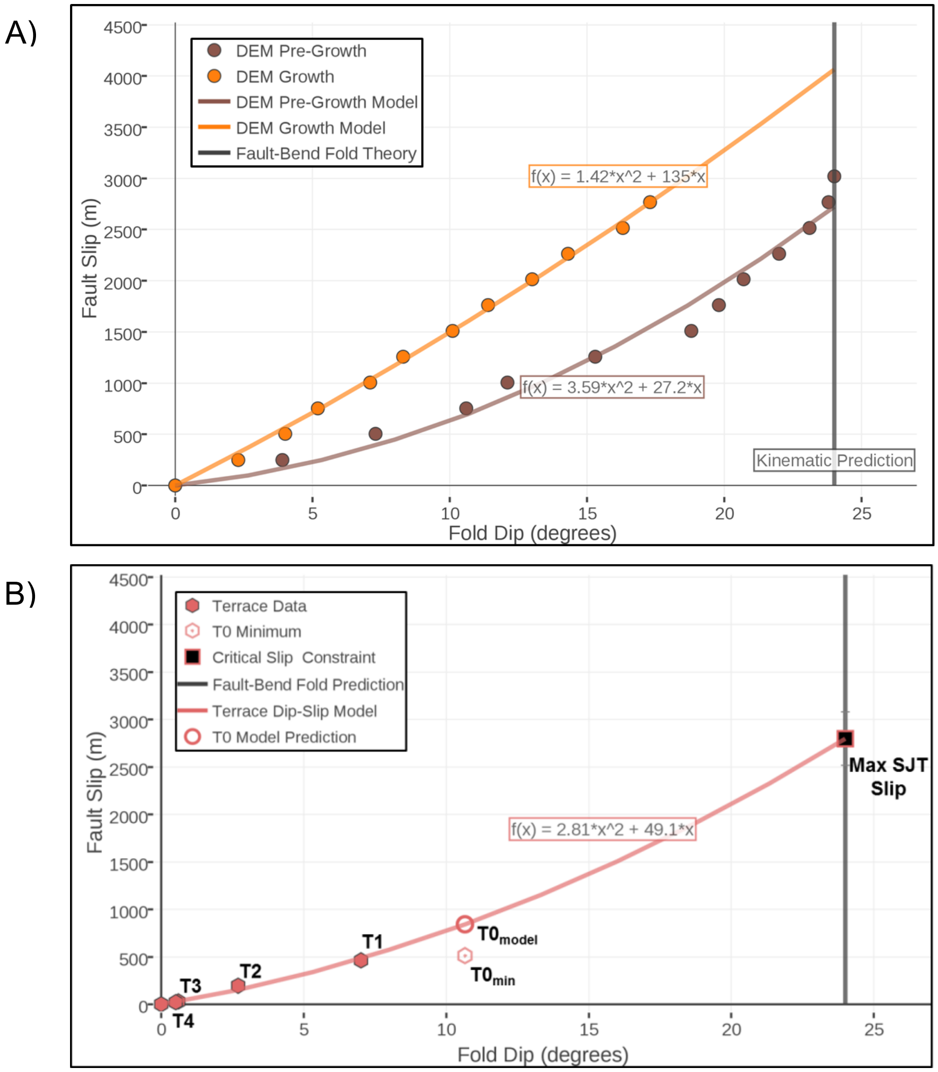

Figure 2.11: A) Dip-slip relations for growth and pre-growth strata in the DEM model can be generalized as a 2^{nd}-order polynomial function fit through the origin. B) Estimates of fault slip versus the observed fault-dip for T1-T4 and the pre-growth constraint for the critical slip to develop the maximum hanging wall fold dip (Guan et al., 2016). The slip for T0 can be estimated directly from this functional form. Fault slip for T1-T4 is calculated in Table 2.2. See text for details.

250 KYR RECORD OF ACTIVE THRUST SHEET DEFORMATION

Based on our analysis of the kinematics governing the dip-slip relation for the hanging wall of the SJT, the slip estimates derived from (3) for the T4-T6 terraces, and our new terrace geochronology (Figure 2.7), we have developed a detailed history fault slip rate on the SJT (Figure 2.12). Specifically, the mean slip rate for the SJT has decelerated from a maximum of ~7.0 mm/yr in the Late Quaternary, to a mean slip rate of ~1.3 mm/yr throughout the Holocene

(Figure 2.9; 2.12). We formally evaluate this conclusion of a decelerating SJT slip rate from the Late Quaternary to the Holocene by performing an f-test on the functional forms fit to the terrace data that considers uncertainties in our estimates of fault slip as well as the terrace age uncertainties (Appendix D). In this assessment, a 2nd-order polynomial function fits our terrace data more accurately than a constant slip rate function fit to all of the data. Thus, although the actual SJT slip rates may differ from the preferred values reported here within the range of our uncertainties, our conclusion of a decelerating slip rate from the Late Quaternary to the Holocene remains robust.

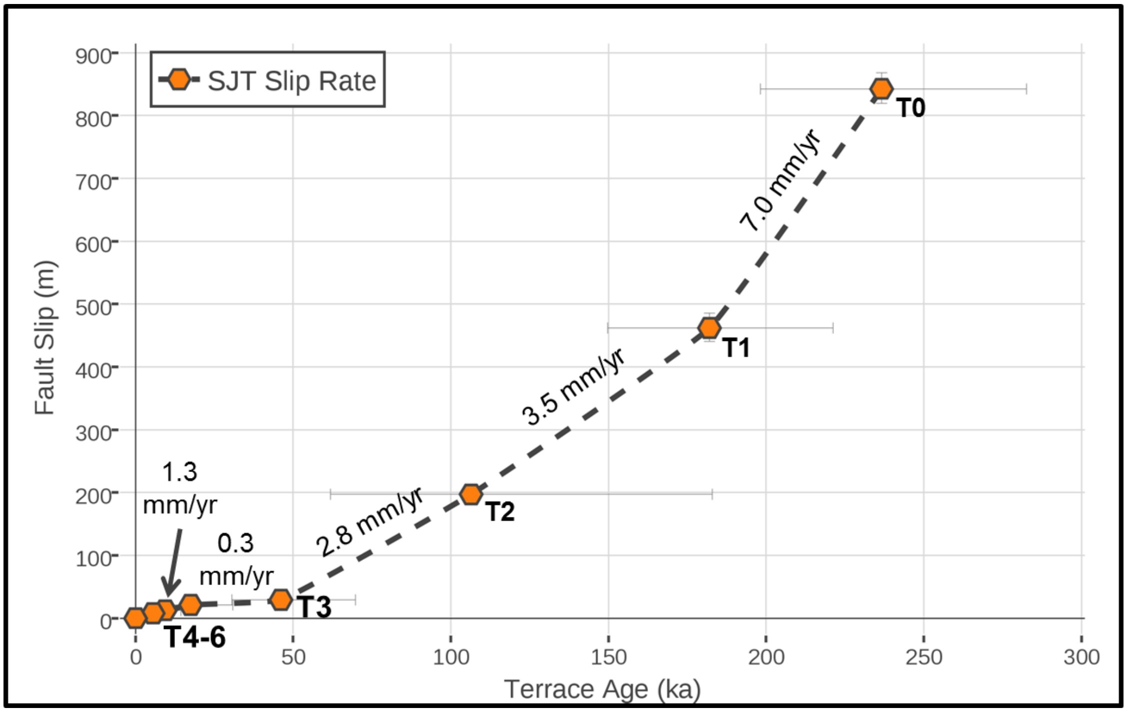

Figure 2.12: SJT slip rate from ~250 ka-present. The slip rate on the SJT has decelerated from Late Quaternary (maximum preferred value = ~7.0 mm/yr) to the Holocene (preferred value = ~1.3 mm/yr). See text for details.

Our preferred Holocene slip rate represents ~25% of the geodetically measured shortening across the Tian Shan rangefront at the 86° latitude of our studied area (Meade, 2007). Thus, the SJT currently serves as a principal structure for accommodating shortening across the eastern Tian Shan in. A faster slip rate on the SJT in the Late Quaternary implies: 1) the regional shortening rate has decreased over the past 250 kyr, 2) deformation formerly accommodated on the SJT has shifted to structures toward the hinterland, within the Tian Shan ranges, or 3) a combination of 1 and 2. Moreover, the dynamic history of SJT slip rate suggests that single measures of fault slip rate for active thrust sheets may not be adequate to properly characterize past or present-day slip rates. Thus, in addition to considering spatial slip gradients in thrust sheets (Figure 2.1), adequate seismic hazards studies should consider temporal variations as well (Figure 2.12).

CONCLUSIONS

Through a unique case study integrating deformed fluvial terraces, feldspar luminescence geochronology, and structural analysis facilitated by seismic reflection data and mechanical forward models, we have developed a new method of extracting detailed histories of fault slip and slip rate from folds in thrust sheets. By combining kinematic and mechanical modeling methods, we developed quantitative relationships between fold relief, fold limb dip, and slip that enabled us to extract a ~250 kyr history of deformation and fault activity on the SJT from measures of terrace fold dip and uplift. These methods can be readily employed in regions of active convergent tectonics to delineate active thrust faults, growing folds, and, thus, understand their histories of deformation over multi-rupture timescales. Moreover, methods that consider more complete records of deformation over multiple rupture cycles provide unique insights into the mechanisms of natural fold growth in relation to thrust faulting. With proper consideration of the potential for spatiotemporal fault slip variations (e.g. Figure 2.1, 2.12), hazards assessments can provide more accurate details of fault activity, paleoearthquake magnitude and slip rates to better reduce the risk to life and property in active thrust belts.

CHAPTER 3

Structural inversion, imbricate wedging, and out-of-sequence thrusting in the southern Junggar fold-and-thrust belt, northern Tian Shan, China[3]

Introduction

The southern Junggar basin is the northern foreland fold-and-thrust belt of the actively uplifting Tian Shan ranges in northwestern China (Figure 3.1), representing a northern extension of active Himalayan (e.g. Molnar and Tapponnier, 1975) and potentially Arabian (Yin, 2010) convergent tectonics. Southern Junggar continues to undergo shortening at present, indicated by Holocene-aged terrace deformation and seismic activity attributed to slip on the Southern Junggar Thrust (SJT) (Avouac et al., 1993; Burchfiel et al., 1999; Lu et al., 2010). This fold-and-thrust belt is composed of a series of east-west plunging, imbricated fault-related folds underlain by both surface-emergent and blind-thrust ramps that shallow to multiple detachment levels across the basin (e.g. Avouac et al., 1993; Burchfiel et al., 1999; Charreau et al., 2008). The structures across this complex fold-and-thrust belt have been the targets of petroleum exploration for decades, leading to the discovery of several oil and gas fields. These include the Qigu, Tugulu and Huoerguosi fields (Figure 3.1), which produce from Cretaceous and Eocene reservoirs overlying Jurassic (Clayton et al., 1997; Ding et al., 2003) and perhaps Permian (Carroll et al., 1992) hydrocarbon sources.

The southern Junggar thrust belt structures can be grouped into three east-west trending fold rows (Figure 3.1). The southernmost structural trend includes the Nananjihai and Qigu

---

[3] A version of this chapter was published in *AAPG Bulletin* in 2016

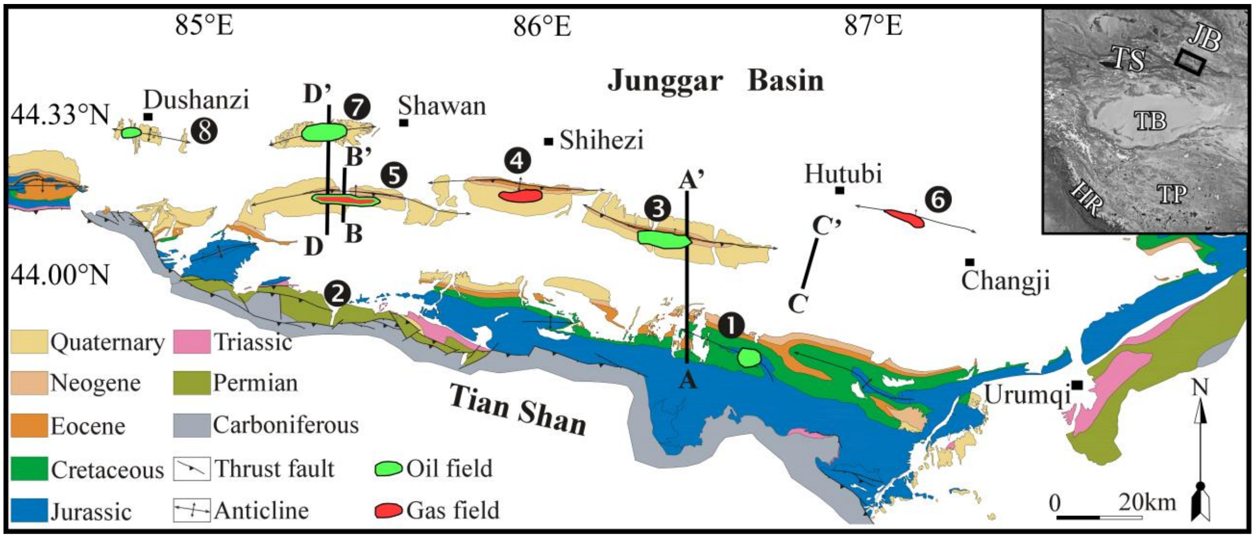

Figure 3.1: Geologic map of the southern Junggar basin and the region's prominent anticlinal structures: 1) Qigu; 2) Nananjihai; 3) Tugulu; 4) Manas; 5) Huoerguosi; 6) Hutubi; 7) Anjihai, 8) Dushanzi. Oil and gas fields are outlined in green and red, respectively. Black lines indicate geologic sections presented in this study. Inset provides satellite imagery of western China and surrounding areas with the study area outlined in orange. JB = Junggar Basin; TS = Tian Shan; TB = Tarim Basin; TP = Tibetan Plateau; HR = Himalayan Rnages. Inset imagery from Google Earth and US Dept. of State Geographer.

anticlines, and represents the northern rangefront of the Tian Shan (Deng et al., 1999; Lu et al., 2010). The Qigu fold provides a structural trap for the Qigu oil field, which produces from Cretaceous clastic reservoir sequences (Fan et al., 2012). The central fold trend is composed of the Tugulu, Manas, and Huoerguosi anticlines, which are doubly plunging, en echelon folds connected through soft linkages (Stockmeyer et al., 2014). The Tugulu and Huoerguosi structures provide traps for oil and gas accumulations in Eocene clastic reservoirs. The northernmost fold row consists of the Hutubi, Anjihai and Dushanzi folds. The Hutubi anticline has no surface expression, but serves as the trap for a gas field. Despite the many discoveries across southern Junggar, development and production operations have run into many unexpected challenges related to charge histories, trap development and reservoir compartmentalization, which have limited cumulative production to date.

The aim of this study is to accurately describe and characterize the structural styles, deformation timing, and thrusting sequence in the southern Junggar fold-and-thrust belt. In addition, we will show how the complex geometric and kinematic evolution of individual fault-related folds impacted their petroleum prospectivity. To describe the subsurface geometry and kinematic evolution of these geologic structures, we use an extensive grid of 2-D seismic reflection profiles and two 3-D seismic volumes (Figure 3.2) – complemented by well data and surface geology – to interpret Jurassic-Quaternary aged faults and folds. We generate a series of balanced geologic cross-sections that describe several structural elements and constrain the history and timing of fold-and-thrust belt growth. In particular, we define the structural styles invoked in our subsurface interpretations using numerous structural geology methods (e.g. seismic data interpretations, kinematic forward models) and attempt to validate our structural interpretations using 2-D structural restoration methods. We subsequently present a model for how the southern Junggar fold-and-thrust belt developed since the Jurassic. Lastly, we illustrate

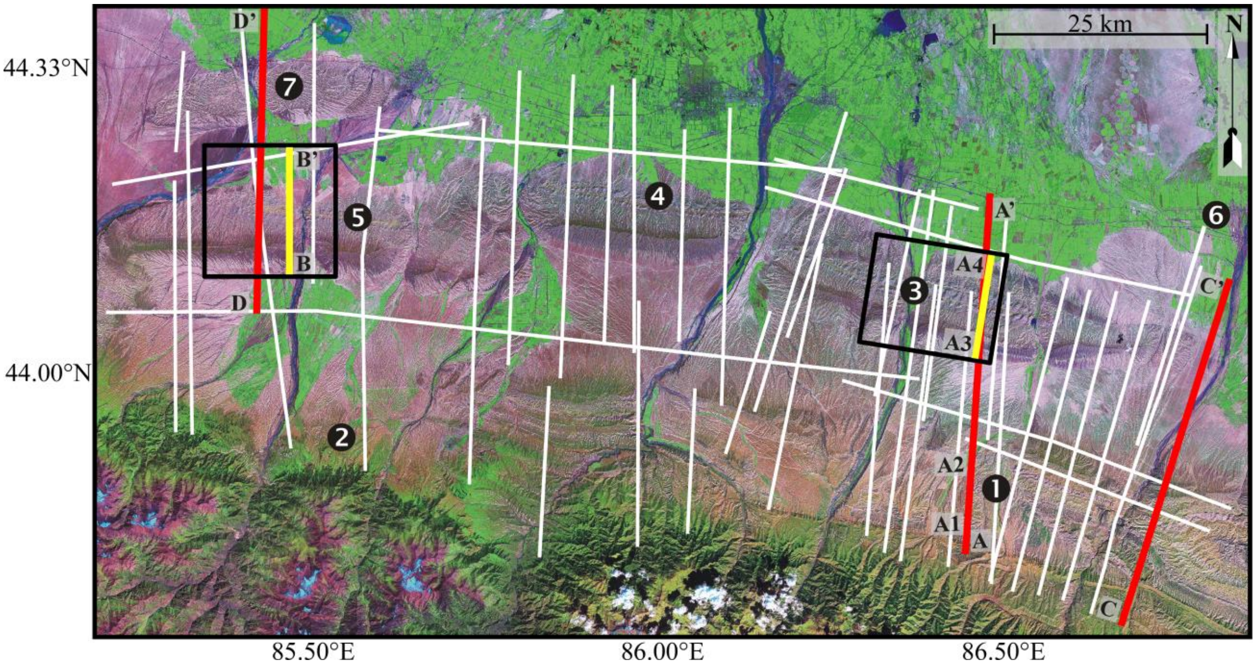

Figure 3.2: Seismic basemap in the southern Junggar basin of data available for this study. All seismic data were pre-stack depth migrated and depth converted using a velocity model derived from sonic logs, check-shot surveys and stacking velocities (e.g. Li et al., 2010). Red profiles are 2-D seismic sections shown in this study. Yellow lines are 2-D extracts from 3-D seismic volumes shown in this study. Numbers refer to anticlines, as described in Figure 3.1. False-color Landsat imagery displayed in bands 7-4-1 (R-G-B).

how the complex structural styles and sequence of deformation impacted hydrocarbon charge histories, trap formation and reservoir compartmentalization. Given the resurgence of exploration activities in other fold-and-thrust belts, including Kurdistan (e.g. English et al., 2015), Colombia (e.g. Mora, 2015) and southern Gulf of Mexico (e.g. Salomon-Mora et al., 2009), among others, our methods and results may provide insight into the structural styles and petroleum prospectivity in other complex fold-and-thrust belts.

Tectonic Setting

The Tian Shan is a ~2,000 km (~1,250 mi) long, east-west trending mountain belt in northwest China (Figure 3.1) that originally formed in the Paleozoic as the result of multiple collisional events involving continental blocks and island arcs during the closure of paleo-oceans (e.g. Windley et al., 1990; Allen et al., 1992; Gao et al., 1998). Subsequent uplift and shortening occurred by reactivating these early-formed structures in the Tian Shan region in the late Permian with deformation persisting until early Mesozoic times (e.g. Gao et al., 1998; Jolivet et al., 2010), during which the Junggar basin formed adjacent to the initial Tian Shan ranges. However, other studies suggest that this late Permian to early Triassic period is best characterized by sinistral shear, whereby Junggar formed originally as a transtensional basin (e.g. Allen et al., 1995). The subsequent Triassic-Jurassic tectonic environment is not well understood. Some studies suggest the region continued to undergo pulses of contraction and foreland basin formation (e.g. Hendrix et al., 1992). In contrast, others have found evidence more consistent with a period of tectonic quiescence and slow subsidence (e.g. Jolivet et al., 2010; Chen et al., 2011) or tectonic extension within the Junggar basin due to back-arc spreading (Li et al., 1998; Liu et al., 2000; Jia, 2012). This interpretation of Triassic and Jurassic extensional tectonics is consistent with the widespread early-middle Jurassic coal deposits in southern Junggar (Figure

3.3; e.g. Avouac et al., 1993; Jia 2012). More regionally, Jurassic-aged extension has been well-documented farther south in the Tarim basin (Sobel, 1999), and to the east in Mongolia and northern China (e.g. Graham et al., 2001; Ritts et al., 2001; Graham et al., 2012; Johnson et al., 2015).

In the late Jurassic to early Cretaceous, localized shortening and uplift occurred in southern and northern Tian Shan by re-activating pre-existing faults (e.g. Hendrix et al., 1992; Sobel, 1999; De Grave et al., 2007; Jolivet et al., 2010; Glorie et al., 2011). This late Mesozoic shortening in Tian Shan and southern Junggar was followed by an intense phase of Cenozoic shortening and uplift associated with the India - Eurasia collision (e.g. Tapponnier and Molnar, 1979; Burchfiel et al., 1999) and possibly the Arabia - Eurasia collision as well (Yin, 2010). Analysis of industry seismic reflection data, satellite imagery, and field observations indicate the primary Cenozoic tectonic motion in the Tian Shan has been north-south contraction, accommodated by thrust faulting and folding. Geologic, seismologic and geodetic observations suggest that this deformation style persists to the present day (e.g. Molnar and Tapponnier, 1975; Nelson et al., 1987; Avouac et al., 1993; Abdrakhmatov et al., 1996; Burchfiel et al., 1999; Thompson et al., 2002). The present-day Tian Shan ranges are bounded by the Tarim basin to the south and the Junggar basin to the north, the latter being the focus of our study (Figure 3.1).

The present-day southern Junggar fold-and-thrust belt contains up to ~6,000 m (~19,700 ft) of Cenozoic alluvial and shallow lacustrine clastic sediments that overlie fluvial and lacustrine deposits of late Cretaceous to Jurassic age (Figure 3.3; e.g. Avouac et al., 1993; Hendrix et al., 1995; Deng et al., 2000; Lu et al., 2010). The Quaternary section is locally up to ~3,000 m (~9,800 ft) thick, and thins abruptly over the crests of the Tugulu, Manas, and Huoerguosi anticlines and toward the Tian Shan rangefront to the south. Thus, the Quaternary section represents the most recent syntectonic (growth) section for the structures in this active fold-and-thrust belt (e.g. Charreau et al., 2008). Holocene shortening throughout the southern Junggar basin has uplifted and folded fluvial terraces across several anticlines, indicating continued shortening and growth to present-day (e.g. Avouac et al., 1993; Molnar et al., 1994; Deng, 2000; Poisson & Avouac, 2004).

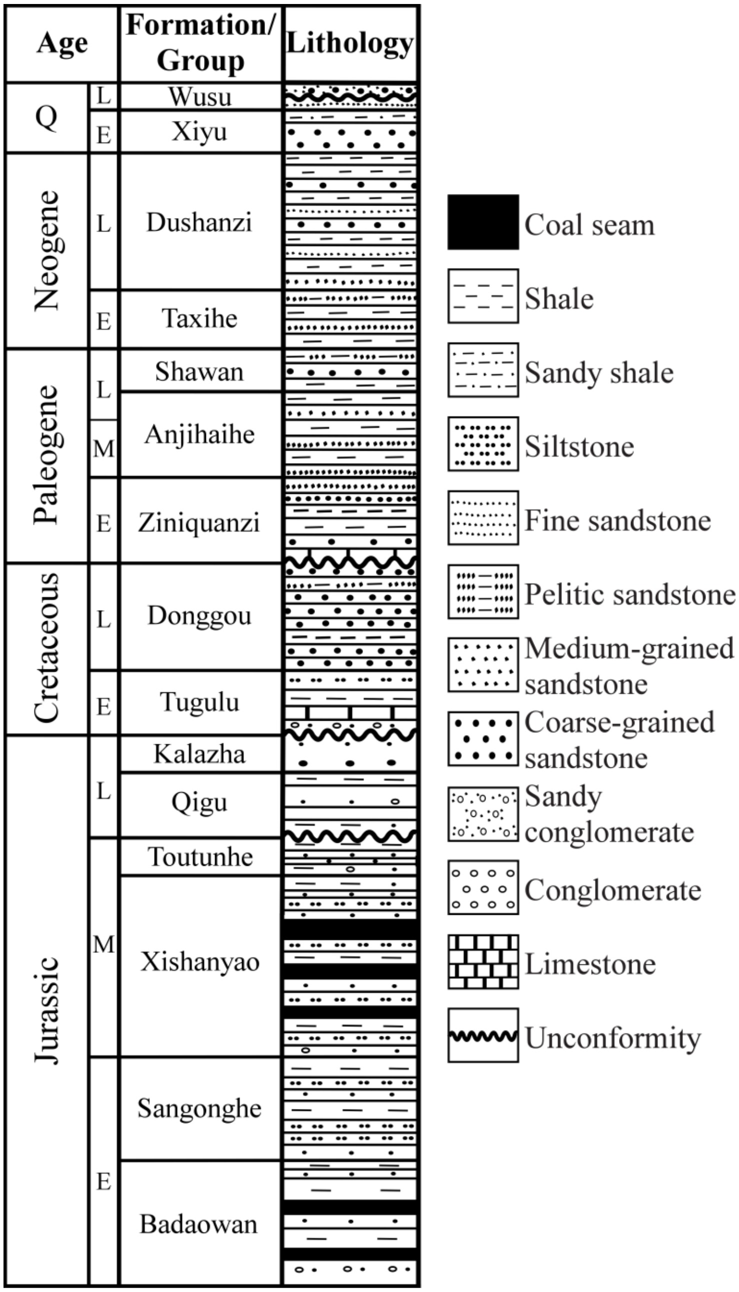

Figure 3.3: Stratigraphic column for the southern Junggar basin. Primary source rocks for the local petroleum system are Jurassic aged. Reservoir targets include clastic Cretaceous and Eocene intervals. Q = Quaternary. Modified from Yang et al. (2013); © 2012 Blackwell Publishing Ltd, European Association of Geoscientists & Engineers and International Association of Sedimentologists.

Regional Structural Characterization

As we described above, the southern Junggar fold-and-thrust belt is characterized by three east-west trending rows of structures: the southernmost Tian Shan rangefront; the middle row consisting of the Tugulu, Manas, and Huoerguosi folds; and the northernmost Hutubi-Anjihai-Dushanzi fold trend (Figure 3.1). All of these structures are well-imaged by 2- and 3-D seismic reflection data (Figure 3.2), which we use to interpret the subsurface fault and fold geometries across all three fold rows in the southern Junggar fold-and-thrust belt. These pre-stack depth-migrated data were converted to depth using a velocity model constrained by sonic logs, check-shot surveys and stacking velocities (e.g. Li et al., 2010). Constraints for the stratigraphy in our interpretations come from surface geology (e.g. Figure 3.1) and well picks. Cross-section A-A' (Figure 3.4) across the Qigu and Tugulu structures illustrates the common structural styles that characterize the first and second fold rows. These structures involve Jurassic through Holocene strata that are cut by a series of thrust ramps, which have been interpreted to sole into multiple detachment levels extend across the southern basin (Avouac et al., 1993, Deng et al., 2000, Li et al., 2010, Stockmeyer et al., 2014). The basal detachment is localized within or beneath the Jurassic section (e.g. Li et al., 2010). The middle Jurassic interval is known from outcrop and drill cores to contain numerous coal beds (Figure 3.3; e.g., Avouac et al., 1993; Hendrix et al., 1995; Yang et al., 2013). A diagnostic feature of these coal beds throughout our seismic dataset is a prominent set of bright seismic reflectors (e.g. Figure 3.4A). We rely on this prominent package of reflectors associated with middle Jurassic coal throughout this study to identify many of the structural elements to describe our subsurface interpretations.

In the Qigu region (e.g. Figure 3.4A) – beneath the northern Tian Shan rangefront – the lowermost detachments within the Mesozoic section are interpreted to underlie a large, north-

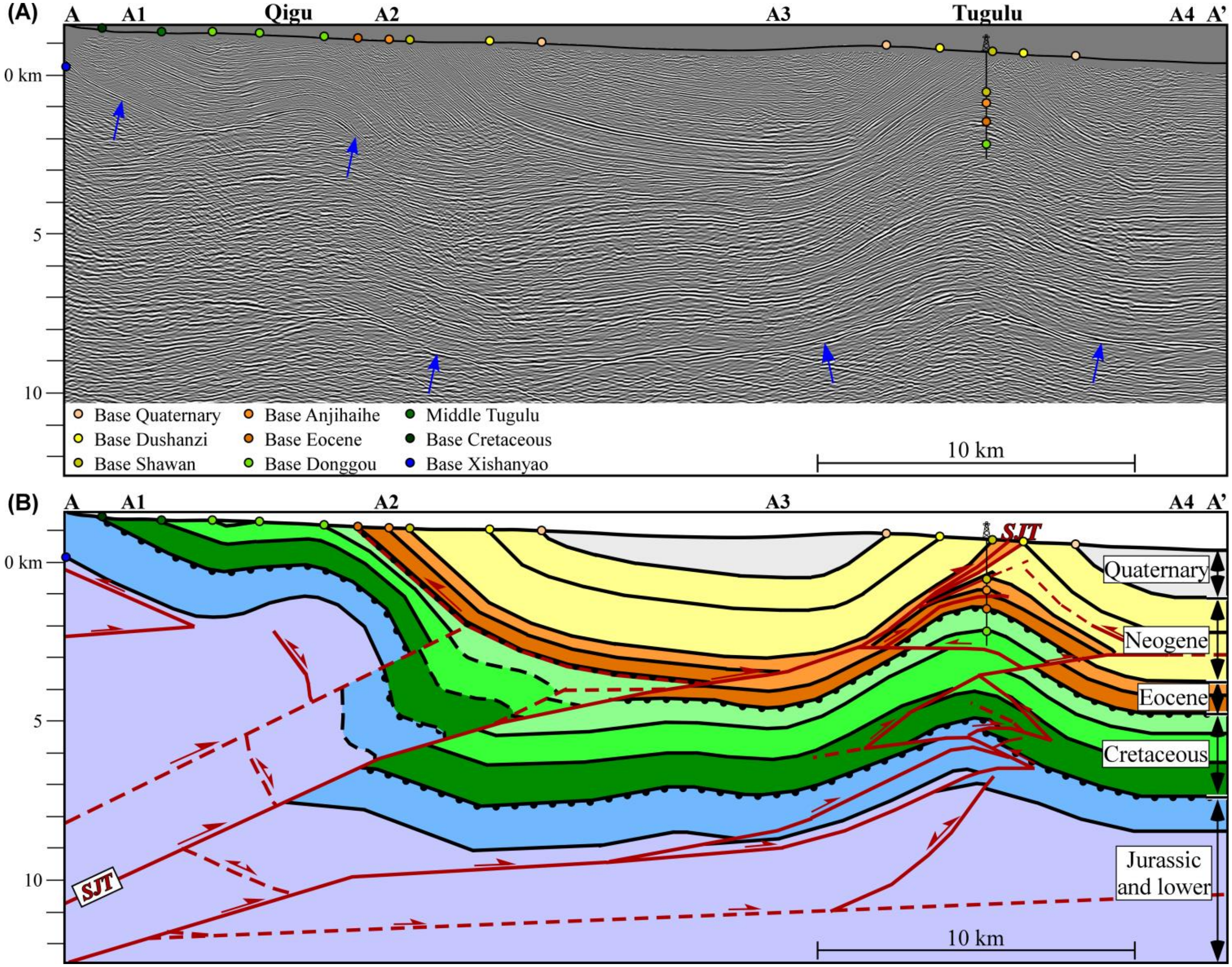

Figure 3.4: A) Uninterpreted 2-D seismic profile imaging the Qigu and Tugulu structures of section A-A'. Blue arrows point to coal-related Jurassic reflectors. Section location shown in Figures 3.1 and 3.2. Interpreted version shown in Appendix E. B) Geologic section of A-A' of the northern Tian Shan rangefront and Tugulu anticline. SJT is the Southern Junggar Thrust. See text for details.

dipping monocline (Li et al., 2010; Lu et al., 2010) exposing Mesozoic and Cenozoic (Figure 3.4, Chen et al., 2011). These Mesozoic detachments are generally interpreted to step down-to-the-south beneath the rangefront along a south-dipping ramp (e.g. Stockmeyer et al., 2014). The Tian Shan range front folds imaged in our seismic dataset, including the Qigu anticline (Figure 3.4A), are encompassed within this north-dipping monocline. We interpret that this monocline formed over a deep fault-bend that shallows in the lower-middle Jurassic stratigraphic level (Figure 3.4). This northward ramp-flat transition produces an anticlinal fault-bend fold (Suppe, 1983) that forms the north-dipping rangefront monocline. In the seismic section shown in Figure 3.4A, there is ~8,000 m (~26,200 ft) of structural relief over a horizontal distance of ~5,000 m (~16,400 ft) to the north. In order to accommodate this significant relief, we interpret two additional south-dipping thrust ramps offsetting the northern limb of the Qigu fold (Figure 3.4B).

The Qigu fold is uplifted by this monocline but has four-way closure, including a southern, south-dipping fold limb. When the Jurassic-Cretaceous strata present in the fold are corrected for the regional north-directed dip associated with the rangefront monocline, the Qigu structure exhibits a southern vergence. Thus, we interpret that the Qigu fold initially developed above a north-dipping reverse fault. We interpret that this north-dipping ramp reactivated a Mesozoic normal fault, which we discuss in a later section, and therefore pre-dated the formation of the large rangefront monocline. Thus, several south-dipping thrusts associated with the relief across the rangefront monocline are interpreted to offset this north-dipping ramp in our interpretation of Qigu (Figure 3.4B).

To the north, between the rangefront structures and the Tugulu-Manas-Huoerguosi fold row, we observe abrupt offset of prominent middle Jurassic coal reflectors and folding in the overlying strata (Figure 3.4A). To explain this, we interpret that Mesozoic detachments levels continue to the north from the rangefront and form thrusts ramps beneath the Tugulu, Manas, and Huoerguosi folds (Avouac et al., 1993; Deng et al., 1999; Lu et al., 2010). In our interpretation of Tugulu (Figure 3.4B) the folded Jurassic section has more than ~2,000 m (~6,600 ft) of structural relief across the anticline, indicating the presence of – at minimum – one deep-seated detachment level in the early Jurassic or older stratigraphic interval. However, the precise depth of the basal detachment level that is responsible for uplift and folding of Jurassic rocks in this section is below the depth resolved by the seismic reflection data (Figure 3.4A).

Within the core of the Tugulu, Manas, and Huoerguosi structures, structural relief of the Cretaceous-Quaternary stratigraphy within the folds typically increases upward (e.g. Figure 3.4). Throughout our seismic dataset, this upward increase in structural relief coincides with abrupt increases in seismic reflector dip. These abrupt dip changes are present in the forelimbs of these folds within the Cretaceous section and again in the backlimbs at shallower depths. We interpret these abrupt dip changes are produced by thrust ramps (e.g. Shaw et al., 2005) that link to detachments in the upper Mesozoic or Cenozoic intervals. These thrust ramps dip to the south and north beneath the backlimbs and forelimbs of the fold, respectively. This pattern of faulting and associated folding is characteristic of a structural wedge deformation style (Medwedeff, 1992; Shaw et al., 2005; Mount et al., 2011), which we discuss in more detail in a subsequent section.

One of the most prominent structural features at shallow levels within the Tugulu-Manas-Huoerguosi fold trend is a series of south-dipping thrust fault splays, which outcrop along the northern flank of these anticlines (Figure 3.1). This fault system is the tectonically active Southern Junggar Thrust (SJT; Stockmeyer et al., 2014). The upper segments of the SJT rise as en echelon fault ramps from a single intermediate detachment level, mimicking the surface expression of the Tugulu-Manas-Huoerguosi fold trend (Figure 3.1). This intermediate detachment level sits near the base of the upper Eocene Anjihai Formation, a weak siltstone and mudstone section (Stockmeyer et al., 2014). Much like our interpretations of deeper Mesozoic detachment levels, this SJT Eocene detachment has been interpreted in detail to step down-to-the-south as a thrust ramp beneath the northern Tian Shan rangefront (Stockmeyer et al., 2014). This is one of the thrust ramps that produces the pronounced structural relief across the Tian Shan rangefront monocline (Figure 3.4).

In summary, the northern Tian Shan rangefront structures are best described as monoclonal folds above a deep-seated Mesozoic anticlinal fault bend. This – and potentially other – Mesozoic detachments continue to the north where south-dipping, potentially imbricated, thrust ramps cut into the Tugulu-Manas-Huoerguosi fold trend. These structures are complicated further by the presence of backthrusts and shallower detachment levels, forming structural wedges. In addition, the active SJT steps up-to-the north from depth below the rangefront, uplifting and offsetting the rangefront monoclines. The SJT cuts through the entire Mesozoic section and soles to a ~horizontal Eocene detachment before ramping up-to-the-north again as en echelon thrust ramps that are surface-emergent in the forelimbs of the Tugulu-Manas-Huoerguosi fold row (Figure 3.4).

The preceding discussion of section A-A’ (Figure 3.4) describes the first-order characteristics and structural styles across the southern Junggar fold-and-thrust belt. However, even this general discussion illustrates the thrust belt’s complex structural history. Our regional interpretation indicates multiple phases of deformation, evidenced by offset and truncated structural elements. Moreover, the number of detachment levels and thrust ramps, as well as the sequence of thrusting within the Tugulu-Manas-Huoerguosi fold trend suggests a complex structural evolution that impacts hydrocarbon charge, trap formation, and continuity of clastic reservoirs. In the following sections, we discuss detailed aspects of our interpretations that offer insights into how the southern Junggar fold-and-thrust belt and its petroleum system evolved.

Structural Styles in the Southern Junggar Fold-and-Thrust Belt

Fault and fold characteristics

The Tugulu, Manas, and Huoerguosi structures all represent distinct, doubly plunging folds with local structural culminations (Figure 3.1). However, these three folds share several common structural characteristics observable in seismic reflection data, which we document in Figure 3.5. The first of these common features is the backlimbs of folds are cut by splays of the south-dipping SJT. A clear example of these footwall cutoffs is imaged and annotated in section B-B' (Figure 3.5). These upper splays of the SJT sole to an Eocene detachment at ~4,000 m (~13,100 ft) depth (e.g. Figure 3.4B; Stockmeyer et al., 2014). These ramp-flat geometries along the upper SJT produce synclinal fault-bend folds (e.g. Suppe, 1983) where the synclinal axial surfaces define the southern limit of this fold row (Stockmeyer et al., 2014). At several locations along strike, there are multiple splays of the SJT present above the anticlines in its footwall (e.g. Figure 3.4B). These uppermost splays are generally planar ramps parallel to stratigraphic beds in the hanging wall. In addition, these SJT splays dip to the south more steeply than the backlimbs of the folds in the footwall of the SJT (e.g. Figure 3.4A, 3.5). Thus, the upper SJT splays do not appear to be folded by – and likely post-date – the development of the underlying anticlines (e.g. Avouac et al., 1993; Charreau et al., 2008; Lu et al., 2010).

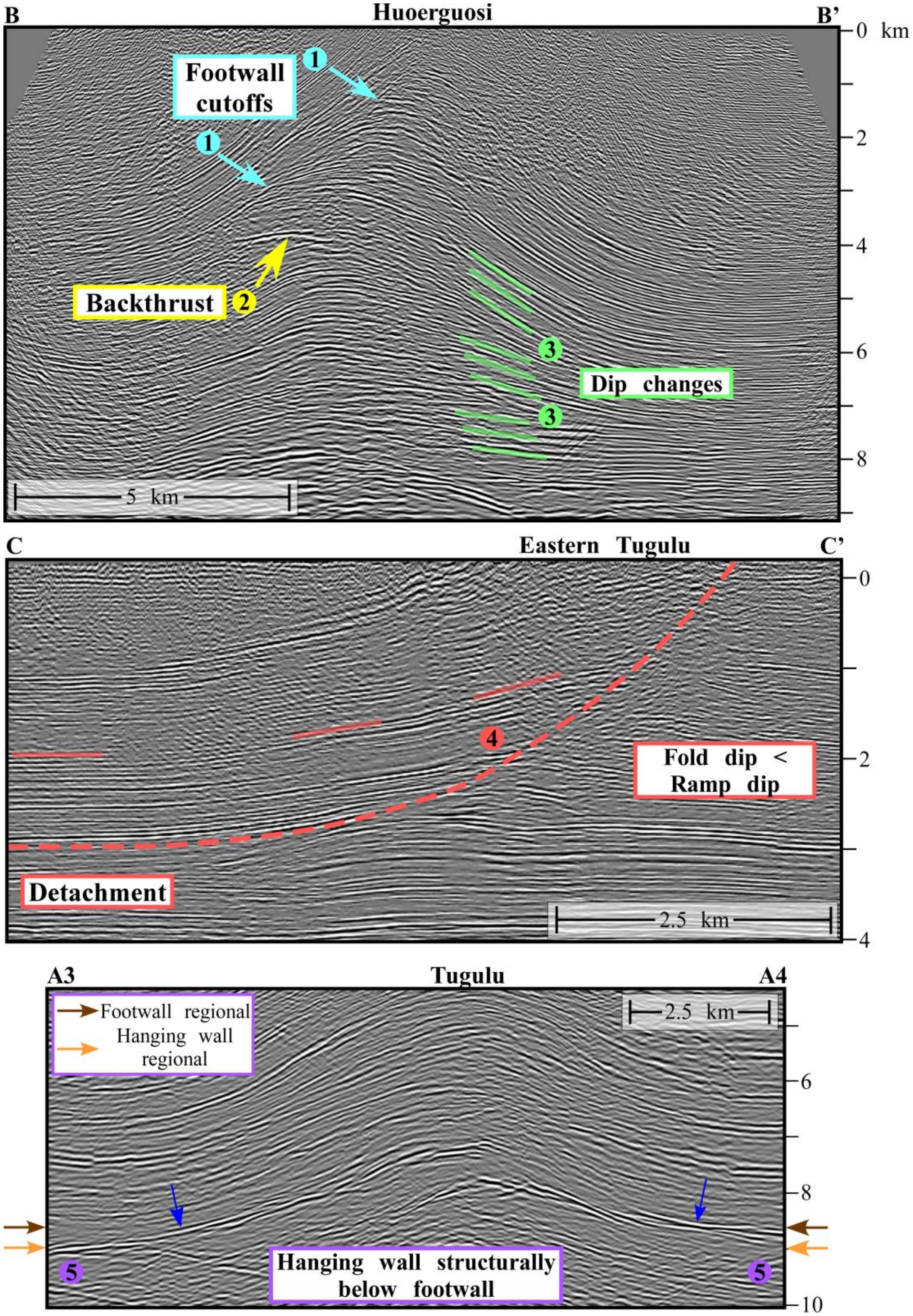

Figure 3.5: Common structural observations in the available seismic data. Top: Section B-B' extracted from the Huoerguosi 3-D: 1) footwall cutoffs; 2) fault plane reflections; and 3) abrupt changes in bed dip. Middle: Section C-C' across the Tugulu fold. Seismic reflectors dip less than the underlying thrust ramp (4), consistent with shear fault bend folding (Suppe et al., 2004). Bottom: Section A3-A4 from A-A'. Abrupt changes in regional level of mid-Jurassic reflectors (5). See text for details. Blue arrows point to coal-related Jurassic reflectors. Section locations shown in Figures 1 and 2.

A second structural component shared by the Tugulu, Manas, and Huoerguosi structures is that the anticlines beneath the SJT have abrupt, upward increases in fold limb dip (Figure 3.5, B-B’). These folds are generally symmetric with northern and southern limbs that extend downward below ~8,000 m (~26,200 ft) below sea level (Figure 3.5). Bed dips in these limbs are steep (~45°) at shallow depths but dip more gently (~10°) in the deeper section of the fold. However, these dip changes are not gradual but rather occur principally as discrete steps (Figure 3.5, B-B’). These abrupt dip changes reflect the presence of thrust faults and/or detachments within the anticlines (e.g. Shaw et al., 2005). Several of these thrust faults are additionally constrained in the seismic data by hanging wall and footwall cutoffs, as well as local fault plane reflections, a third common feature in this fold trend (Figure 3.5, B-B’). Although there are several south-dipping thrusts in the cores of the Tugulu, Manas, and Huoerguosi structures, many of the prominent thrust ramps are north-dipping backthrusts, which cause many of the abrupt dip changes observed in the forelimbs of folds. The presence of forethrusts and backthrusts – in addition to cutoffs and abrupt bed dip changes in forelimb folds – are the primary observations for invoking a structural wedge interpretation style (Medwedeff, 1992; Shaw et al., 2005, Mount et al., 2011) to describe the of the Tugulu-Manas-Huoerguosi fold trend.

In many locations across the study area we observe fault ramps stepping up from several detachment levels. However, in much of our seismic dataset, such as section C-C’ (Figure 3.5), hanging wall folds dip significantly less than the underlying thrust ramp, a fourth common element of the Tugulu-Manas-Huoerguosi fold trend. This observation of fold dip less than ramp dip after stepping up from a detachment – where these dips are equal – is consistent with a shear fault-bend folding structural style (Suppe et al., 2004; Hardy & Connors, 2006). We observe this in several of the thrust sheets across southern Junggar including the uppermost ramps of the SJT (e.g. Figure 3.5) and above deeper thrust ramps, particularly many of the backthrusts within our structural wedges.

We document a fifth observation shared by the Tugulu, Manas, and Huoerguosi structures in section A3-A4 (Figure 3.5), involving the nature of structural relief across these folds. Jurassic horizons in these folds – easily identified by the bright reflectors associated with mid-Jurassic coal seams – are structurally low at the hanging wall regional level relative to the regional level in the footwall. The coal reflectors in section A3-A4 (Figure 3.5) are ~500 m (~1,600 ft) lower in the syncline on the southern side of the Tugulu fold trend relative to their structural position north of the fold. This change in structural level occurs abruptly across the fold. In contrast, the overlying Cretaceous and Eocene strata are typically higher or at the same structural level on the south side of the fold relative to the north (e.g. Figure 3.6A). Thus, this change in structural relief must be accommodated by northward thinning of the upper Jurassic section across the fold trend (e.g. Figure 3.4).

We have described five common observations in the Tugulu-Manas-Huoerguosi structural trend: 1) footwall cutoffs along the SJT, 2) abrupt upward increases in seismic reflector dip, 3) backthrust fault plane reflections, 4) hanging wall folds dipping less than fault ramp dips after stepping up from a detachment, and 5) Jurassic structural levels jumping abruptly across these folds (Figure 3.5). In the following sections, we discuss how these observations are incorporated into our detailed structural interpretations of the southern Junggar fold-and-thrust belt history.

The role of Jurassic rift systems

As discussed above, Jurassic units in southern Junggar are typically at a lower structural position on the south side of the Tugulu, Manas, and Huoerguosi folds than to the north (Figure

3.5). In addition, we observe these Jurassic horizons are generally horizontal outside of the fold trend. Thus, this change in elevation occurs abruptly across the folds and cannot be attributed to regional processes such as loading-induced flexure of the upper crust or changes in accommodation space. A detailed analysis of the deep structure of the Tugulu anticline in 3D seismic data (Figure 3.2) allows us to explore an alternative interpretation for the observed structural relief of Jurassic strata.

Prominent reflections within the mid-upper Jurassic sequence – particularly the bright coal-related seismic reflectors – exhibit clear lateral terminations in the core of the Tugulu fold, which indicate fault cutoffs. Aligning these cutoffs at depth within the lower Mesozoic section yields fault dips of ~45-55° S (Figure 3.6A). Moreover, the lower Jurassic and older section thickens abruptly northward in the hanging wall of the most prominent of these faults. This expanded section is expressed by a set of prominent reflections within the Jurassic section that dip to the north, whereas the mid-Jurassic coal horizon is flat or south dipping (Figure 3.6A). While the footwall geometries are not well imaged, the upper Jurassic section appears to thin abruptly to the north by ~300 m (~1,000 ft) across the fault into the footwall (Figure 3.6A). Taken together, the structural relief, steep fault dip, and thickened Jurassic hanging wall section suggest that the structure beneath the Tugulu fold represents a south-dipping listric normal fault that was active in the Jurassic. To explain the sense of structural relief observed in the mid-Jurassic interval (e.g. Figure 3.6A), this normal fault must trend roughly east-west, dip to the south, and locally accommodate up to ~1,000 m (~3,300 ft) of normal separation.

The north-dipping lower Jurassic seismic reflectors guiding our synrift interpretation (Figure 3.6A) are well imaged throughout both 3-D seismic volumes and in several of the 2-D profiles across the study area (Figure 3.2). Thus, we interpret this synrift interval to be regionally

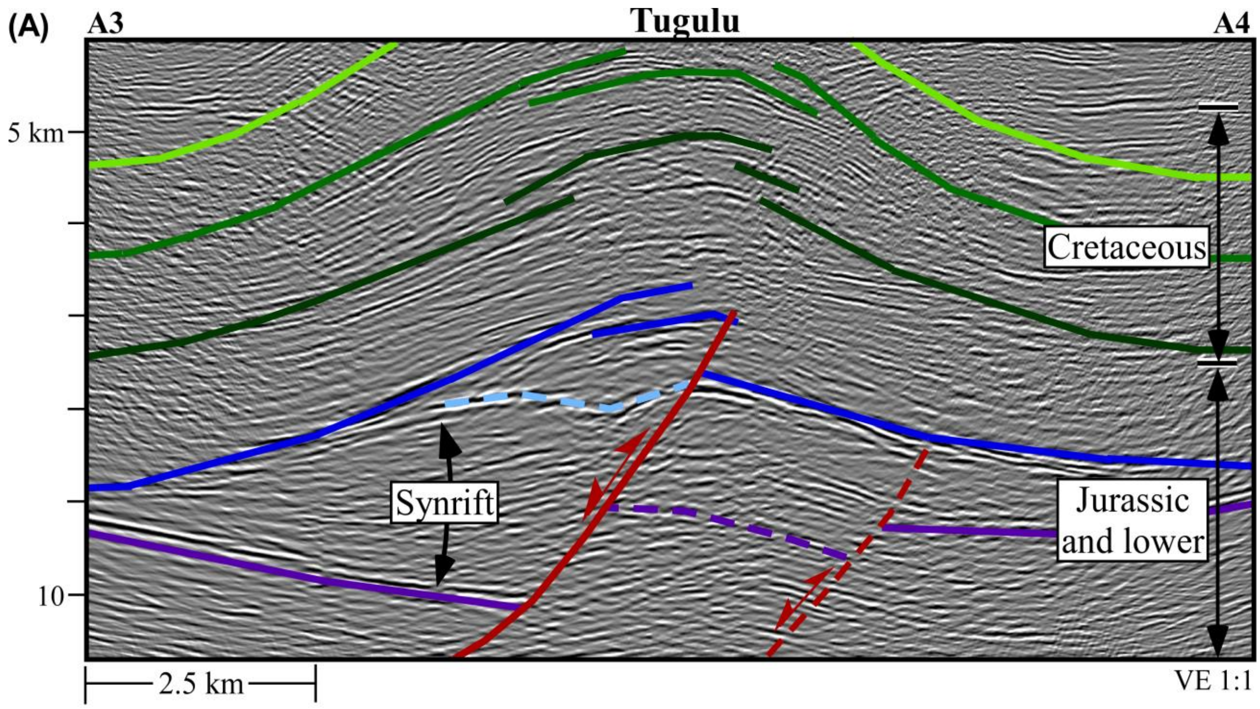

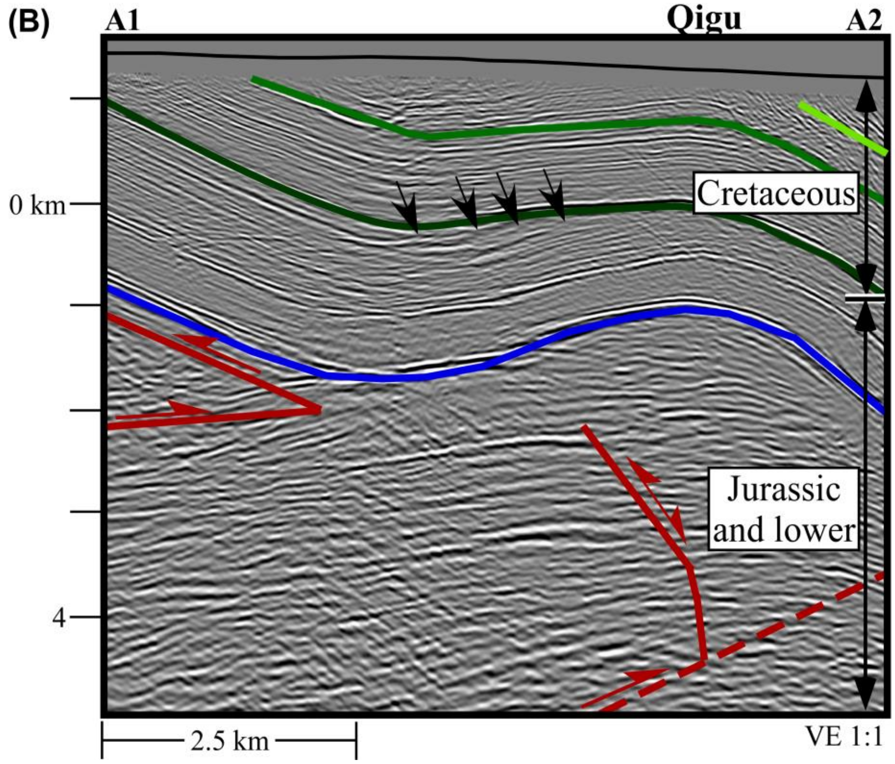

Figure 3.6: Interpretations of inverted rift structures in southern Junggar. A) Seismic section A3–A4 from the Tugulu 3-D seismic volume (Figure 2). This shows evidence for Jurassic half grabens in the hanging walls of south-dipping normal faults that were subsequently inverted. See text for details. B) Section A1–A2 from A-A' (Figure 4) across the Qigu fold. Black arrows indicate Jurassic reflectors truncated by the regional, base-Cretaceous angular unconformity. We interpret this angular unconformity reflects a period of early contractional deformation in the late Jurassic to early Cretaceous, which was subsequently eroded then reactivated throughout the Cretaceous. See text for details.

extensive across southern Junggar. These wedge shaped packages of Jurassic strata in the hanging walls of the high-angle faults are consistent with the geometry of rollover structures that are common in extensional systems (e.g., Hamblin, 1965; Gibbs, 1984; McClay and Ellis, 1987;

Groshong et al., 1990; Xiao and Suppe, 1992; Shaw et al., 1997). This interpretation is consistent with previous field observations of rapid changes in thickness of coal beds and other Jurassic strata (e.g. Avouac et al., 1993). In addition, Jurassic normal faults have been interpreted in seismic reflection data across northern Tian Shan rangefront structures to the west of our immediate study area (Xu et al., 1992). Jurassic-aged rift systems have been identified throughout Mongolia and western and northern China as well. These are generally interpreted as the product of back-arc spreading, transtensional tectonics or perhaps extensional collapse (e.g. Li et al., 1998; Sobel, 1999; Liu et al., 2000; Graham et al., 2001; Ritts et al., 2001; Graham et al., 2012; Jia, 2012; Johnson et al., 2015).

Despite our interpretation of a Jurassic rift system below the Tugulu-Manas-Huoerguosi fold trend, there is clear evidence of reverse separation of the prominent mid-Jurassic coal-related seismic reflectors across the uppermost portion of the interpreted Jurassic normal fault (Figure 3.6A). The change in sense of slip along the fault beneath Tugulu suggests that this structure has undergone positive tectonic inversion. Inverted normal fault systems are common in many tectonic environments, and are generally characterized by uplifted half grabens in the hanging walls of normal faults with contractional folding localized above the fault tips (e.g., Glennie and Boegner, 1981; Bally, 1984; Williams et al., 1989; McClay and Buchanan, 1992; Rivero et al., 2011). The steep dips (45°-55°) of several active thrust sheets throughout the Tian Shan ranges are interpreted to represent pre-existing normal faults that have been inverted to accommodate regional tectonic shortening in the region (Sibson & Xie, 1998). Thus, tectonic inversion may be a common structural style throughout the greater Tian Shan region.

To explain the structural observations beneath the Tugulu fold, this inversion must have occurred after deposition of the mid-Jurassic coal horizon and may have involved more than one fault splay (e.g. Figure 3.6A). Similar patterns of structural relief, faulting and folding that are suggestive of rifting and structural inversion are present beneath the Manas and Huoerguosi folds. However, the stacking of thrust sheets and related folding above these deep Mesozoic structures makes it difficult to resolve their precise geometries in the available seismic reflection data. Thus, we are unable to identify a discrete syntectonic sedimentary section or unconformity, if present, that would constrain the timing of tectonic inversion in this fold row. In an attempt to establish the timing of tectonic inversion we examined the Qigu anticline, which lies to the south of the Tugulu fold within the Tian Shan rangefront (Figure 3.6B). The Jurassic-Cretaceous section within the Qigu anticline is much shallower than at Tugulu (e.g. Figure 3.6A) and can be directly tied to outcrop, providing a more coherent representation of fold geometries than the corresponding strata at Tugulu.

As discussed previously, the Qigu anticline is a south vergent structure that formed above a north dipping reverse fault. Within the southern limb of this fold, the upper Jurassic section locally dips more steeply than the overlying Cretaceous section, which leads to a dramatic southward thickening of the upper Jurassic section across the Qigu anticline. This dip change occurs across a regional, angular unconformity at the base of the Cretaceous sequence that we observed in seismic data (e.g. Figure 3.6B) and in the field, suggesting Qigu underwent a phase of contractional folding in the late Jurassic to early Cretaceous, after which the fold was peneplained. A similar transition from Jurassic rifting to late Jurassic or early Cretaceous contractional folding has been documented in the southern Tian Shan (Sobel, 1999). This positive inversion may have been a consequence of the Cimmerian orogeny, a major convergent event in western China, which has been interpreted to activate pre-existing structures in the Tian Shan during the late Mesozoic (e.g. Hendrix et al., 1992; De Grave et al., 2007). Continued thrust reactivation on this north-dipping fault at Qigu in the Cretaceous generated additional uplift of the fold – indicated by the thinning of Cretaceous intervals across the northern limb of the fold (Figure 3.4) – and produced the prominent, four-way fold closure that provides a structural trap for the Qigu oil field (Fan et al. 2012). The local evidence of earliest Cretaceous shortening here at Qigu, as well as regionally across the Tian Shan (e.g. Sobel, 1999; De Grave et al., 2007), suggests the possibility that the normal faults beneath the Tugulu, Manas, and Huoerguosi folds were also tectonically inverted at this time. Alternatively, or in addition, these structures may have been inverted in the Cenozoic associated with intense convergence throughout western Asia. In either case, inversion beneath Tugulu would explain the thrust sense of fault offset at shallow levels along the high-angle Jurassic normal fault (Figure 3.6A).

As shown in section A-A' near the base of the Tugulu fold (Figure 3.4), Jurassic normal faults sole into a deep Mesozoic detachment not imaged in our seismic dataset. Thus, our subsurface interpretations indicate at least two prominent Mesozoic detachments across the southern Junggar fold-and-thrust belt. Interestingly, the presence of these inverted rift structures is spatially coincident with the en echelon style of the Tugulu-Manas-Huoerguosi fold trend (Figure 3.1, 3.2). Indeed, our analysis throughout southern Junggar suggests the locations of these Mesozoic extensional structures appear to have localized thrust ramps in the overlying detachment systems that propagated northward into the foreland during the Cenozoic (e.g. McClay and Buchanan, 1992). Therefore, the Jurassic rift architecture may have controlled the spatial occurrence of folds throughout the southern Junggar basin. Moreover, due to normal faulting and subsequent reverse faulting through Jurassic source rocks (Clayton et al., 1997; Ding et al., 2003), our interpretations imply the potential for early hydrocarbon charge into

Mesozoic traps, similar to migration histories for the central Junggar basin to the north (Xiang, et al., 2015).

As we suggest above, the thrust ramps stepping up above the rift structures from a mid-Mesozoic detachment produce imbricate stacks of thrust sheets that characterize the fold trends to the north of the Tian Shan rangefront in the southern Junggar fold-and-thrust belt. These folds also exhibit evidence for the presence of numerous backthrusts and additional forethrusts at shallower depths through the cores of these structures. Thus, we turn our focus in the next section to the details of our interpretation for a structural style dominated by imbrication and structural wedging within the southern Junggar thrust belt.

Imbricated structural wedges

Deformation within the Tugulu, Manas, and Huoerguosi folds is accommodated on a series of stacked detachments that extend northward from the Tian Shan rangefront. As discussed above, the lowermost of these detachments likely sits within or below the lower Jurassic section, loosely constrained based on the geometry of the synrift package and the inverted normal fault geometry (Figure 3.4, 3.6A). Thrust ramps and folds imaged in the seismic data suggest there are additional detachment levels within the middle to upper Mesozoic section (e.g. Figure 3.4). Finally, the SJT, which lies in the hanging wall of these structures, is linked to a detachment within the Eocene Anjihai Formation (Figure 3.4; Stockmeyer et al. 2014). The presence of multiple detachment levels and stacked thrust ramps within the Tugulu-Manas-Huoerguosi fold trend reflects the process of structural imbrication (e.g. Shaw et al., 1999). This yields abrupt increases in fold limb dips moving from the deep to the shallow portions of these folds (e.g. Figure 3.5). These sudden changes in dip occur across shallower detachment levels or thrust ramps. Several of these thrust ramps are imaged within the folds, including a prominent set of north-dipping backthrusts defined either by direct fault plane reflections (Figure 3.5) or downward terminating fold limbs and cutoffs within the Cretaceous and Cenozoic strata. The presence of these backthrusts suggests that a component of slip on these detachments is accommodated by structural wedging.

A structural wedge forms by the coeval activity of forethrusts and backthrusts that are linked at a wedge tip (Medwedeff, 1992; Shaw et al., 2005). The Huoerguosi 3-D seismic volume provides a well-constrained example of a structural wedge within this trend (Figure 3.5, B-B'). Strata above a well-imaged backthrust dip much more steeply than those in the immediate footwall. In Figure 3.7, we present a kinematic model that describes the behavior of this structural wedge. In stage A, a subtle anticline that pre-dates activity on the incipient structural wedge – perhaps by structural inversion of a Jurassic-aged normal fault – has developed. In stage B, a deep detachment level forms a ramp above the pre-existing structure. This fault ramp

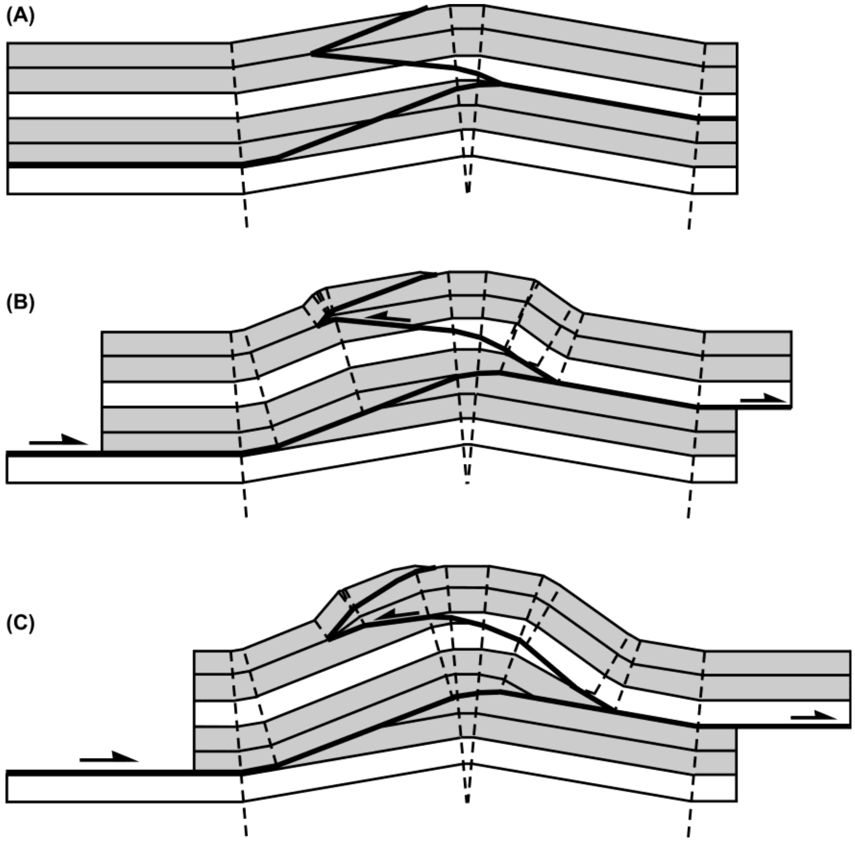

Figure 3.7: Kinematic model describing the sequential development of the southern Junggar structural wedges. A) a pre-existing anticline showing the trace of the incipient wedge structure (bold). B) growth of the structural wedge via coeval activity of forethrusts and backthrusts. The wedge tip translates along the upper detachment of the forethrust. Slip on the ramp at depth is partitioned between motion on the wedge backthrust and slip along the upper detachment. C) Increased slip widens the structural wedge and increases structural relief. Note the backthrust ramp stepping up from a mid-crustal detachment at the base of the shallower, white horizon and cutting up through this white layer. This reflects shear fault-bend folding invoked in the kinematic model (Suppe et al., 2004). See text for details.

shallows its dip as it extends across the underlying anticline because it is linked to an upper detachment level within the northern limb of the pre-existing fold. Stage B involves coeval slip on a backthrust that is linked to this upper detachment level, forming a wedge tip pinned to a synclinal axial surface. As slip increases on the fault system, the wedge tip translates toward the foreland along the upper detachment level. The axial surface pinned to this wedge tip is active; strata are folded across this axial surface and incorporated into fold limb above the backthrust. All or part of the slip on the forethrust can be translated to the backthrust by this process. In cases where all of the slip is not transferred to the backthrust, displacement can be sent farther into the foreland along an upper detachment (Mount et al., 2011). Model stages B and C invoke this process, where coeval slip continues on the forethrust and backthrust, with a component of forethrust slip bypassing the backthrust and continuing into the foreland along the upper detachment. In section B-B' (Figure 3.5), the position of the backthrust within the Huoerguosi anticline corresponds to an abrupt change in dip within the northern limb of the fold, with strata dipping ~30°N above and ~10°N below the fault. In addition, we observe the dip of the backthrust to be steeper than that of the beds in its hanging wall, despite stepping up from a detachment (e.g. Figure 3.5, C-C'). This suggests a shear fault-bend fold structural style (Suppe et al., 2004; Hardy & Connors, 2006). We observe similar relationships of backthrust dip exceeding bed dip within the Tugulu and Manas structures as well. Thus, we invoke this structural style in our kinematic model (Figure 3.7) and throughout our structural wedge interpretations.

Guided by this structural interpretation and those discussed above (e.g. Figure 3.5, 3.6), we generated a balanced geologic cross-section (Dahlstrom, 1969) of the Huoerguosi and Anjihai structures (D-D') based on a regional 2-D seismic profile that images both anticlines

(Figure 3.2). Section D-D’ (Figure 3.8) highlights all of the major tectonic elements of the Huoerguosi trend that we have described previously, including evidence for a Jurassic rift system, a backthrust within a structural wedge, and the surface-emergent SJT fault ramp. Our interpretation of the structure includes a south-dipping listric normal fault that offsets the Jurassic section and is inverted to fold a broad, gentle anticline in the overlaying Cretaceous section. Additionally, a detachment level within the Jurassic section steps up as a south-dipping thrust ramp above this fold. This ramp flattens to an upper detachment level in the mid-Cretaceous section and is linked to two north-dipping backthrusts that forms an imbricated structural wedge, akin to our forward model in Figure 3.7. The shallower of these two backthrusts shows evidence of shear fault-bend folding; strata in its hanging wall fold dip less than the thrust ramp despite stepping up from a detachment (Suppe et al., 2004; Hardy & Connors, 2006). Thus, the Huoerguosi wedge structure interpreted in D-D’ is best described as an imbricated shear fault-bend fold structural wedge (e.g. Guzofski et al., 2007). Within the Huoerguosi fold, we interpret a series of additional forethrust and backthrust splays with smaller displacements based on the geometries of the 2-D seismic reflectors and constrained by analysis of the 3-D seismic data volume. Collectively, these faults reflect a complex history of thrusting and fault-related folding that has thickened the core of the Huoerguosi fold. Section D-D’ also documents the geometry of the active SJT, which rises from an upper Eocene detachment level and consists of two fault splays at the surface (Stockmeyer et al., 2014). Similar to our kinematic model in Figure 3.7, the aggregate slip on the backthrusts of the Huoerguosi wedge structure is less than the slip on the underlying wedge forethrust. We suggest the forethrust slip is partitioned between displacement on the wedge backthrusts and slip extending northward on the mid-Cretaceous detachment (Mount et al., 2011). The Anjihai anticline – an active oil field to the

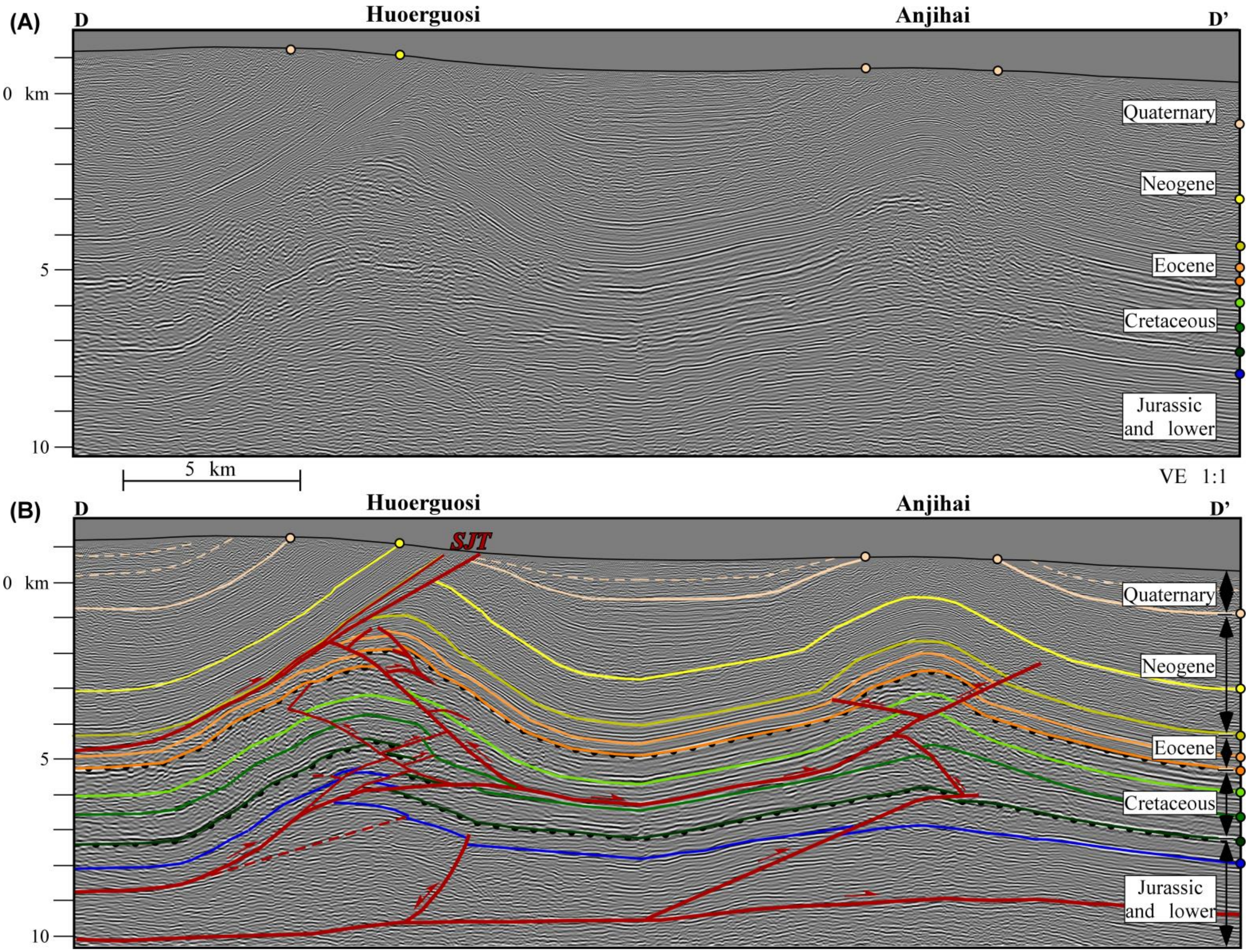

Figure 3.8: A) Uninterpreted 2-D seismic section D-D' across the Huoerguosi and Anjihai anticlines. B) Interpretation of D-D'. See text for details. Stratigraphy is constrained by surface geology, well data and our regional seismic interpretations. Section locations shown in Figures 3.1 and 3.2.

north of Huoerguosi (Figure 3.1) – may consume any slip that bypasses the Huoerguosi fold on the mid-Cretaceous detachment, or perhaps on a deeper Mesozoic detachment.

The Anjihai structure in section D-D’ (Figure 3.8) exhibits several characteristics that suggest it is a detachment or fault-tip fold (e.g., Poblet et al., 1997; Shaw et al., 2005; Daëron et al., 2007). Specifically, the generally symmetric fold is formed above a detachment level within the Jurassic section. This surface dips gently to the south and represents the basal detachment level that was inferred in our interpretations of the rift structures beneath the Tugulu, Manas, and Huoerguosi folds (Figure 3.4, 3.8). In addition, the Cretaceous section is thickened in the core of the Anjihai fold, consistent with a detachment folding mechanism (Figure 3.8). However, in contrast to previous interpretations of this structure (e.g. Daëron et al., 2007), the seismic data used in this study images clear evidence of fault ramps stepping up into the core of the Anjihai fold. Most notably, there is an abrupt increase in backlimb dip at ~5300 m depth, which we interpret to be caused by a thrust ramp (Figure 3.8). The presence and location of this thrust ramp within the Anjihai structure is further constrained by hanging wall and footwall cutoffs. When combined with our stratigraphic interpretations, this south-dipping fault ramp is observed to sole to a detachment level at the same stratigraphic level as the mid-Cretaceous detachment interpreted immediately north of the Huoerguosi structure (Figure 3.8B). This implies there is a continuous detachment level between the two structures that could accommodate slip bypassing the Huoerguosi wedge backthrusts (e.g. Figure 3.7) and be consumed within the Cretaceous-Eocene section of the Anjihai fold. In addition, a deeper thrust ramp is inferred due to the presence of Jurassic coal horizon cutoffs present in section D-D’ and several 2-D seismic reflection profiles along strike. We interpret that this deep ramp steps up from the basal detachment within the lower Jurassic section, and has modest displacement (<200m). Forelimb dip changes and cutoffs observed within the core of the Anjihai structure also imply the presence of a prominent backthrust that links to the deeper forethrust, consistent with the structural wedge interpretation across the Tugulu-Manas-Huoerguosi fold trend. We observe additional offset evidence that indicates this backthrust was offset by the shallower forethrust ramp. These forethrusts and the backthrust we have interpreted each modified the initial detachment fold geometry.

Structural restorations and their implications

In an attempt to validate our structural interpretation in section D-D' (Figure 3.9A), we generated a palinspastic restoration of section D-D' that conserves bed length (Figure 3.9B). As the Anjihai anticline is the northernmost structure in the southern Junggar fold belt, we suggest that shortening of the Anjihai fold must consume all of the displacement on the detachments and faults within it, including the mid-Cretaceous detachment level that extends north from the Huoerguosi fold. Thus, the foreland of section D-D' serves as an effective pin line for the restoration. The restored loose line for the Cretaceous-Eocene section in Figure 3.9B implies a component of foreland directed simple shear. Moreover, the restored fault shapes are consistent with typical ramp-flat geometries. This palinspastic restoration of D-D' yields ~5,000 m (~16,400 ft) of horizontal shortening in the upper Jurassic section. Notably, this restoration produces ~650 m (~2,100 ft) less shortening in the lower Cretaceous than the upper Jurassic (Figure 3.9B).

We consider two possible explanations for the geometry of the restored loose line and the shortening discrepancy. We first consider these patterns could be the result of changes in bed length during deformation, a phenomenon that invalidates palinspastic restoration assumptions and has been suggested to occur in other fold-and-thrust belts (e.g. Epard & Groshong, 1993;

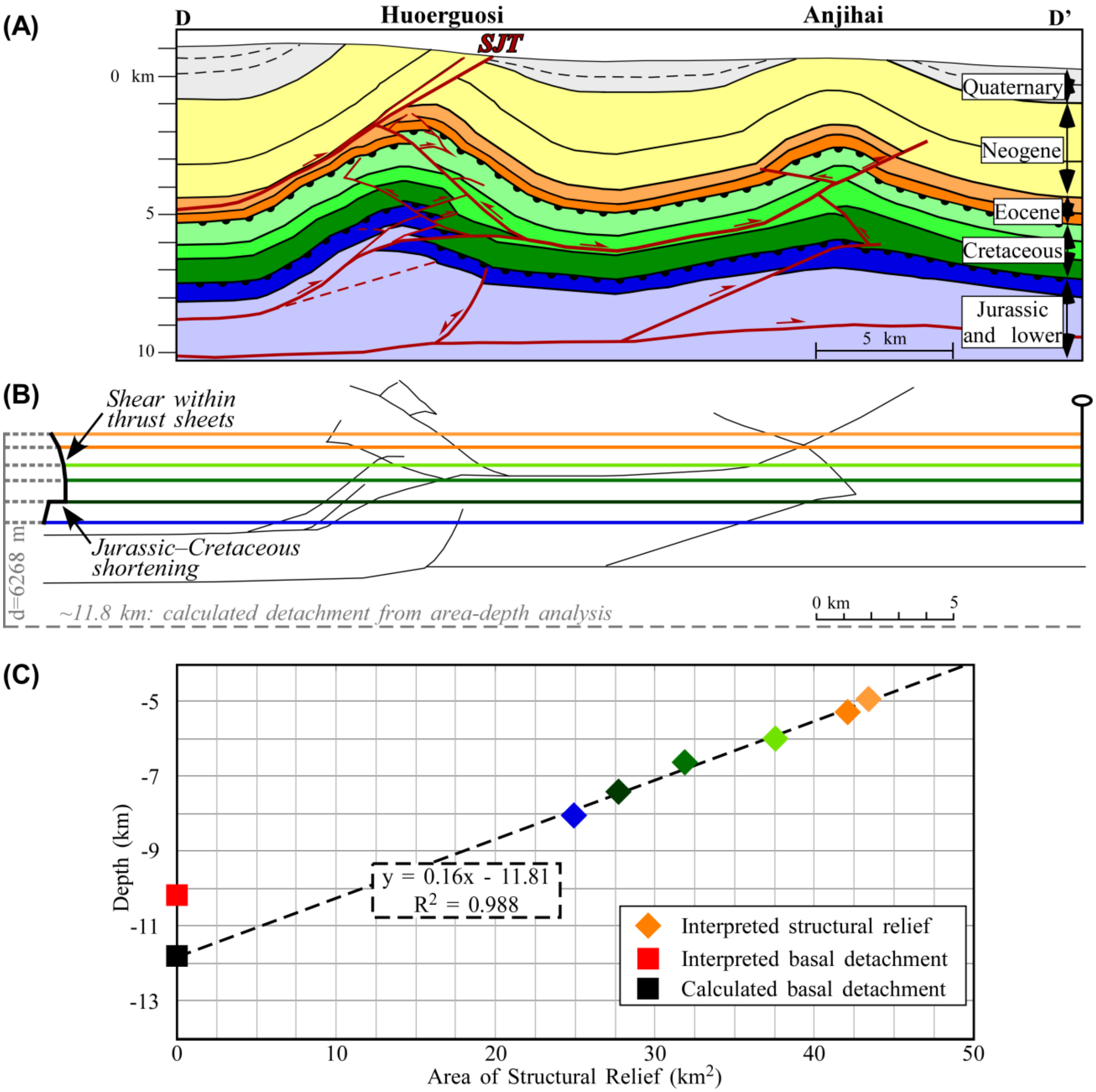

Figure 3.9: A) Geologic section D-D' based on the interpretation in Figure 3.8. B) Palinspastic restoration of section D-D' reveals a ~650 m (~2,100 ft) offset between the upper Jurassic and lower Cretaceous sections. The tilt in the restored loose line indicates hanging wall shear during deformation in the Cretaceous-Eocene interval. See text for details. Area-depth result (grey) suggests slightly more shortening. See original area-depth plot in Appendix E. C) Area-depth plot using the structural relief data implied by our interpretation. See text for details.

Gonzalez-Mieres & Suppe, 2006; Groshong et al., 2012; Schlische et al., 2014; Eichelberger et al., 2015; Groshong, 2015). To assess this possibility, we modeled the magnitude of shortening and depth of the basal detachment using the area-depth method (Epard & Groshong, 1993).

Area-depth does not adhere to a specific kinematic theory, nor does it assume constant line-length during deformation. In addition, the area-depth method assumes a constant boundary condition displacement for all pre-growth strata while allowing an additional component of shortening – manifest as hanging wall simple shear – that increases linearly from the basal detachment to the top of the pre-growth section (Epard & Groshong et al., 1993; Gonzalez-Mieres & Suppe, 2006). Using the areas of structural relief of our structural interpretation (Figure 3), the area-depth method calculates a constant shortening magnitude, d, of 6,268 m (~20,600 ft) for the mid-Jurassic-Eocene section (Figure 3.9B, 3.9C). In addition, the basal detachment is calculated to be ~11,800 m (~38,700 ft) below sea level, ~1,600 m (~5,200 ft) deeper than the interpreted basal detachment depth underlying the Huoerguosi structure in Section D-D' (Figure 3.9B). The linear best-fit function used to calculate shortening and detachment depth yields an R^2 value of 0.988 (Figure 3.9C), indicative of a balanced structural interpretation, consistent with the results of the palinspastic restoration (Figure 3.9B).

In the area-depth interpretation, the shortening discrepancies produced by the palinspastic restoration (Figure 3.9B) would be caused by layer-parallel shear (LPS) during deformation (Appendix E), and would not have tectonic significance (e.g., Groshong et al., 2012). In this interpretation, the goodness of fit between the linear area-depth function (Figure 3.9C) and the interpreted structural relief suggests the Jurassic-Eocene interval is entirely pre-growth and that little to no hanging wall shear has been manifest above the basal detachment. Thus, uplift of the Jurassic-Eocene stratigraphic interval and structural growth in the Huoerguosi and Anjihai structures would not have initiated until the late Eocene or later. Moreover, the area-depth model suggests all of the fault slip in the section is consumed within the Huoerguosi and Anjihai structures, consistent with our structural interpretation. The calculated basal detachment

(~11,800 m; ~38,700 ft) is deeper than our seismic interpretation (~10,200 m; ~33,500 ft). A detachment below that in our interpretation of D-D’ (Figure 3.8) may explain the modest folding of our interpreted detachment beneath the Anjihai fold (Figure 3.8B). Alternatively, this apparent folding could be the result of a modest velocity pull-up feature.

The second possibility we consider is that the loose line and shortening discrepancy between the Cretaceous and Jurassic sections derived from the palinspastic restoration have direct tectonic significance. In this interpretation, the ~650 m (~2,100 ft) difference in shortening between the upper Jurassic and lower Cretaceous intervals (Figure 3.9B) could record positive tectonic inversion of the Jurassic normal fault and related contractional folding beneath the Huoerguosi anticline during the late Jurassic to early Cretaceous. This latter interpretation is consistent with the observed fold geometries and interpreted rift systems beneath the Tugulu, Manas, and Huoerguosi trends (Figure 3.6A) well as folding of the Qigu anticline in this same time period, recorded by the angular unconformity documented in Figure 3.6B. Moreover, the tilt in the restored loose line of the palinspastic restoration in the Cretaceous-Eocene interval could reflect foreland directed simple shear. This shear is consistent with our interpretations of these structures as shear fault-bend folds developed above several distinct detachment levels (Suppe et al., 2004). We favor this latter interpretation because it is consistent with our interpretations of structural style, timing of structural growth in the Qigu anticline, and the presence of multiple detachments in the section.

Regardless of the restoration approach, our structural interpretations of D-D’ (Figure 3.9) suggest that growth of the Huoerguosi and Anjihai folds was structurally linked by common detachment levels and was – at least in part – contemporaneous. In particular, a portion of the slip along the Huoerguosi forethrust bypasses the wedge backthrusts along a mid-Cretaceous detachment and is consumed within the core of the Anjihai fold (Figure 3.8, 3.9). The Hutubi anticline, a subsurface fold with no surface expression, is present along-strike to the east of the Anjihai structure and northeast of the Tugulu fold (Figure 3.1). However, no major folds have developed along this trend between the eastern edges of the Huoerguosi and Tugulu anticlines. This suggests that the intervening Manas and Tugulu folds likely accommodate all or most of the slip on their detachments and faults, likely by structural wedging (e.g. Figure 3.4).

Structural timing and thrusting sequence

The presence of multiple detachments and faulting levels in the southern Junggar fold-and-thrust belt raises important questions about the deformation sequence within the Tugulu, Manas, and Huoerguosi structures. In this type of imbricate system, the sequence of thrusting can have an important influence on the geometry of structures and the development of hydrocarbon traps (e.g., Shaw et al., 1999). Moreover, thrusting sequence can influence the maturation of hydrocarbons and development of charge pathways. Figure 3.10 provides an illustrative description of the structural evolution of the southern Junggar fold-and-thrust belt based on the tectonic elements that we have described in the preceding sections. In this process, we consider the presence of angular unconformities, patterns of syntectonic growth strata (e.g. Suppe et al., 1992; Shaw and Suppe, 1994) and evidence of late Quaternary fault activity that constrain the timing of several thrust faults and related folds.

In Figure 3.10A, we interpret that southern Junggar basin was originally deformed by a rift system with a series of Jurassic normal faults along portions of the rangefront and beneath the future locations of the Tugulu, Manas, and Huoerguosi structures. Expansion of the Jurassic section in the hanging wall of steeply dipping faults and the greater depth of the top Jurassic horizon on the south relative to the north side of the trend across the folds are the primary

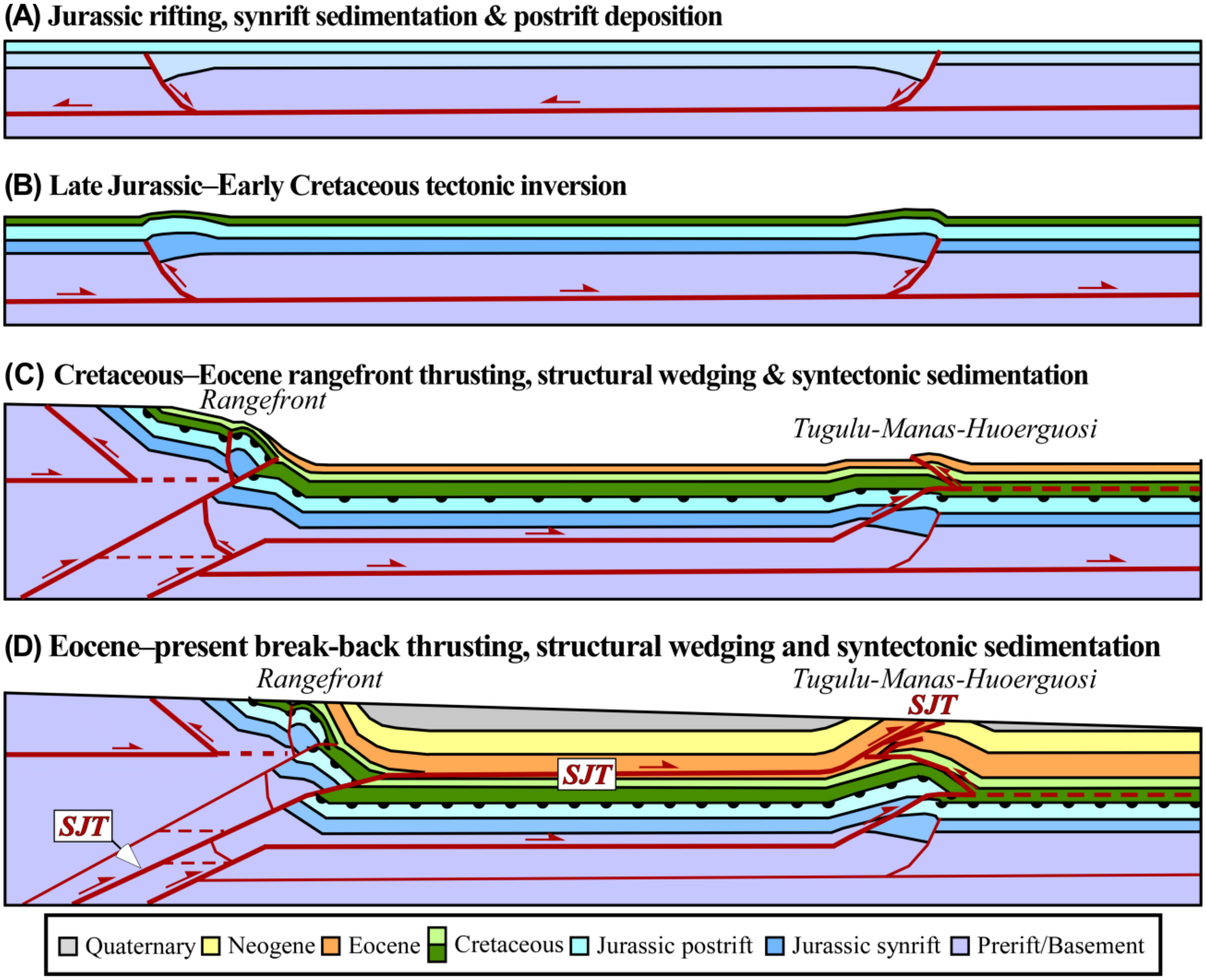

Figure 3.10: Development of the major structural elements in the Tian Shan rangefront and Huoerguosi, Manas, and Tugulu folds. A) Jurassic rifting and synrift deposition. B) Late Jurassic to earliest Cretaceous tectonic inversion of the rift basins. C) Cretaceous-Eocene shortening – including fault-bend folding and structural wedging – along the northern Tian Shan rangefront and the Tugulu-Manas-Huoerguosi fold row. Fault slip that is not consumed by the wedge structures would likely be consumed on structures farther to the foreland, such as the Anjihai anticline (e.g. Figure 3.8). D) Eocene–present shortening includes further development of the structural wedges followed by the formation and displacement along the out-of-sequence Southern Junggar Thrust (SJT). The SJT is active at present, folding and uplifting Holocene fluvial terraces (e.g. Avouac et al., 1993).

observations that support the interpretation of these rift systems (Figure 3.5, 3.6). The next phase of deformation involved tectonic inversion of all or portions of these rift structures (Figure 3.10B). The primary evidence for tectonic inversion at this time is found at the Qigu anticline, which shows folded Jurassic strata overlain by an angular unconformity and more modestly folded Cretaceous strata (Figure 3.6B). This fold appears to be contractional in nature and is interpreted to reflect structural inversion of the pre-existing normal fault. The angular unconformity indicates these structures were peneplained, after which Cretaceous strata were deposited. The dramatic thinning of Cretaceous stratigraphy along the northern limb of the Qigu anticline (Figure 3.6B) is evidence these strata were deposited as a syntectonic growth interval during continued development of the rangefront structures. We interpret a similar inversion history for portions of the rift system beneath the Tugulu, Manas, and Huoerguosi structures. This interpretation is based on the uplift and local reverse separation of the top Jurassic horizon along the high-angle normal faults (Figure 3.6A, 3.8).

Upper Cretaceous strata in our cross-sections show no appreciable thickness changes across the Tugulu, Manas, and Huoerguosi structures (Figure 3.4, 3.8). In contrast, lower Eocene strata show evidence of subtle thinning onto the southern limb of Tugulu and Huoerguosi (Figure 3.4, 3.8). This could indicate the Eocene interval is a section of growth strata. The presence of detachments and thrust ramps related to the SJT as well as faulting within the structural wedges complicates these stratigraphic intervals. Thus, it is possible that thinning of Eocene beds may be structural rather than stratigraphic in origin. However, if the thinning is depositional, it suggests that a component of contractional folding on Mesozoic detachments may have occurred in the Eocene (e.g. Daëron et al., 2007; Lu et al., 2010) and produced the early forms of our interpreted imbricated shear fault-bend fold structural wedges (Figure 3.10C). The Neogene section also appears to show modest thinning onto the crests of the Tugulu, Manas, and Huoerguosi structures (Figure 3.4, 3.8). Thus, we leave open the possibility of limited fold growth and fault activity of the Mesozoic detachments and structural wedges into the Neogene (Figure 3.10D). If true, this would imply a long period of activity on the Mesozoic detachments within the southern Junggar basin (Daëron et al., 2007; Lu et al., 2010). Alternatively, this modest thinning of the Neogene section might reflect uncertainties in the velocity model used for depth conversion, and thus not represent a significant structural element. In any case, it appears that the primary phase of Cenozoic contraction occurred in the Eocene, followed by a period of modest structural growth or tectonic quiescence in the Neogene (Figure 3.10D).

The Quaternary section thins abruptly onto portions of the Tugulu, Manas, and Huoerguosi structures and the Tian Shan rangefront, implying that it records a second, major phase of Cenozoic deformation (e.g. Fu et al., 2003; Charreau et al., 2008; Lu et al., 2010). Notably, the fanning of limb dips within the Quaternary sections along the northern limb of the Tugulu, Manas, and Huoerguosi structures is consistent with the detachment (Poblet et al., 1997) and shear fault-bend folding mechanism (Suppe et al., 2004) implemented in our cross-sections (Figure 3.4, 3.8). Thus, we interpret the detachment levels within the Jurassic and Cretaceous sections transferred slip northward from the rangefront during the Quaternary, leading to the continued growth of the wedge structures that form the core of the Tugulu, Manas, and Huoerguosi folds. We suggest that these wedge structures were originally localized by the presence of the underlying, tectonically inverted Jurassic rifts systems. The final stage of deformation is related to the activity and development of the SJT (Figure 3.10D). This fault offsets and folds Holocene terraces across the Tugulu-Manas-Huoerguosi fold trend and is considered the source of the 1906 M 7.4-8.2 Manas earthquake (Avouac et al., 1993; Molnar et al., 1994; Burchfiel et al., 1999). Moreover, the upper splays of the SJT are planar ramps that do not appear to be folded by the underlying anticlines within the Tugulu, Manas, and Huoerguosi structures (Figure 3.4, 3.8). This geometry, combined with the evidence of recent fault activity, implies that the SJT is a young, break-back thrust system with uppermost splays that post-date most, if not all, of the growth of the Tugulu, Manas, and Huoerguosi anticlines (Charreau et al., 2008; Lu et al., 2010). In this scenario, the detachment level in the Eocene section propagated northward from the rangefront and extended up the southern limb of the Tugulu, Manas, and Huoerguosi folds, forming the upper SJT fault ramps (Stockmeyer et al., 2014).

In sum, the complex tectonic sequence across the southern Junggar fold-and-thrust belt involves components of rifting, tectonic inversion, imbrication, structural wedging, and break-backward thrusting. In the following section we explore the implications of these structural elements for development operations and future exploration in the basin.

Implications for reservoir geometry and hydrocarbon charge

While the surface expression of the Tugulu, Manas, and Huoerguosi anticlines are suggestive of simple, doubly plunging folds that might provide large closures (Figure 3.1), the complex structural elements and sequence of deformation that we have described yield a complex petroleum trap history. Specifically, the presence of multiple detachment levels, along with coeval forethrusts and backthrusts within the wedge structures, has produced a series of complexly faulted closures within Eocene reservoir sequences. Several forethrusts and backthrusts – mapped in depth slices from 3-D seismic volumes (Figure 3.11) – may have limited the extent of fold closures, which would imply that prospective reservoir compartments may rely on fault seal. Moreover, given that these faults have different orientations, magnitudes of slip, and possibly ages, it seems likely that they may have different sealing characteristics. As an example, three wells that penetrate an Eocene reservoir target along the crest of the Huoerguosi fold encountered different fluid types, oil-water contacts and reservoir pressures (Figure 3.12). These include water saturated intervals above oil bearing pay zones and heavy oil over gas, all within the same reservoir sequence. Based on detailed horizon, fault and fluid contact mapping in 3-D seismic data across the Huoerguosi structure, we show that these three wells each penetrated distinct fault-bounded compartments of the same Eocene reservoir target

(Figure 3.12). Our finding of a compartmentalized reservoir target integrated with the information of varying fluid types and fluid contact depths from the three wells (Figure 3.12) indicate that the faults bounding each block have had sufficient sealing capacity to prohibit pressure communication. Thus, recognition and detailed mapping of the various forethrust and backthrust splays is necessary to properly characterize the prospectivity of different reservoir compartments, as well as to evaluate the overall recoverable reserves in this field.

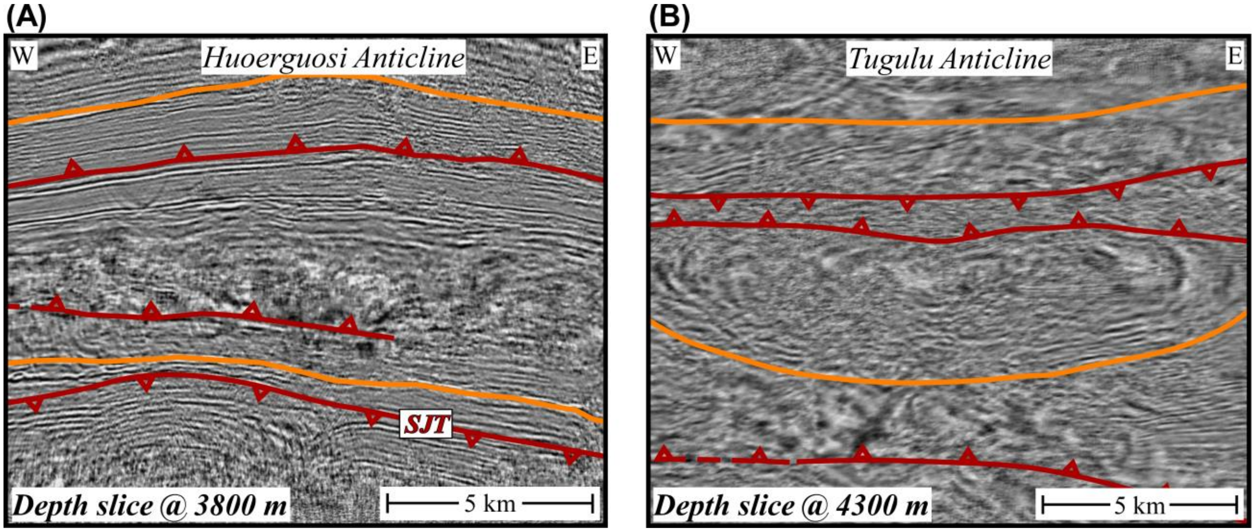

Figure 3.11: Depth slices from 3-D seismic volumes in southern Junggar (Figure 3.2). *Left*: Depth slice across the Huoerguosi anticline at 3,800 m (~12,500 ft) below sea level. *Right*: Depth slice across the Tugulu anticline at 4,100 m (~13,500 ft) below sea level. These data both reveal the presence of a fold in the core of each structure that is cut by north- and south-dipping thrust faults, shown in red. Orange horizon is the base-Eocene regional unconformity. SJT is Southern Junggar Thrust. 3-D seismic volumes were pre-stack depth migrated and depth converted using a velocity model derived from sonic logs, check-shot surveys and stacking velocities (e.g. Li et al., 2010). Stratigraphy is constrained by surface geology, well data and our regional seismic interpretations.

The complex sequence of deformation in the Tugulu, Manas, and Huoerguosi structures may also have an influence on the formation of hydrocarbon charge pathways into these reservoirs. Specifically, we speculate that the presence of Jurassic rift systems may provide charge pathways for additional hydrocarbon volumes beneath portions of these fold trends. Early stages of contractional fold growth, due to tectonic inversion and thrusting in the late Mesozoic or early Cenozoic, may have formed initial structural traps within these fold trends (e.g. Figure 3.10B). These initial structures could have accumulated hydrocarbons that migrated early in the basin's history. The Qigu oil field along the rangefront of the Tian Shan may serve as such an example, given evidence for its early formation (Figure 3.6B) and proven reserves (Figure 3.1). Subsequent thrusting and folding in the Cenozoic would have dissected and complicated the geometries of any early-formed traps, including those within the Tugulu, Manas, and Huoerguosi

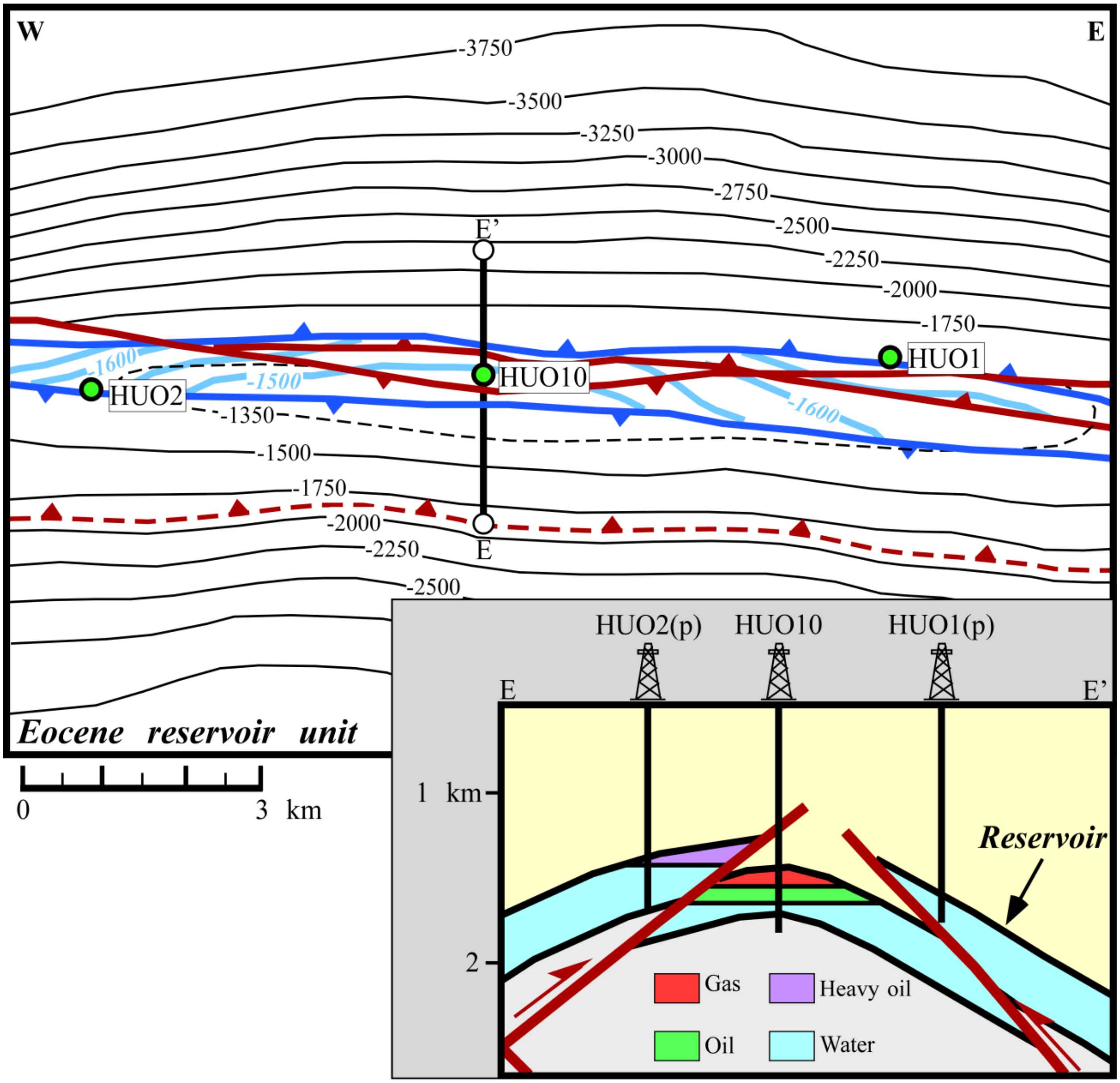

Figure 3.12: Structure contour map of an Eocene reservoir unit across a portion of the Huoerguosi 3-D seismic volume (Figure 3.2) and schematic cross-section E-E' detailing three distinct reservoir blocks penetrated by three different wells. See text for details. Black contours correspond to the hanging wall reservoir compartments (e.g. north and south of the thrust faults). Light blue contours correspond to the footwall compartment bounded by both faults. Hanging wall fault contacts shown in red. Footwall fault contacts shown in blue. Projected wells in E-E' indicated by (p). Stratigraphy is constrained by surface geology, well data and our regional seismic interpretations.

structures (e.g. Figure 3.10C, 3.10D). This suggests the possibility that hydrocarbons may have, in part, re-migrated from early traps within the Mesozoic section into the present-day fold and fault closures within the Cenozoic section. All of these complicated tectonic elements likely limit the volumes of hydrocarbons trapped in shallow Eocene reservoir horizons within Tugulu, Manas, and Huoerguosi structures (Figure 3.12). However, they also offer the potential for exploration in deeper traps within these folds, as well as in other, early-formed structures across the fold belt.

Conclusions

We have presented new interpretations of high-quality 2- and 3-D seismic reflection data characterizing the structural styles across the southern Junggar fold-and-thrust belt in the northern foreland basin of the Tian Shan ranges, NW China. The results of our detailed subsurface interpretations and restorations have important implications for how this fold-and-thrust belt formed, in addition to the impact of structural style on petroleum prospectivity in the basin. Our primary results have shown:

1) The southern Junggar basin likely originated as a Jurassic rift system as evidenced by high angle normal faults, hanging wall fold geometries characteristic of rollover structures, and abrupt jumps in regional position of Jurassic strata, consistent with extension.
2) Rift structures underwent positive tectonic inversion, as evidenced by normal and reverse separation along high angle faults. Tectonic inversion and related shortening appears to have occurred in the late Jurassic to early Cretaceous, indicated by the Qigu angular unconformity.

3) Tectonic inversion of these normal faults in the late Mesozoic to early Cenozoic formed traps that may have accumulated hydrocarbons during an early stage of charge from Jurassic or older source rocks.
4) Contractional deformation dominated the Cenozoic period and led to the development of the complex fault-related folds farther to the north in the southern Junggar basin. These structures are characterized as imbricated shear fault-bend fold structural wedges.
5) Our detailed mapping of a reservoir target in the Huoerguosi 3D seismic volume confirms a highly compartmentalized Eocene reservoir, a product of the numerous forethrusts and backthrusts associated with the structural wedge style of trap formation. These small thrusts act has effective seals, limiting cross-fault communication.
6) Late Quaternary deformation has been localized along the Southern Junggar Thrust (SJT), which acts an active, out-of-sequence thrust sheet, truncating the backlimbs of the Tugulu-Manas-Huoerguosi fold trend. Thus, the southern Junggar basin is currently in a sequence of break-back thrusting.

CHAPTER 4

Geomechanical restoration as a tool for fractured reservoir characterization: application to the Permian Basin, West Texas[4]

Introduction

Effective tools for fracture characterization are in great demand for development operations in conventional and unconventional petroleum basins around the world. In deformed basins, understanding the influence of tectonic strain on reservoir properties influencing permeability is particularly important. Indeed, structural elements may aid hydrocarbon production by generating or enhancing secondary permeability within the target reservoir (e.g., Lorenz & Finley, 1989; Engelder et al., 2009; Ghosh & Mitra, 2009; Gale et al., 2014). Tectonic strain may also enable vertical or lateral communication with adjacent formations, impacting reservoir performance. In the presence of stacked reservoirs, this may increase ultimate recoveries during field development. However, reservoir connectivity can also divert hydrocarbons to less economic zones (e.g., Aydin, 2000; Bowker, 2007). Similarly, faults or fracture networks can facilitate water incursion, leading to higher water cuts and, ultimately, decreasing well profitability. Thus, accurate characterization of natural structures that impact reservoir performance is critically important during field development (e.g., Hennings et al., 2000). Indeed, accurate predictions of strain patterns in fractured reservoirs may prove to be quite valuable during development operations, informing such decisions as well placement, borehole orientation, perf intervals, and production management. However, secondary fault and

---

[4] A version of this chapter was submitted for publication in *AAPG Bulletin* in 2016

fracture patterns at the reservoir scale are often complex and difficult to constrain due to the resolution limits of conventional seismic reflection data.

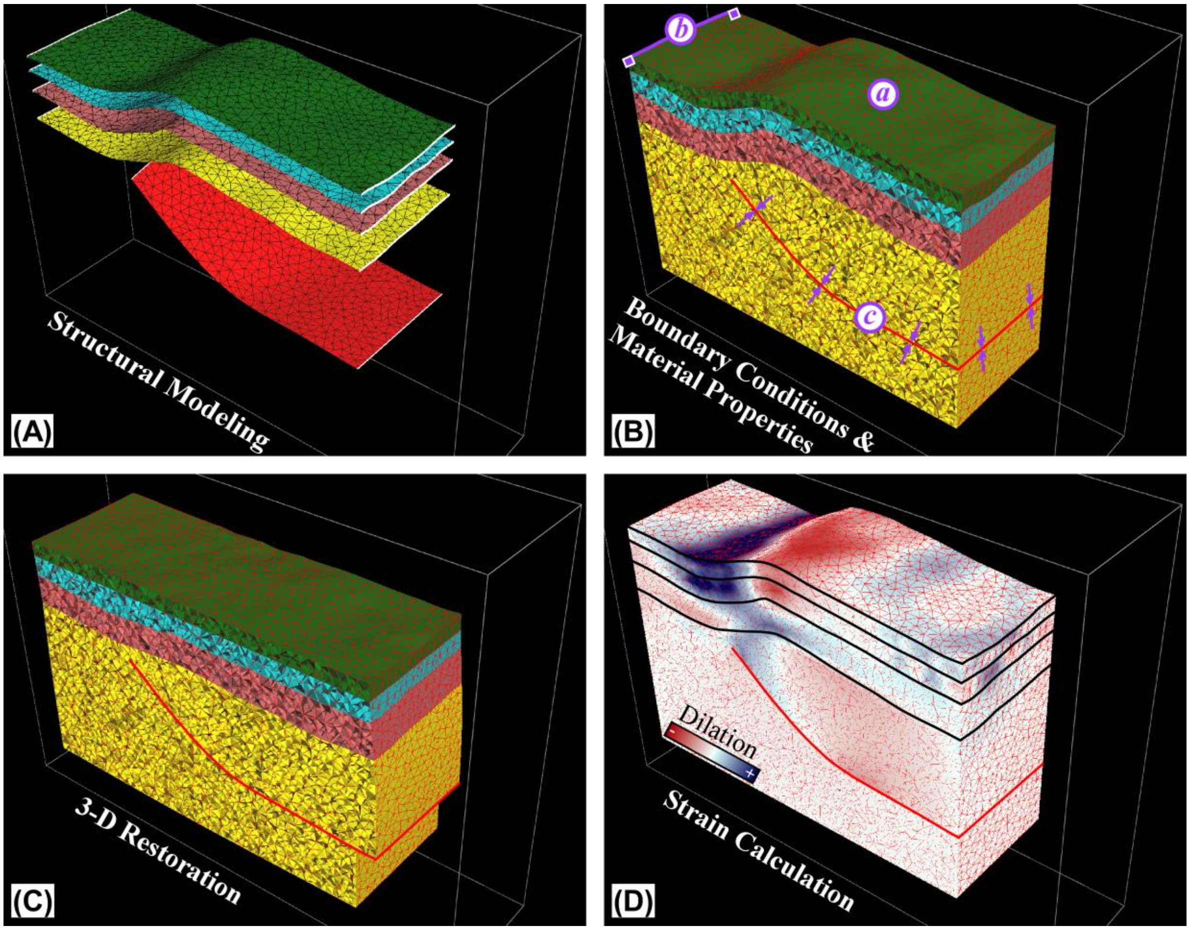

Figure 4.1: General workflow for geomechanical restoration illustrated by a restoration of the Elsinore Anticline model used in this study. A) Structural modeling of 3-D geologic surfaces derived from interpretations of 3-D seismic reflection data and well logs. B) Generation of the volumetric mesh, referred to as the restoration model. Material properties are applied to each 3-D region. Boundary conditions are required for the restoration problem: *a*) datum of a deformed horizon, *b*) fixed boundary wall(s), *c*) fault compliance). C) Restored model after solving the defined restoration problem. D) Strain visualization for detailed analysis of the restoration result. See text for details.

In this study, we seek to evaluate if a new suite of 3D geomechanical restoration methods (e.g. Figure 4.1) can be used to effectively model fault and fracture patterns in petroleum reservoirs. Kinematic cross section- and map-based methods have been developed over the past few decades in attempts to model structural growth and the associated strain patterns (e.g., Allmendinger, 1998; Egan et al., 1999; Rouby et al., 2000; Griffiths et al., 2002; Benesh et al., 2014). However, these techniques are limited in that they do not explicitly consider stress or variable rock strengths. A new generation of geomechanical methods may address some of these concerns (e.g., Muron, 2005; Maerten & Maerten, 2006; Moretti et. al., 2006; Durand-Riard et. al., 2011; Chauvin et al., 2015). Specifically, geomechanical restorations incorporate mechanical rock properties, including stratigraphic variations in rock strengths, and are able to address the inherent three-dimensional nature of deformation (e.g., Guzofski et al., 2009; Plesch et al., 2007; Durand-Riard et al., 2013). Moreover, these restorations can employ geologically reasonable boundary conditions, such as restoration of datum horizons and fault displacements.

The current generation of restoration tools utilize simple, linear or non-linear elastic constitutive laws to model large, permanent rock strains. Geomechanical forward models that similarly use elastic constitutive laws have proved valuable for understanding the inherent 3-D nature of fold development (e.g., Shackleton & Cooke, 2007) in addition to 3-D stress and strain patterns of fault-related fold growth (e.g., Cooke & Pollard, 1997; Bellahsen et al., 2006). However, there are important physical limitations to the elastic stress-strain relationships employed in current geomechanical restoration methods that must be considered. These methods seek to address this limitation by incorporating faults, detachments, and bedding plane slip surfaces that separate the models into many small elastic regions. Moreover, the methods can recover small increments of deformation with stress relaxation to model large strains. Despite these approaches, however, it seems reasonable to conclude that geomechanical restoration methods may be limited in their abilities to precisely define stress and strain. Thus, in this study we employ an objective, empirical approach to assess the viability of these strain predictions by comparing them with independent geophysical attributes and dynamic well production data.

In this study, we employ a 3-D geomechanical restoration method (Muron, 2005) to assess the impact of tectonic strain on reservoir performance within a natural gas reservoir – the

Lower Devonian Thirtyone Formation – in the Oates SW field, Delaware Basin, West Texas (Figure 4.2). Using well logs and a 3-D seismic reflection survey, we build a 3-D structural model of the Paleozoic Atoka-Ellenburger stratigraphic section, including several prominent fault-related folds that serve as structural traps in the Oates SW field. We restore our 3-D structural model using horizon and fault displacement boundary conditions, and calculate rock strain from the resulting displacement fields. In conjunction with these restorations, we generate a 3-D semblance volume from our seismic data to serve as a proxy for natural rock strain. We seek to validate the restoration method as a predictor of natural rock strain by quantifying the correlation between modeled strain distributions and semblance throughout the Thirtyone reservoir in the study area. We further explore the viability of the method by addressing the impact of reservoir scale strains on the production histories of vertical and deviated natural gas wells in the Oates SW field.

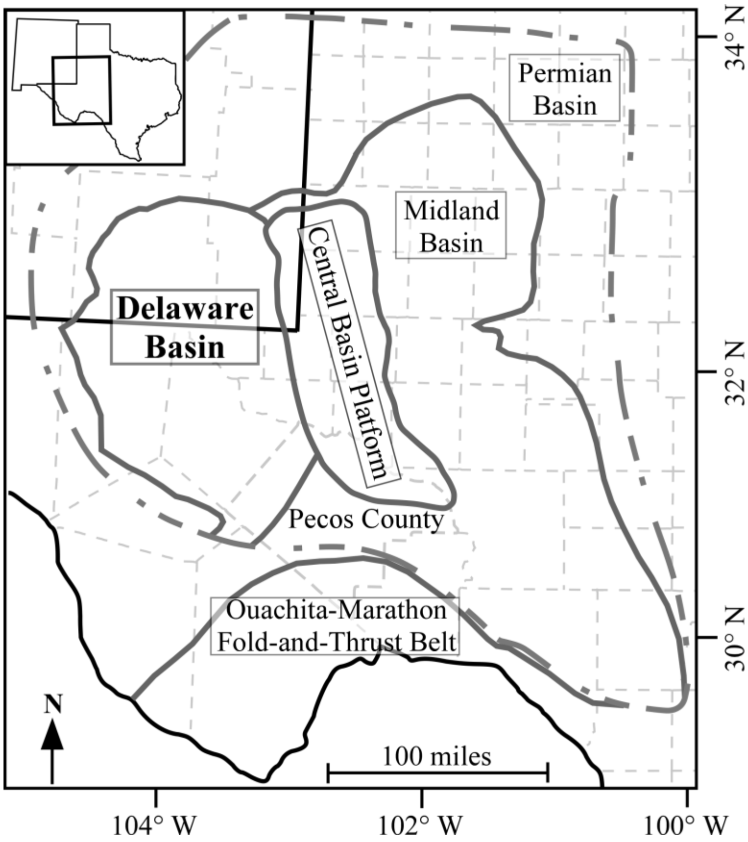

Figure 4.2: The Permian Basin (dashed lines) of West Texas and New Mexico is composed of the Midland Basin, the Central Basin Platform and the Delaware basin. To the south is the Ouachita-Marathon fold-and-thrust belt that formed in the Early Pennsylvanian. This case study focuses on a natural gas field in the southern Delaware Basin within Pecos County, TX.

Geomechanical Restoration

Structural restoration is the process of retro-deforming tectonic-induced strains accumulated over geologic timescales (e.g., Dahlstrom, 1969). Standard restoration methods remove fault offsets while simultaneously unfolding geologic structures. Most traditional methods follow line-length or area balancing constraints, or are governed by kinematic rules to recover deformation. In contrast, new 3-D geomechanical restoration methods use finite-element methods governed by constitutive relationships that define rock strength and mechanical stratigraphy, providing a more physics-based approach to structural restoration. These developments have provided the ability to address fully 3-D aspects of deformation history for complex geologic structures while also providing insight into the effects of rock properties and property contrasts on strain distributions associated with structural growth (e.g., Guzofski, et al., 2009). In the following sections, we provide a concise description of the general restoration approach and workflow. For a more detailed description of the methodology, we refer the reader to Muron (2005), Maerten & Maerten (2006), Guzofski et al. (2009), and Chauvin et al. (2015).

Geomechanical Restoration Methodology

The geomechanical restoration tool used in this study applies the finite element method (FEM) coupled with a dampening algorithm to restore 3-D geologic structures while minimizing changes in volume and global energy-state of the restoration model (Muron & Mallet, 2004; Muron, 2005). This method restores a stratigraphic surface within the volume to a defined datum level while simultaneously honoring additional boundary conditions, which commonly include: 1) a fixed pin line, fixed walls, or sliding walls within the model; 2) displacement of the walls or local fault slip constraints; and 3) fault compliance constraints, requiring adjacent fault blocks to remain in contact across the fault surface. A linear or non-linear elastic constitutive relationship governs the strength of model elements within fault-bounded blocks during the restoration. This geomechanical approach incorporates isotropic rock properties – such as Young's Modulus and Poisson's Ratio – that can vary between different sub-volumes of the model. Moreover, the method does not prescribe a specific kinematic theory or velocity field to direct a structural restoration. Rather, the restoration result is primarily controlled by the defined boundary conditions and material properties. A model is considered restored when all boundary conditions are satisfied in the absolute minimum strain-energy state (Muron & Mallet, 2004). Our extensive testing of geomechanical restoration, in addition to previous studies (e.g., Lovely et al., 2012), indicates the importance of defining geologically constrained boundary conditions. Non-physical restorations can lead to inaccurate interpretations of structural growth and reservoir strain distributions.

As structural restoration seeks to remove permanent rock strain over geologic timescales, we recognize there are inherent limitations to the linear-elastic constitutive relationship in our restoration tool. In theory, this approach should restore infinitesimally small increments of folding and faulting. In practice, this is typically not possible due to limits on our knowledge of deformation path over these small increments. We attempt to overcome these limitations by restoring modest stages of deformation. With growth (i.e. syn-tectonic) strata, sequential restoration is possible by incrementally restoring each growth section in succession (e.g., Guzofski et al., 2009; Vidal-Royo et al., 2012). In a similar vein, restorations of modestly deformed structures that lack growth strata have been able to accurately model strain distributions using a single-step restoration (e.g., Plesch et al., 2007; Durand-Riard et al., 2013). The restoration tool utilized in this study has been able to overcome some limitations of the linear-elastic simplification by dividing a structural model into sub-volumes bounded by stratigraphic horizons, fault ramps, and detachments. Thus, while each sub-region retro-deforms elastically, the full model bears large-scale, permanent strain influenced by fault displacements. Indeed, several studies have found this method of geomechanical structural restoration to be well suited for modeling strain orientations and their relative magnitudes distributed through 3-D geologic structures and stratigraphic formations (e.g., Maerten & Maerten, 2006; Moretti et al., 2006; Plesch et al., 2007; Guzofski et al., 2009; Shokair et al., 2009; Vidal-Royo et al., 2012; Durand-Riard et al., 2013). In this study, we seek to extend this geomechanical restoration method to characterize reservoir scale structures that impact observed production trends from a naturally fractured reservoir in the Delaware Basin, West Texas (Figure 4.2).

Geomechanical Restoration Workflow

The 3-D geomechanical restoration workflow used in our study first requires a topologically consistent 3-D structural model of surfaces representing the faults and stratigraphic horizons of interest (Figure 4.1A). These surfaces are often generated from interpretations of depth-converted 3-D seismic reflection data and well logs. Ensuring topologic consistency of all surface contacts produces several volumetric regions of varying spatial dimension that are stored within the structural model: 3-D region volumes bounded by stratigraphic and/or fault surfaces; 2-D region surfaces (e.g., geologic and boundary surfaces); 1-D region line contacts of intersecting surfaces (e.g., hanging wall and footwall fault contacts); 0-D region node contacts (e.g., end-points of 1-D regions). The structural model and contact data are used to generate a volumetric mesh composed of tetrahedral elements, which we refer to as the restoration model (Figure 4.1B). Isotropic material properties are defined in each 3-D region of the restoration model by Young's Modulus (E) and Poisson's Ratio (ν), or Lame's First (λ) and Second (μ) parameters. The last step of model set-up requires defining geologically and physically reasonable boundary conditions (Figure 4.1B). Typical boundary conditions include flattening a deformed datum surface, holding a node, line and/or surface fixed in one or more direction, defining fault compliance, and restoring fault offsets. With material properties and boundary conditions applied to the model, the restoration tool can solve the assigned restoration problem. After numerical convergence to a minimum strain-energy state (Muron & Mallet, 2004), a restoration vector and strain tensor are calculated at each node of the model. Using these outputs, the 3-D model can be displayed in the restored state (Figure 4.1C) and individual components of strain – such as strain invariants – can be calculated for a detailed analysis of strain distributions (Figure 4.1D).

Geologic Setting of Oates SW Field

We use the geomechanical restoration tool described above to assess the impact of tectonic strain on production trends from the Lower Devonian Thirtyone Formation in the Oates SW field, southern Delaware Basin, West Texas (Figure 4.2, 4.3). The Thirtyone reservoir is a cherty dolomite that exhibits characteristics of a naturally fractured reservoir (Ruppel & Hovorka, 1995; Montgomery, 1998; Saller et al., 2001; Billingsley, 2006). In the Central Basin Platform, the Thirtyone reservoir is thought to have spatially heterogeneous primary porosity and permeability, often controlled by the original depositional attributes such as chert abundance and facies geometry (Ruppel & Hovorka, 1995; Montogmery, 1998). However, fracturing and faulting has complicated reservoir property variabilities by developing compartmentalization, preferred flow paths and potentially flow barriers (Ruppel & Hovorka, 1995; Montgomery, 1998).

Production from the Lower Devonian Thirtyone in the Oates SW field, Delaware Basin (Figure 4.2, 4.3) has exhibited similar heterogeneities in production trends. Some wells have been shut-in soon after initial production due to low flow rates, whereas cumulative production in several wells has exceeded 1 BCF gas (Billingsley, 2006). Water cut has been similarly inconsistent, with no clear pattern between or even within individual structures. Indeed, water incursion is a significant concern in places, with cumulative water production exceeding 8 MM bbl in the most water-rich well of the field (Billingsley, 2006). Thus, the Lower Devonian Thirtyone reservoir in the Oates SW field (Figure 4.3) is an ideal test case for applying our geomechanical restoration tool for reservoir characterization.

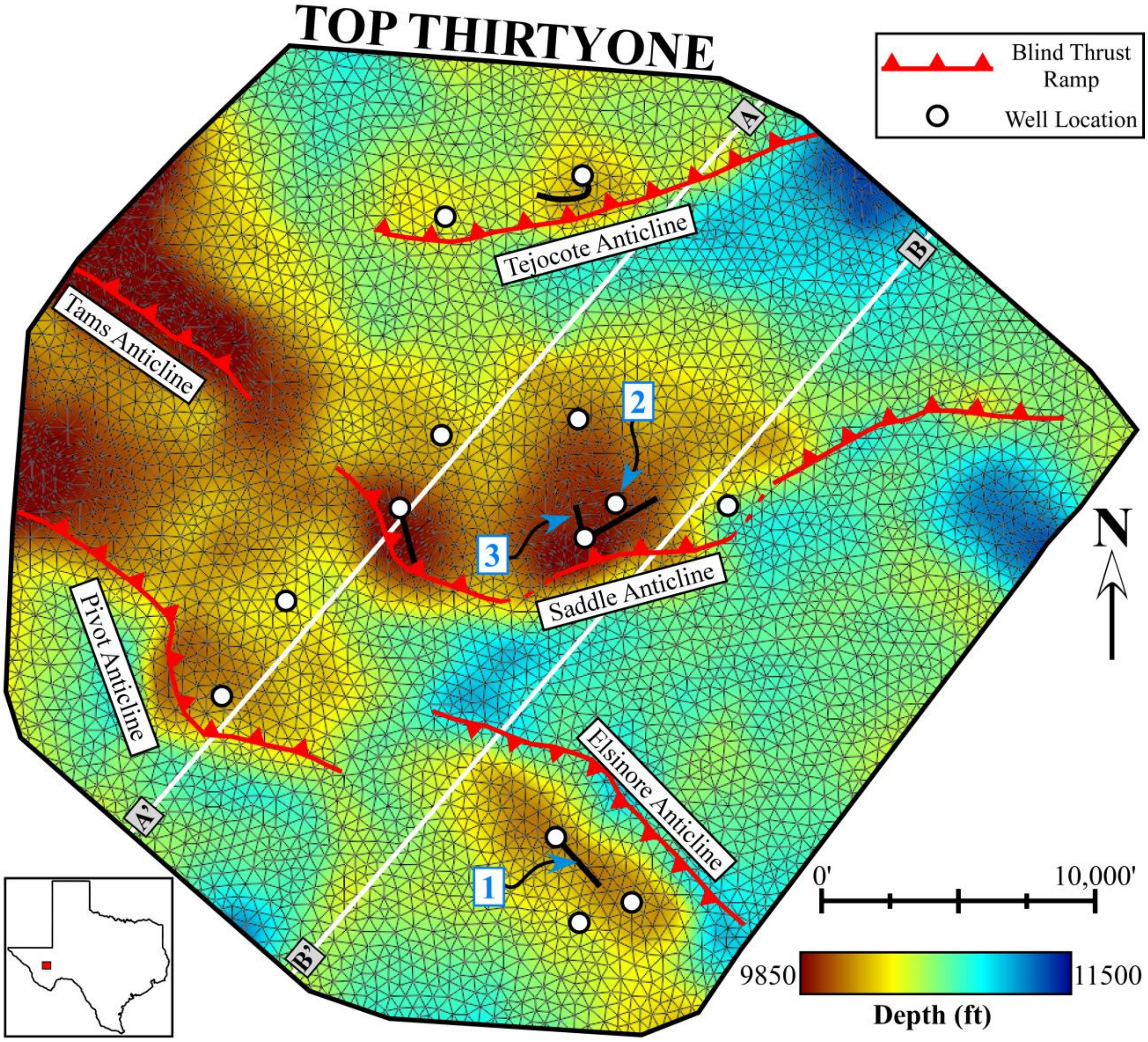

Figure 4.3: Structure map of the Lower Devonian Thirtyone Formation, the primary reservoir target in the Oates SW field, West Texas (Figure 4.2). Sections A-A' and B-B' are shown in Figure 4.5.

Paleozoic Stratigraphy

This study focuses on the Lower Ordovician-Lower Pennsylvanian stratigraphic interval in the Oates SW field (Figure 4.4). The deepest unit clearly imaged in the seismic data is the Ellenburger Group, a Lower Ordovician carbonate (Figure 4.4). Regionally, the Ellenburger Group has undergone significant diagenesis, including extensive dolomitization, tectonic fracturing, and karstification. As a result, Ellenburger can be quite permeable and source undesirable levels of water to shallower reservoirs in the presence of vertical flow networks (e.g., Loucks, 2006). Above the Ellenburger sits the Middle Ordovician Simpson Group (e.g., Suhm & Ethington, 1975; Frenzel et al., 1988). The Simpson is a thick group of interbedded limestone, shale and sandstone (Figure 4.4). The Upper Ordovician is marked by the Montoya Formation. Montoya is a carbonate deposit that has been almost entirely dolomitized (Pope, 2014). In addition, abundant chert within the Montoya is present throughout West Texas, including our study area (Figure 4.4), interpreted to indicate a period of strong marine upwelling (Pope, 2014). The Lower Devonian marks the deposition of the primary reservoir in the study area, the Thirtyone Formation. Thirtyone is another cherty dolomite (Figure 4.4). In Oates SW, the abundance of chert within the Thirtyone is likely to be laterally heterogeneous and perhaps even discontinuous, akin to other nearby fields (Ruppel & Barnaby, 2001). The Thirtyone is overlain by the Upper Devonian Woodford shale. Through much of the study area, Woodford is followed in stratigraphic succession by the Mississippian Barnett shale and Lower Pennsylvanian Atoka sandstone (Figure 4.4).

Structural Interpretation

The primary tectonic activity deforming the Paleozoic Ellenburger-Atoka units in West Texas occurred during Late Paleozoic Ouachita-Marathon Orogeny, marking the closure of the proto-Atlantic Ocean (e.g., Hills, 1985; Shumaker, 1992), immediately south of our study region (Figure 4.2). Using a depth-converted 3-D seismic reflection survey and industry well logs, we interpreted the major stratigraphic units deformed by the Ouachita-Marathon collisional event and characterized the prominent structures defining the major structural traps in the field. Our structural interpretations of the major traps are presented in Figure 4.5. The Paleozoic section of interest is well imaged and allows for straightforward mapping of the fold structure within this unit. We generally observe structures to be characterized by wide, gentle back limbs with steeper, narrow forelimbs (Figure 4.5A). The geometries of the folds in section A-A' (Figure 4.5A) are consistent with an anticlinal fault-bend fold structural style (Suppe, 1983). We do not

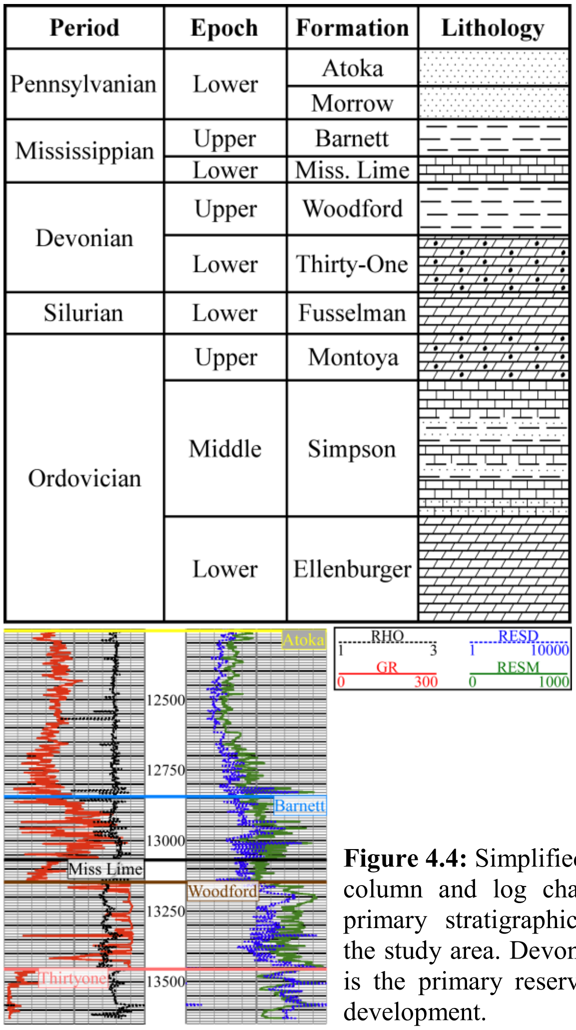

Period	Epoch	Formation	Lithology
Pennsylvanian	Lower	Atoka	
		Morrow	
Mississippian	Upper	Barnett	
	Lower	Miss. Lime	
Devonian	Upper	Woodford	
	Lower	Thirty-One	
Silurian	Lower	Fusselman	
Ordovician	Upper	Montoya	
	Middle	Simpson	
	Lower	Ellenburger	

Figure 4.4: Simplified stratigraphic column and log character of the primary stratigraphic intervals in the study area. Devonian Thirtyone is the primary reservoir target for development.

observe the continuation of axial surfaces or folded reflectors below our Top Ellenburger interpretation. Thus, we interpret the upper detachment of the fault-bend folds to be at or near the top Ellenburger (Figure 4.5A). The deeper units are not well-imaged, making it difficult to directly interpret the fault ramp geometry beneath the anticlinal folds from offset reflectors or direct fault-plane reflections. Thus, we use the observed fold shape to interpret the geometry of the thrust ramps at depth (e.g., Suppe, 1983; Shaw et al., 2005). These thrust ramps generally dip in the NW, N and NE directions. The seismic data do not suggest the presence of a prominent syncline in the backlimbs of the structures that would indicate a shallowing of thrust ramps to a basal detachment level (Suppe, 1983). Thus, we interpret these structures to be basement-involved anticlinal fault-bend folds (Figure 4.5A). This structural style describes the Pivot, Tams, Saddle and Tejocote structures (Figure 4.3, 4.4A).

Our interpretation of the Top Ellenburger marker in section A-A' (Figure 4.5A) suggests it is folded in the hanging wall of some structures, despite serving as an upper detachment surface. This observation is consistent with a break-forward sequence of thrusting (e.g., Shaw et al., 1999). In this interpretation, the Tejocote structure formed initially, followed in sequence by the Saddle and Pivot folds, respectively (Figure 4.5A). We do not observe any significant stratigraphic thickness changes across these structures that would indicate the presence of growth stratigraphy constraining the timing of fold development. However, most of the reflectors between the interpreted Lower Wolfcampian horizon and the Atoka formation are relatively undeformed (Figure 4.5). Thus, faulting and associated uplift of the fault-related folds in Oates SW likely occurred shortly after Early Pennsylvanian. Moreover, the lack of significant deformation in strata above Top Atoka indicates the lack of, or perhaps limited, deformation associated with the Late Cretaceous-Early Cenozoic Laramide Orogeny in the western continental United States (e.g., Dickinson & Snyder, 1978).

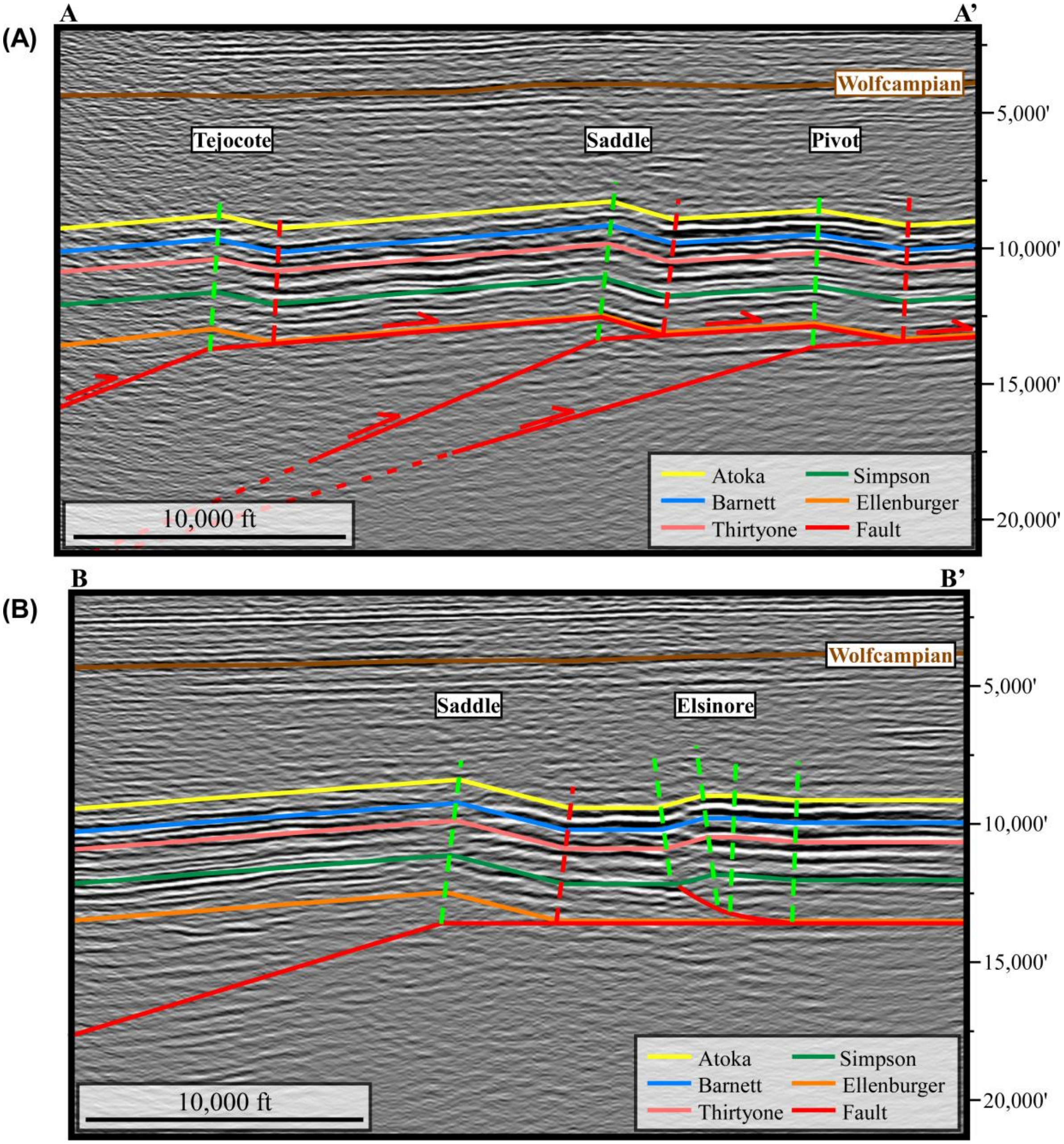

Figure 4.5: Structural interpretation of the Atoka-Ellenburger interval across the study area. A) Section A-A', interpretation of basement-involved anticlinal fault-bend folds. A regional upper detachment lies along the Top Ellenburger. These structures developed in a break-forward sequence of thrusting (e.g., Shaw et al., 1999). See text for details. B) Section B-B', interpretation of the Saddle and Elsinore structures. The Elsinore is a fault-propagation fold, in contrast to the other prominent traps in Oates SW. Top Ellenburger serves as the basal detachment for the Elsinore Thrust, shielding the Ellenburger from hanging wall deformation in this region. See text for details. Line locations shown in Figure 4.3.

The Elsinore fold in section B-B’ (Figure 4.5B) is distinct from the structural style of the other major traps. The Elsinore structure exhibits a northeastern vergence, whereas the other structures have vergence directions generally in the range of SSE-SSW (Figure 4.5). This suggests the underlying Elsinore Fault dips to the SW, approximately opposite to the other major fault dip directions (Figure 4.5B). Moreover, we observe offset reflectors between our interpreted Simpson and Ellenburger levels, indicating the presence of a thrust ramp above the Top Ellenburger detachment. Lastly, we interpret a synclinal axial surface pinned to the tip of this observed thrust (Figure 4.5B). These observations indicate the Elsinore Anticline is best described as a fault-propagation fold (Suppe & Medwedeff, 1990; Shaw et al., 2005). Notably, the Top Ellenburger serves as a basal detachment for the Elsinore Thrust whereas it serves as an upper detachment for the other fault-related folds. This basal detachment for the Elsinore structure shields the Ellenburger Group – and its potential water source – from hanging wall deformation in the vicinity of the Elsinore structure.

Three-Dimensional Geomechanical Restorations

Structural Models

We used our fault and horizon interpretations of the seismic and well log data to build 3-D geologic surfaces in the Gocad modeling environment (Mallet, 1992). We use these surfaces to construct our volumetric mesh for restoration. Given the size and complexity of the structures, it was most efficient from both a modeling and computational standpoint to divide our regional model of the Oates SW field into sub-domains (Figure 4.6A). Following our interpretation of a break-forward thrusting sequence (Figure 4.5), we split the Oates SW field into four structural domains: 1) Pivot Anticline; 2) Elsinore Anticline; 3) Saddle and Tams Anticlines; and 4)

Tejocote Anticline (Figure 4.6A). We restored each of these 3-D geologic models separately to characterize the Lower Devonian Thirtyone reservoir throughout the Oates SW field.

We included the following surfaces as stratigraphic layers in each model: Top Atoka, Top Barnett, Top Thirtyone, Top Simpson and Top Ellenburger. Fault surfaces and detachments were included in each structural model as well (e.g., Figure 4.1). Moreover, we removed any observed regional dip of the Top Ellenburger detachment surface from each restoration model, allowing us to restore horizons to a horizontal datum. After restoration, the regional dip is restored to each model for subsequent analysis. We note that restoring any regional dip to a 3-D model after restoration does not rotate the output restoration vectors nor the strain tensors, as these outputs are defined within a local coordinate system of the 3-D volume. Separate rotations must be applied to the restoration vectors and strain tensors to ensure all components of the restoration result are in a consistent frame of reference.

Boundary Conditions

Fault-Bend Fold Models

For each fault-bend fold restoration model – the Pivot, Tams+Saddle, and Tejocote Anticlines – we restore the Top Atoka surface to a horizontal reference elevation. Our structural interpretation (Figure 4.5) indicates both the Atoka and Thirtyone intervals are pre-growth strata, thus a datum applied to the Atoka should fully restore the Thirtyone. An additional boundary condition is applied to one side of the model such that it can only move in the dip-slip and vertical directions. Fixed-wall boundary conditions have been shown to aid the restoration problem by providing a frame of reference (e.g., Guzofski et al., 2009; Durand-Riard et al., 2013). Fault compliance boundary conditions are also defined (e.g., Figure 4.1B); we force all displacement along faults during restoration to occur in the hanging wall of the model. Although

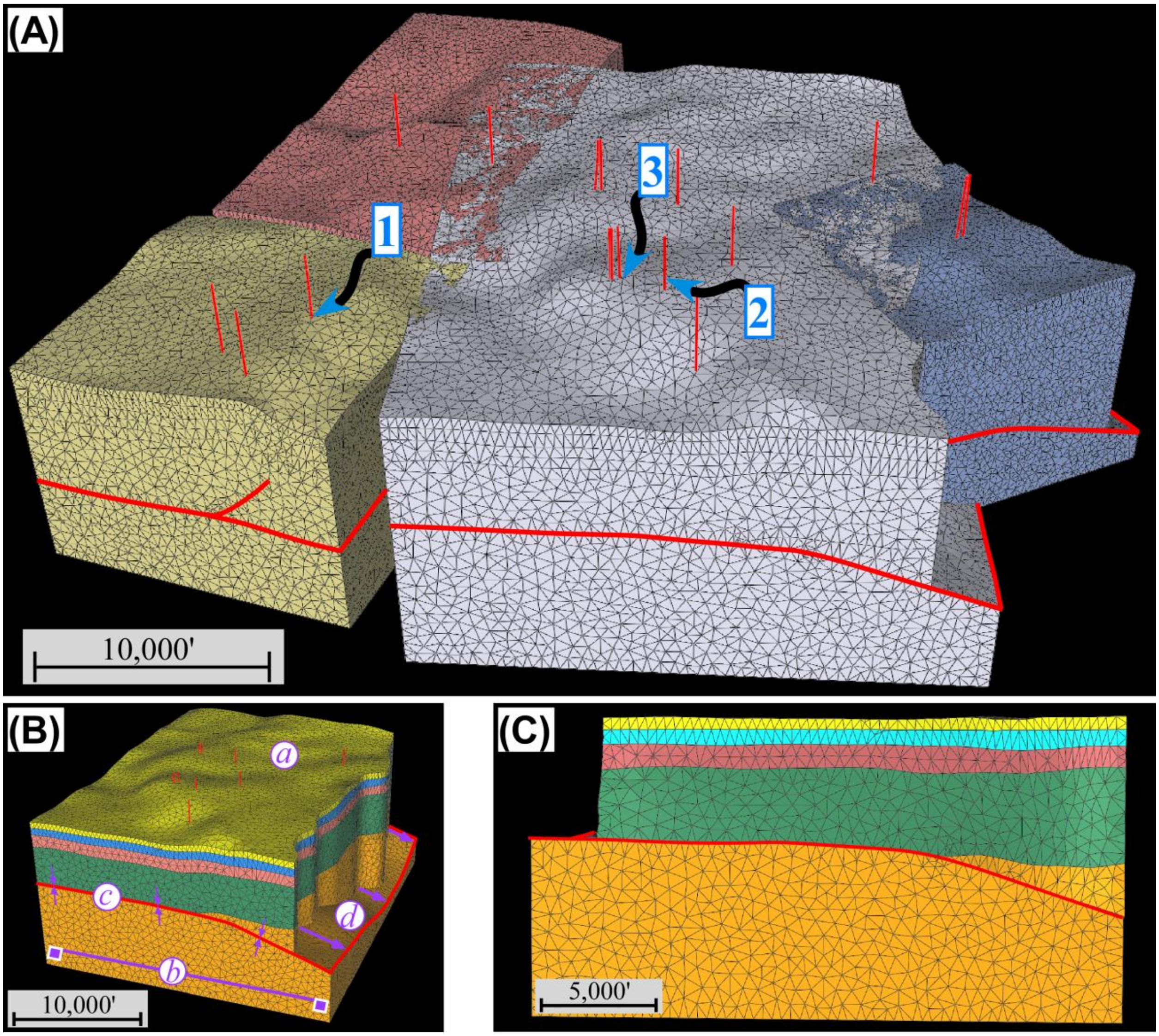

Figure 4.6: Geomechanical restoration models of structural traps in the Oates SW field. A) The regional structural model was broken into separate structural domains, requiring four volumetric meshes to restore all of the structures in the study area. B) Material properties are applied to each sub-volume of a restoration model. Boundary conditions are also required for the restoration problem. Boundary conditions for the fault-bend fold models include: *a*) a datum horizon; *b*) a boundary wall fixed in one direction, *c*) fault compliance, and *d*) a fault slip constraint. See Figure 4.1B for boundary conditions applied to the Elsinore Anticline model. C) The restored model.

this assumption is not necessarily an accurate description of near-fault deformation observed in nature, we deem it to be a reasonable first-order approximation of fault-related folding over geologic timescales. As our restoration tool does not adhere to a specific kinematic model or geometric theory during restoration, it is generally difficult to produce a geologically reasonable restoration of fault-bend folds without providing fault offsets to govern the direction of motion, which are not present in our 3-D models (Figure 4.5). This challenge arises because the restoration of a datum horizon can simply flatten the folded intervals by imposing translation in many different directions along the upper detachment. In effect, this amounts to a near vertical flattening of the fold. To overcome this challenge, geomechanical restorations generally rely on hanging wall and footwall cut-offs (e.g., Guzofski et al., 2009) or a boundary wall displacement that reflects fault slip (e.g., Durand-Riard et al., 2013). In this study, we developed a workflow that defines a fault slip estimate from the anticlinal fold width (Suppe, 1983) and implements this as a boundary wall displacement in the hanging wall of the fault (Figure 4.6B; Appendix F). This offset boundary wall serves as the fault slip constraint on the thrust ramp, acting to drive hanging wall motion across the underlying thrust fault in the appropriate, down-dip direction during restoration (e.g., Figure 4.6C). This boundary condition guides the restoration tool to produce a geologically reasonable restoration path, and avoids some other pitfalls associated with restorations that lack sidewall boundary conditions (Lovely et al., 2012).

Fault-Propagation Fold Model

As described above, the Elsinore structure stands out from the other prominent folds in the Oates SW field (Figure 4.5B). Relative to the anticlinal fault-bend folds, the Elsinore Anticline is characterized by 1) an opposite vergence and fault dip direction, 2) a different structural style, and 3) the presence of a basal detachment, not an upper detachment. Therefore, the boundary conditions for the Elsinore restoration (Figure 4.1B) were slightly modified relative to the fault-bend fold models (Figure 4.6B). Similar to the other restoration models, we restored the Top Atoka unit to a planar surface and limit movement of one sidewall to the dip-slip and vertical directions (Figure 4.1B). In addition, we define fault compliance and restrict all motion to the hanging wall fault block. As the Elsinore structure is a fault-propagation fold, all of the fault slip is consumed at the fault tip (e.g., Suppe & Medwedeff, 1990), precluding any large-scale motion beyond the anticlinal forelimb. Therefore, we fix the NNE boundary wall of the Elsinore anticline (in the foreland of the fault tip) in the dip-slip direction (Figure 4.1B). Another difference compared to the fault-bend fold models is that we do not define a fault slip boundary condition for the Elsinore Anticline model (Figure 4.1B). The absence of an upper detachment surface and the pinned foreland boundary wall were sufficient boundary conditions to generate geologically reasonable restoration slip directions and magnitudes (Figure 4.1C).

Material Properties

Material properties, particularly property contrasts, can impart a strong influence on the strain distributions of thrust sheets (e.g., Erickson, 1996; Hughes et al., 2014; Morgan, 2015). For each restoration model, we defined a Young's Modulus (E) and Poisson's Ratio (ν) to govern the strengths of each stratigraphic layer. Although mechanical properties can be estimated using well logs, these values are not necessarily representative at the scale of an entire field due, at least in part, to unknown heterogeneities in lithology, fracture density, porosity and permeability. Therefore, we used synthetic values for E and ν to define our model strengths. To assess the effect of mechanical stratigraphy on our restoration results, we tested a suite of restorations using deformable and rigid definitions for rock strengths. Deformable regions are assigned material properties of: $E=3.5*10^9$ Pa and $\nu=0.325$. In contrast, rigid regions are defined by: $E=3.5*10^{10}$ Pa and $\nu=0.225$. Our extensive testing with this restoration tool has found that – all other variables being equal (e.g., boundary conditions) – material property contrasts can significantly affect restoration results, but that the absolute magnitudes of these properties within reasonable limits have little effect on the restoration outcomes.

We tested the 32 unique combinations (2^5) of material property definitions on each of the four structural models, yielding 128 geomechanical restorations (e.g., Figure 4.1, 4.5). For each restored model, we assess the residual structural relief and modeled strain distributions along Top Devonian to determine whether the defined material property contrasts generates a geologically reasonable restoration. If a combination of material properties yields a reasonable result for all four structural models, we treat that combination of material properties as viable for our modeling purposes. Our analysis found that models with rigid Barnett and Devonian layers yielded the least amount of residual structural relief across the Top Thirtyone surface. We suggest this occurs because the layers are sufficiently rigid to transmit the applied forces on the Top Atoka to the Top Thirtyone surface within the restoration models. Thus, these models were able to most effectively restore the structural relief across the Thirtyone reservoir. Of these seven models, we assessed the modeled strain distributions across the Devonian layer at ~164 ft (50 m) vertical intervals. We anticipated strains to be localized in the anticlinal forelimbs, with lower magnitude strains in the broad, gentle back limbs. Moreover, we seek models that produce negative restoration dilation in the fold crest and positive restoration dilation in the fold limbs (e.g., Figure 4.1D). This strain distribution is consistent with numerous mechanical forward models of fault-related folds (e.g., Erickson & Jamison, 1995; Cooke & Pollard; 1997; Strayer & Hudleston, 1997; Strayer et al., 2004; Bellahsen et al., 2006; Benesh, 2010; Hughes et al., 2014). Two of the remaining material property definitions passed this strain assessment in all four restoration models. These two models differ only by the strength of Atoka. We continued our analysis with rigid Atoka models as the strain distributions of the two remaining material property combinations were nearly identical and the differences in residual structural relief across the top Thirtyone surface was, at most, 2.7 ft (0.8 m) for all four restoration models. In the following section, we assess the accuracy of these modeled strain distributions by comparing them to independent measures of natural rock strain.

Strain-Semblance Analysis

Modeled Strain Patterns

We merge the strain results from each of the four restoration models, allowing us to extract the strain distributions onto the Top Thirtyone 3-D surface for subsequent analysis. To avoid non-physical strain predictions associated with the fault slip boundary conditions and other edge effects, we omitted near-edge regions of each model from our strain analysis. This led to a slightly reduced surface-area extent of modeled strain for analysis than the total mapped coverage of Top Thirtyone (Figure 4.3). However, the limits of our semblance calculations controlled our final extent for analysis (discussed below).

We extract I_1 and I_2 components of strain onto the Top Thirtyone surface, to isolate volume changes and shear strains, respectively, across the Thirtyone reservoir (Appendix G). The restoration results across the Oates SW field indicate dilation is concentrated in the prominent anticlinal forelimbs (Figure 4.7A), which are steeper and more narrow than the corresponding back limbs (Figure 4.5). There are relatively modest magnitudes of dilation in the back limbs of the structural traps. Figure 4.7B illustrates similar distributions of distortional strain across the Top Thirtyone. Interestingly, along-strike variations in I_2 within the anticlinal forelimbs (Figure 4.7B) correspond to along-strike variations in structural relief (Figure 4.3), which is a function of fault slip for fault-bend and fault-propagation folds (Suppe, 1983; Suppe & Medwedeff, 1990). In addition, the restorations predict lower magnitude distortional strain in the back limbs of the prominent structures, similar to the patterns observed for dilation in Figure 4.7A. Together, these first-order strain patterns defined by the restorations are consistent with observations of natural structures and forward mechanical models of similar structural styles (e.g., Erickson & Jamison, 1995; Strayer et al., 2004; Hughes et al., 2014). However, the local distributions and patterns of each strain type have noticeable differences, which may indicate variations in how strain associated with secondary structures is manifest within the Thirtyone reservoir. These variations have the potential to impart heterogeneities in reservoir character across the Oates SW field that can impact hydrocarbon development, such as secondary porosity and changes in permeability.

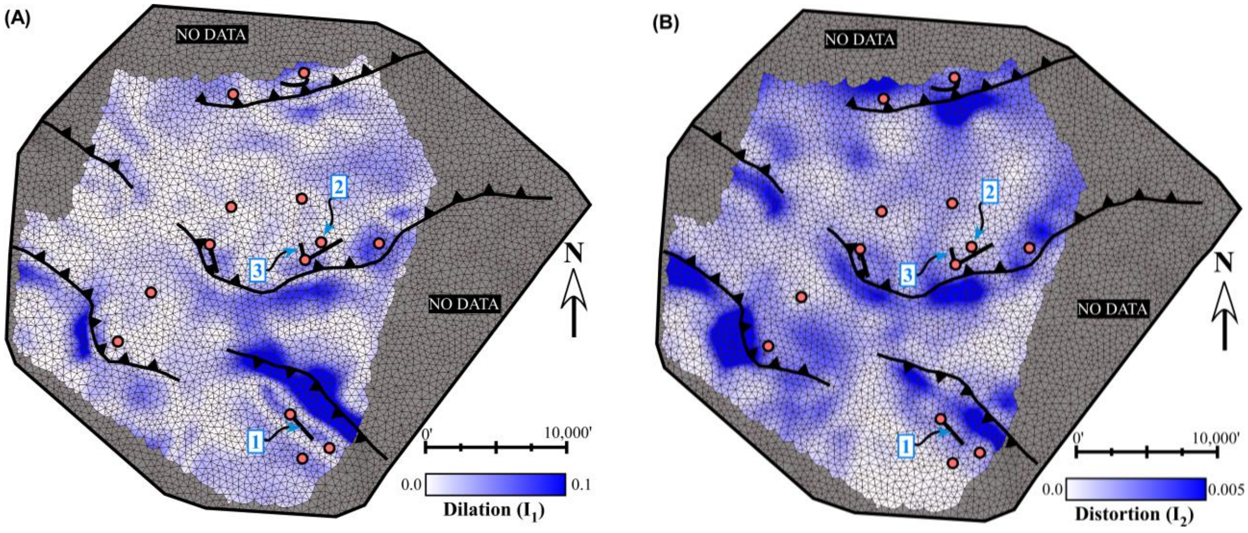

Figure 4.7: Calculated strain distributions across the Top Devonian Thirtyone horizon. A) Magnitude of dilatational (I_1) strain. B) Distortional (I_2) strain magnitudes. The geomechanical restorations indicate the majority of strain across the Top Thirtyone surface is localized in anticlinal forelimbs. Subtle strain signatures are predicted in the back limbs of each structure as well. See text for details.

Natural Rock Strain

In order to assess whether the restoration strains effectively represent deformation in the Oates SW structures, we compare the modeled strain patterns to an independent measure of natural rock strain. For this purpose, we rely on semblance, a coherency-based seismic attribute, to serve as a proxy for natural strain (Marfurt et al., 1998). Semblance is measured as the similarity of a stacked seismic trace relative to adjacent traces within a defined depth range (Bahorich & Farmer, 1995; Marfurt et al., 1998). This geophysical attribute is measured from zero to unity; a semblance value of zero represents total dissimilarity between two adjacent stacks whereas a semblance of unity indicates total similarity. Accordingly, semblance is a measure of the lateral continuity of acoustic impedance and has been shown to be quite effective in the identification of macro-scale, secondary, and sub-seismic faults and fracture zones (e.g., Bahorich & Farmer, 1995; Marfurt et al., 1998; Shokair et al., 2009; Chopra & Marfurt, 2010; Frankowicz & McClay, 2010).

We extract semblance data onto the Top Thirtyone surface (Figure 4.8). The region of the well-imaged 3-D seismic data used to calculate our semblance volume limits the extent of analysis. We used a ~1066 ft (325 m) vertical window for the semblance calculation in order to discriminate between large-scale discontinuities due to the faults and folds likely represented in our starting model – and smaller-scale features that were generally not explicitly meshed in our restoration models. In addition, this large vertical window for the semblance calculation mutes local discontinuities associated with the local stratigraphy and minor processing artifacts (Bahorich & Farmer, 1995; Marfurt et al., 1998). Thus, we interpret low semblance features to indicate the presence of secondary structures, potentially imaged in the 3-D seismic data. The extracted semblance data (Figure 4.8) reveals wide, continuous, low semblance zones within the forelimbs of the major fault-related folds. These are interpreted to represent one or more faults that disrupt the seismic continuity. The locations of these secondary faults suggest that they are associated with fold growth (Figure 4.3, 4.7). In addition, we identified several tight, linear bands of low semblance that illuminate observable faults in the seismic data. Our subsequent mapping of these secondary faults from the 3-D seismic volume (e.g., Figure 4.8) indicates they are present in both the forelimbs and back limbs of structures, and support our interpretation of low semblance zones indicated faulted regions. We emphasize that these secondary faults are not explicitly represented in our restoration models.

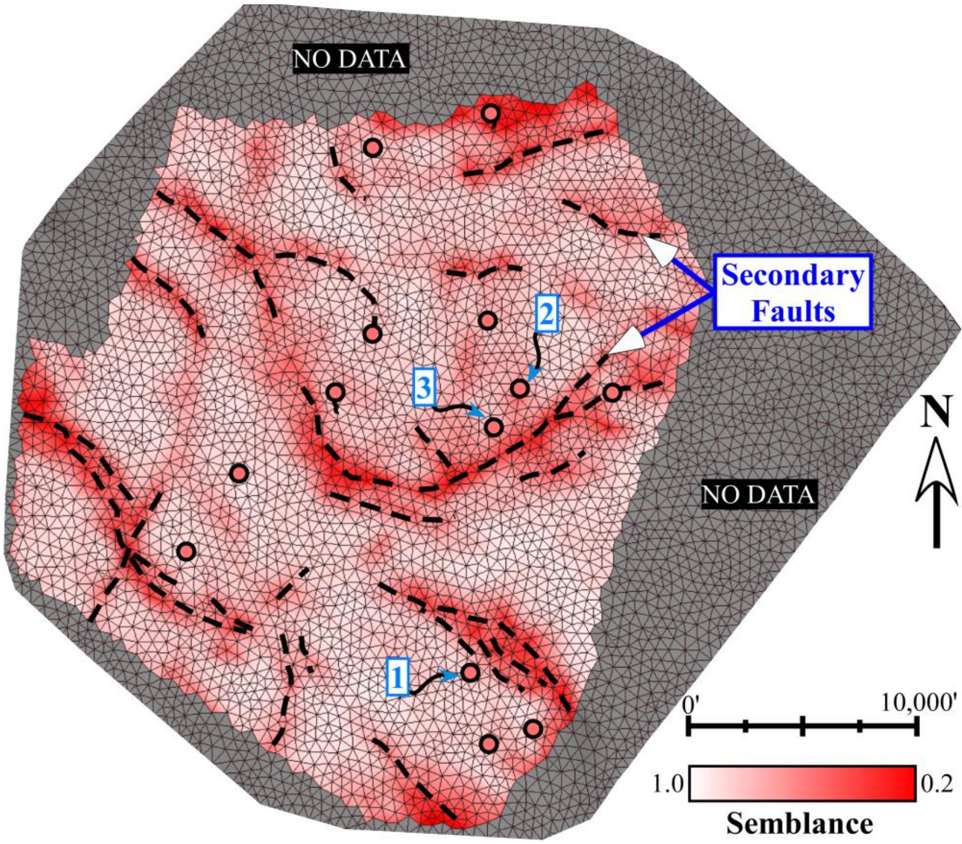

Figure 4.8: Semblance – used as a proxy for natural rock strain – extracted onto the top Thirtyone Formation surface. Semblance values are low where seismic reflectors are laterally discontinuous and high where they are more continuous. Low semblance values are concentrated in the anticlinal forelimbs of the Oates SW structures, consistent with the pattern of elevated strains in these regions (Figure 7). Linear semblance features in the forelimbs and backlimbs often illuminate secondary faults imaged in the seismic data that deform the Thirtyone reservoir. These secondary faults are not represented in the geomechanical restoration models. See text for details.

Strain-Semblance Correlations

We compare the strain distributions (Figure 4.7) with the spatial patterns of semblance across the Devonian Thirtyone reservoir (Figure 4.8), and identify a strong correlation between low semblance and elevated magnitudes of strain predicted by the geomechanical restorations. The increased dilation and distortion in anticlinal forelimbs (Figure 4.7) correlate particularly well with the low semblance values in the same areas across the structures in the Oates SW field (Figure 4.8). To quantitatively assess these correlations we generated Model-II (i.e. reduced major axis; geometric mean) regressions between strain and semblance within the Devonian reservoir across individual structures. A Model-II regression is a linear regression approach that treats both variables as dependent with an unknown error variance (Rayner, 1985). The results of

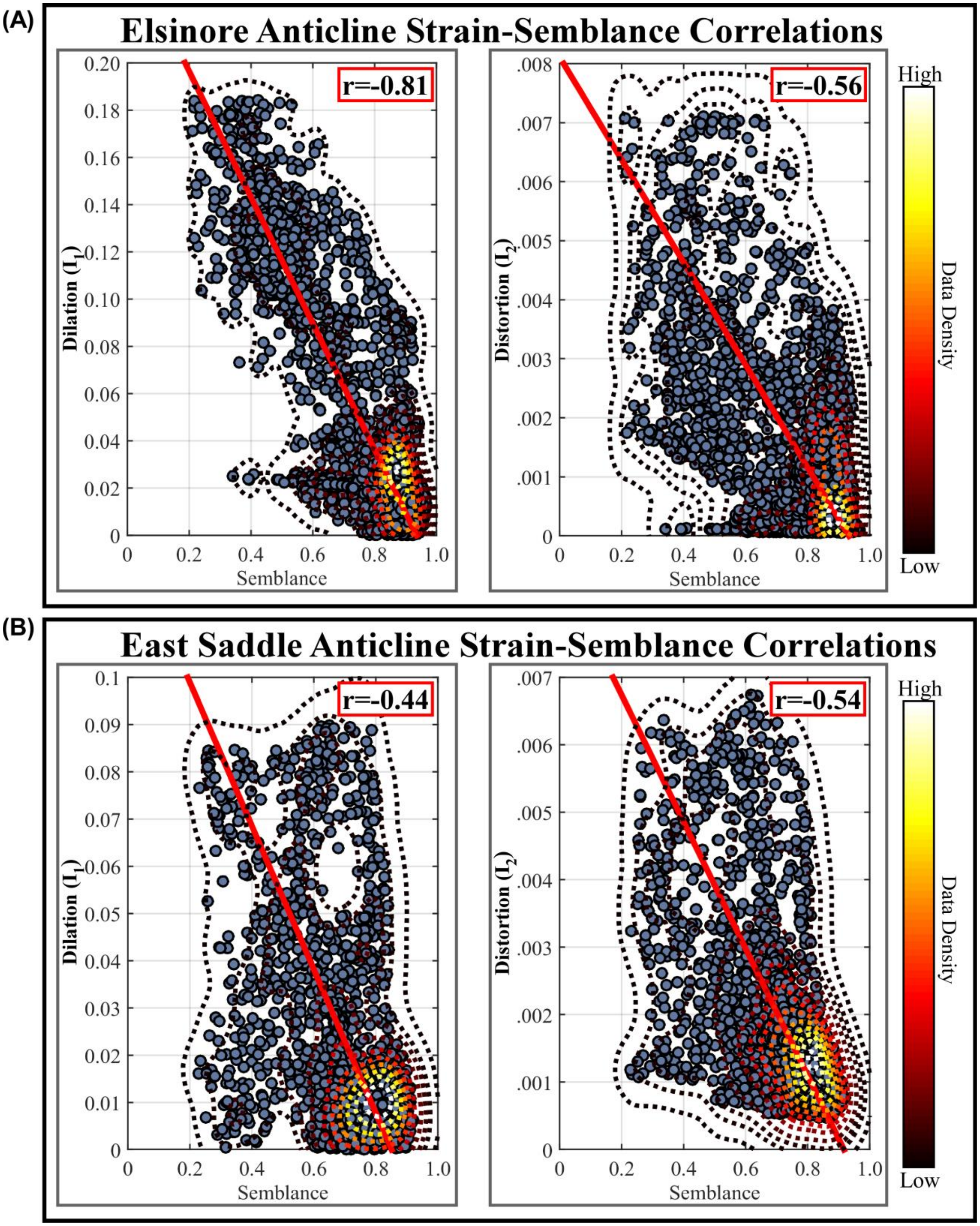

Figure 4.9: Strain-semblance Model-II regressions (Rayner, 1985) across two of the structural traps in the study area. A) Elsinore Anticline, which includes Well-1 (Figure 4.3). B) Central Saddle Anticline, which includes Well-2 and Well-3c (Figure 4.3). The negative strain-semblance correlations for both dilation and distortion suggest the geomechanical restorations accurately modeled strain associated with primary and secondary structural growth.

our I_1-semblance and I_2-semblance regressions are presented in Figure 4.9. For both structures, there is a clear trend of decreasing semblance with increasing strain, indicated by the negative slopes of the best-fit regression line. Moreover, the leftward tilt of the outer data density contours further suggests this inverse relationship. The negative correlation between dilation and semblance across the Elsinore Anticline (Figure 4.9A) is particularly strong (r=-0.81). In addition, the Central Saddle structure exhibits a moderately strong negative I_2-semblance correlation coefficient (r=-0.54). The structure of the data density contours in this regression plot each exhibit a leftward tilt, further supporting this correlation (Figure 4.9B). These correlations, combined with our ability to explicitly map secondary faults that correlate with highly and moderately strained regions (Figure 4.7, 4.8), support our finding that the geomechanical restoration method used here can accurately model strain distributions without explicitly including secondary structures in the volumetric mesh. Thus, we conclude that geomechanical restoration can serve as a viable tool for accurately modeling secondary fault and fracture distributions in deformed reservoirs. In the following section, we continue our characterization of the Lower Devonian Thirtyone reservoir in the Oates SW field by incorporating dynamic well data.

Reservoir Characterization using Geomechanical Restorations

The Oates SW field (Figure 4.3) began producing gas in the 1950's. Development of the field has been dominated by completing vertical wells, with the majority of perf zones producing gas from the Thirtyone reservoir. Currently, Abraxas Petroleum Corporation operates the field and produces gas from open-hole horizontal wells drilled by Abraxas in the mid-2000's (Billingsley, 2006). Legacy and recent production across the field have encountered heterogeneities in reservoir performance. Vertical wells within the Pivot anticline (Figure 4.3)

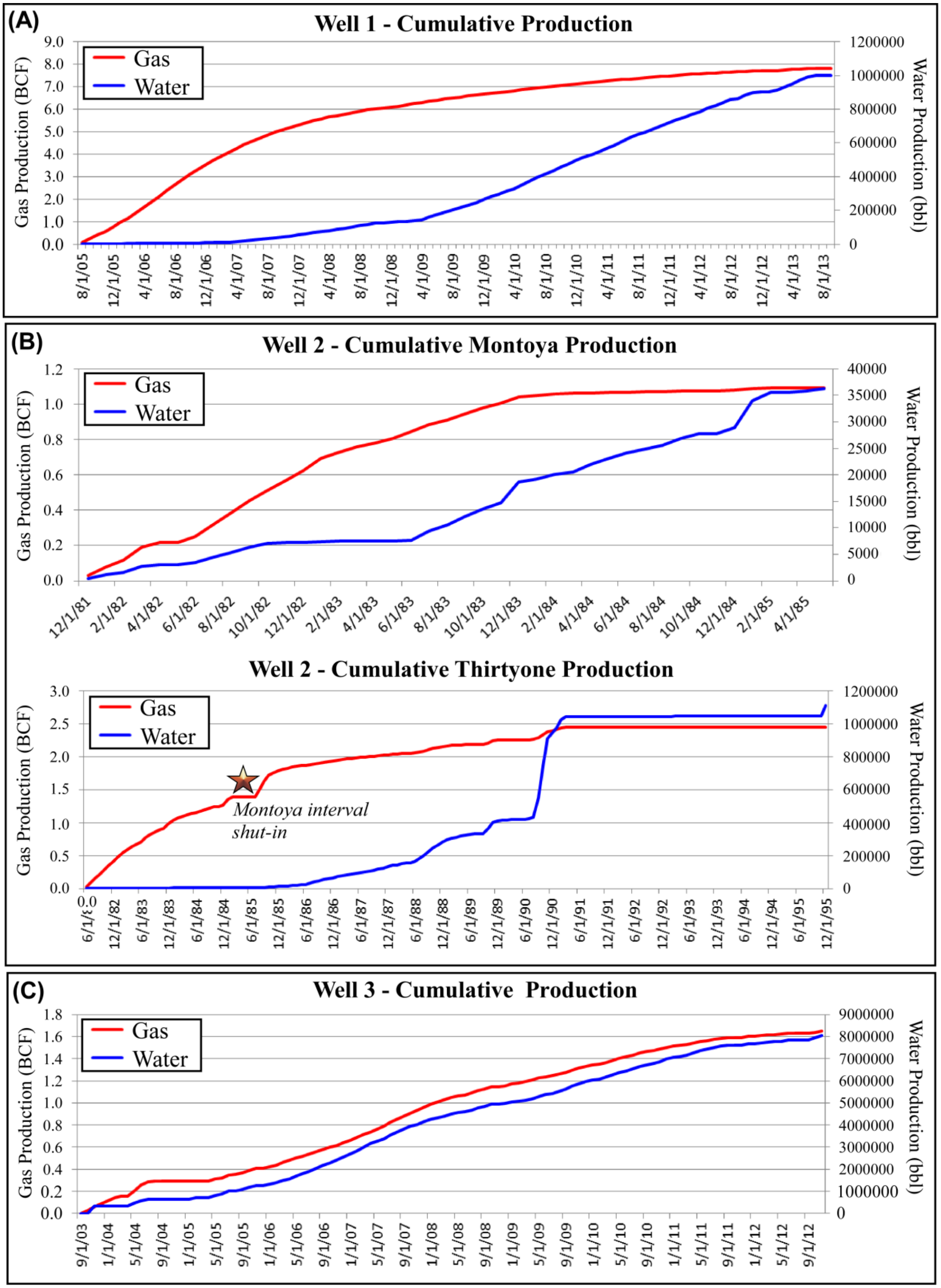

Figure 4.10: Production data of three different wells across Oates SW Field. See text for details.

produced negligible amounts of hydrocarbons, whereas the most productive structure – The Elsinore Anticline – has produced ~10 BCF to date, including 8 BCF from one horizontal well. Moreover, water cuts have ranged from modest to substantial (Billingsley, 2006). Figure 4.10 presents cumulative production curves of three wells – two horizontal and one vertical – in the study area, highlighting some of the production variability in the Oates SW field. In this final section, we investigate the impact of tectonic strain and structural growth on reservoir properties and production trends for these three wells in the Oates SW field.

Well-1

Well-1 (Figure 4.3) is a horizontal well drilled by Abraxas Petroleum in the mid-2000's within the Elsinore Anticline, a fault-propagation fold (Figure 4.5B). Well-1 produces from an interval ~175 ft (~50 m) below the top of the Devonian Thirtyone. The lateral azimuth is SE, parallel to the trend of the structural crest (Figure 4.3). Open-hole production from this lateral segment has exceed 8 BCF natural gas – the most of any well in the field – and 1 MM bbl water to date, with water cut increasing through the life of the well (Figure 4.10A). Figure 4.11 presents the strain and semblance trends along the lateral section of Well-1. Beginning at the heel of the lateral, dilation (Figure 4.11A) is a maximum magnitude (>3.0%) and quickly decreases away from the heel, to a minimum (<1.5%) in the first 1/3 of the total lateral length. The middle third remains at very low dilatational strain, ranging between <1.5% and ~2.0%. Continuing across the the outer third of the lateral segment, dilatation then increases to ~2.5% (Figure 4.11A). The trend of distortional strain is quite similar, strains are a minimum in the middle third of the lateral section and increase in both directions toward the toe and heel of the well (Figure 4.11C). Figure 4.11B depicts the semblance variations along Well-1. We observe relatively low semblance magnitudes near the heel of the lateral and across most of the first third of the lateral section. Semblance then increases to a maximum magnitude across the middle third of the lateral segment. Continuing toward the toe, semblance decreases to a local minima before increasing again at the toe (Figure 4.11B).

In summary, there is elevated strain and lower semblance along the outer sections (i.e. the heel and toe) of the Well-1 horizontal section. In contrast, the middle section of the lateral is characterized by greater semblance and minimal amounts of strain. These findings indicate a strong, negative correlation between both strain properties, dilation and distortion, and semblance along the much of the lateral section of Well-1, consistent with the negative strain-semblance correlations at larger scales (e.g., Figure 4.9). Thus, we conclude there is a structural control on the strain and semblance values along the Well-1 lateral track.

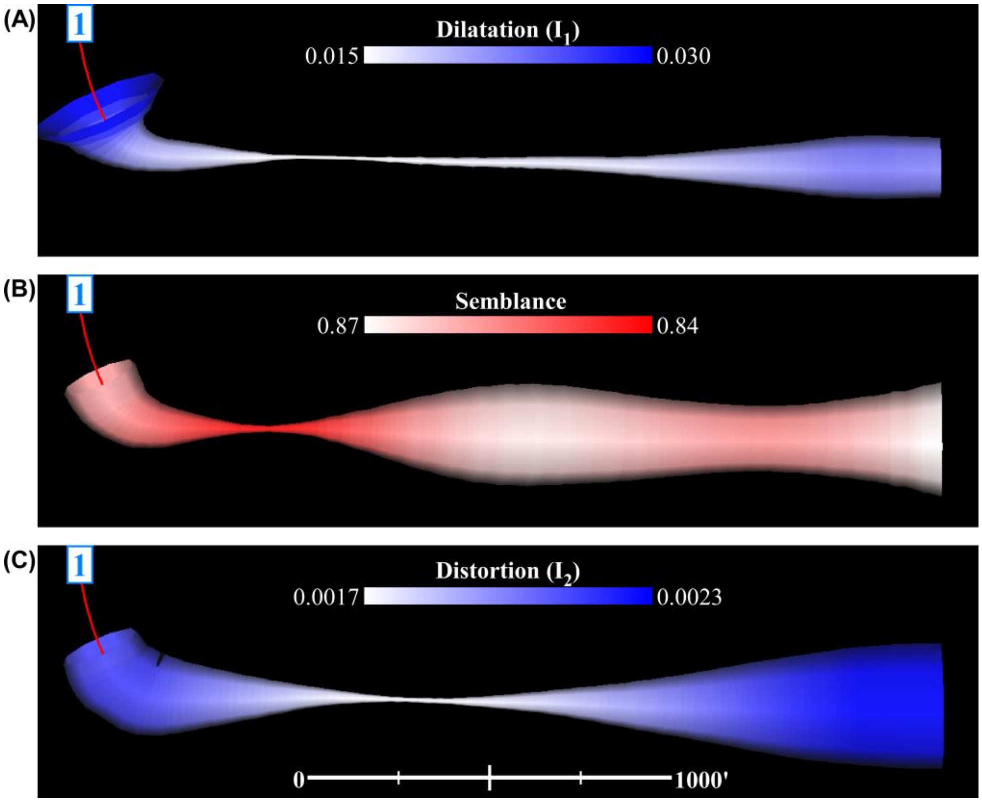

Figure 4.11: Strain and semblance values along Well-1. A) Dilatation (I_1); B) Semblance; C) Distortion. The radius of each plot scales with the magnitude of each attribute. To estimate these values along the wellbore, we sample the strain and semblance data are sampled at ~165 ft (50 m) intervals along the wellbore. At each interval step, the mean values of strain and semblance are calculated within a ~325 ft (100 m) spherical radius of the wellbore.

Figure 4.12A visualizes distortional strain along the outer third – near the toe – of the Well-1 lateral with the nearby seismic imaging. In this perspective view, we observe a distinct, narrow kink band within the Top Barnett-Base Devonian interval around the wellbore. This subtle fold limb is coincident with the increase in distortional and dilatational strain along the well path (Figure 4.12A). We suggest this kink band reflects elevated amounts of strain in this region of the borehole, consistent with the elevated strain predictions from our restorations and the lower semblance in this section of the lateral (Figure 4.12). This folding may have led to enhanced natural fracturing yielding a pocket of enhanced permeability, likely improving the productivity of the Well-1 reservoir, consistent with the 8 BCF of gas production to date (Figure 4.10).

Figure 4.12B is the same perspective as Figure 4.12A, but now viewing the Well 1 path in the middle third of the lateral where semblance is relatively higher and both strain measures are near minima. Indeed, neither the Barnett nor Devonian section are folded, indicating the kink band observed in the outer third of the well bore is a local feature and does not extend into this region of the lateral. This further supports our interpretation of a structural origin to the strain and semblance trends along the lateral section of Well-1. Specifically, we suggest the kink band in Figure 4.12A is the cause for the increased strain and decreased semblance observed near the toe of the Well-1 lateral segment. This result supports the viability of geomechanical restorations to predict subtle strain patterns in fractured reservoirs that may influence reservoir properties. The vertical extent of the kink band penetrated by Well 1 may also shed light on its water production history. Notably, the kink band is limited to the Barnett-base Devonian section and, thus, does not extend far above or below the reservoir. This restricted interval of folding – and corresponding high strain – would presumably limit the vertical extent of any enhanced

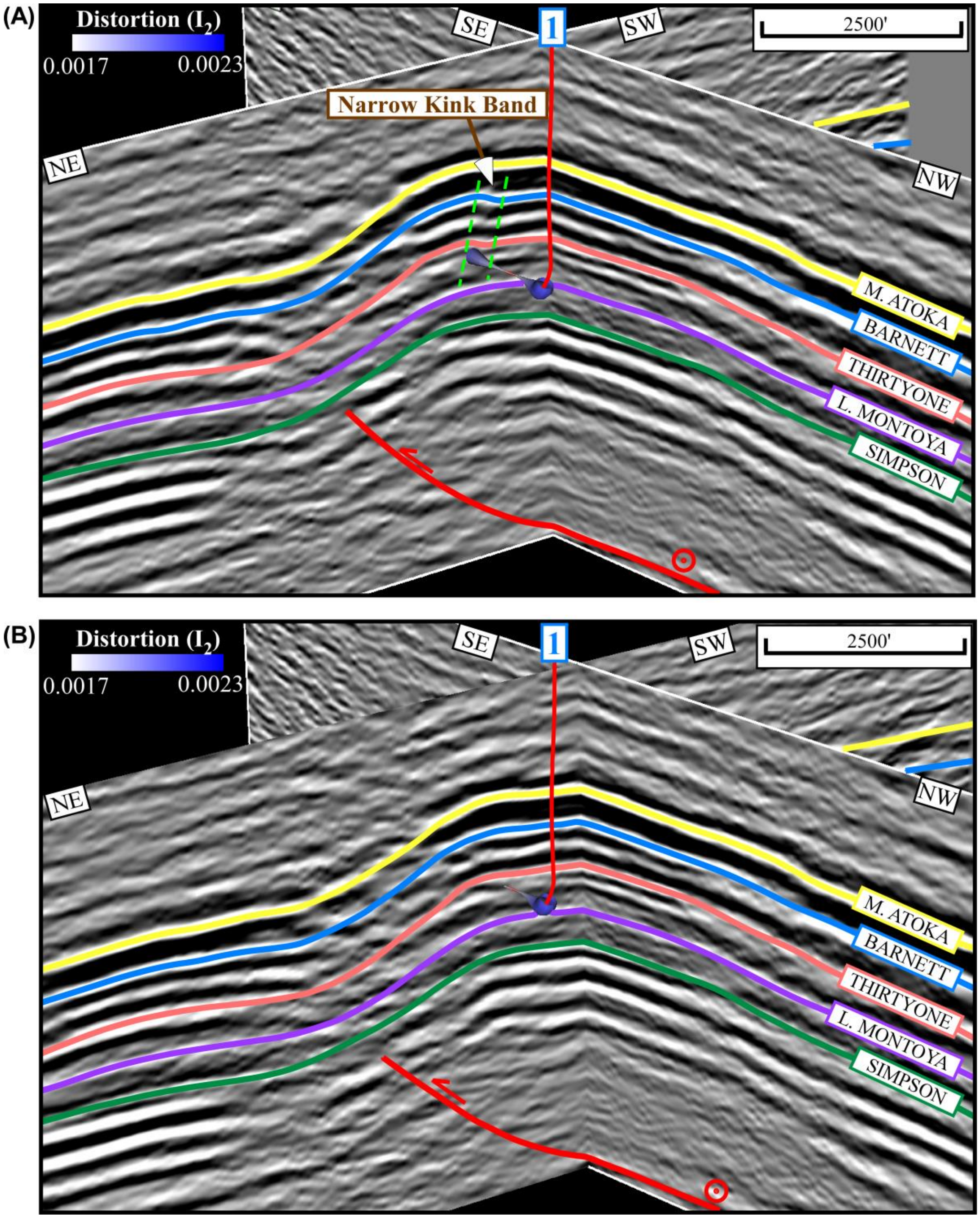

Figure 4.12: A) A region of increased strain and decreased semblance in the outer third of Well-1 lateral (Figure 4.11) corresponds to a narrow kink band – imaged in the 3-D seismic data – localized within the Barnett-Devonian interval. B) In the middle third of the well path – where modeled strain and semblance are relatively lower and higher, respectively (Figure 4.11) – the narrow kink band in Figure 4.11A is not present. These observations suggest strains caused by very subtle fold limbs can be resolved by our geomechanical restoration tool. See text for details.

permeability. Thus, increased water charge from adjacent aquifers would not be expected, which is consistent with the observed water production trends for Well-1 (Figure 4.10). Moreover, structural style may be an additional barrier to water incursion. We interpret the Elsinore structure as a fault-propagation fold that soles into the Top Ellenburger detachment (Figure 4.5B). The stratigraphic level of this detachment may effectively shield the underlying water-rich Ellenburger (Loucks, 2006) from the overlying hanging wall deformation and reservoir. This could further limit the vertical flow pathways from the Ellenburger, preventing significant water charge into the Thirtyone reservoir. Together, these three structural interpretations – 1) local fold limbs generating enhanced fracture permeability along the well bore; 2) folding and enhanced permeability confined to the Barnett-Devonian stratigraphic sections; and 3) the Thirtyone reservoir shielded by the basal detachment from the underlying Ellenberger Formation – provide a viable explanation for the significant gas production and typical water cuts in Well-1 of the Oates SW field.

Well-2

Well-2 (Figure 4.3) is a legacy vertical well drilled in the early 1980's. This well originally produced from the Montoya Formation, immediately below the Devonian Thirtyone. Shortly after initial production, the operator began production from a second interval in the uppermost Thirtyone using a separate line of production tubing (Figure 4.10B). 22 months after production commenced from the Thirtyone interval, the Montoya production line was shut-in. Immediately following shut-in of the Montoya section, there was a temporary surge in production from the Thirtyone production line (Figure 4.10B), implying vertical pressure communication between these two reservoirs. In total, Well-2 produced in excess of 3.5 BCF, with a fairly modest water cut.

In Figure 4.13, we visualize the seismic imaging at the location of Well-2, overlain by the calculated semblance. In addition, we display the distortional strain (I_2) predicted by our geomechanical restoration along the vertical wellbore within the Devonian-Montoya interval. Well-2 is drilled in a section of relatively low semblance, likely indicating the presence of secondary structures leading to seismic reflector discontinuities. Indeed, our interpretations of possible secondary faults in the seismic data suggest two or more secondary faults adjacent to Well-2 (Figure 4.13). These faults cause small-scale folding and/or reflector offset observed in the seismic reflection data. We interpret the downward increase in dilatational strain along the Well-2 borehole to be consistent with the presence of these secondary faults. We suggest this interpretation can also explain the observed production history for Well-2. In this interpretation, the secondary fault structures increased vertical permeability within the Devonian-Montoya

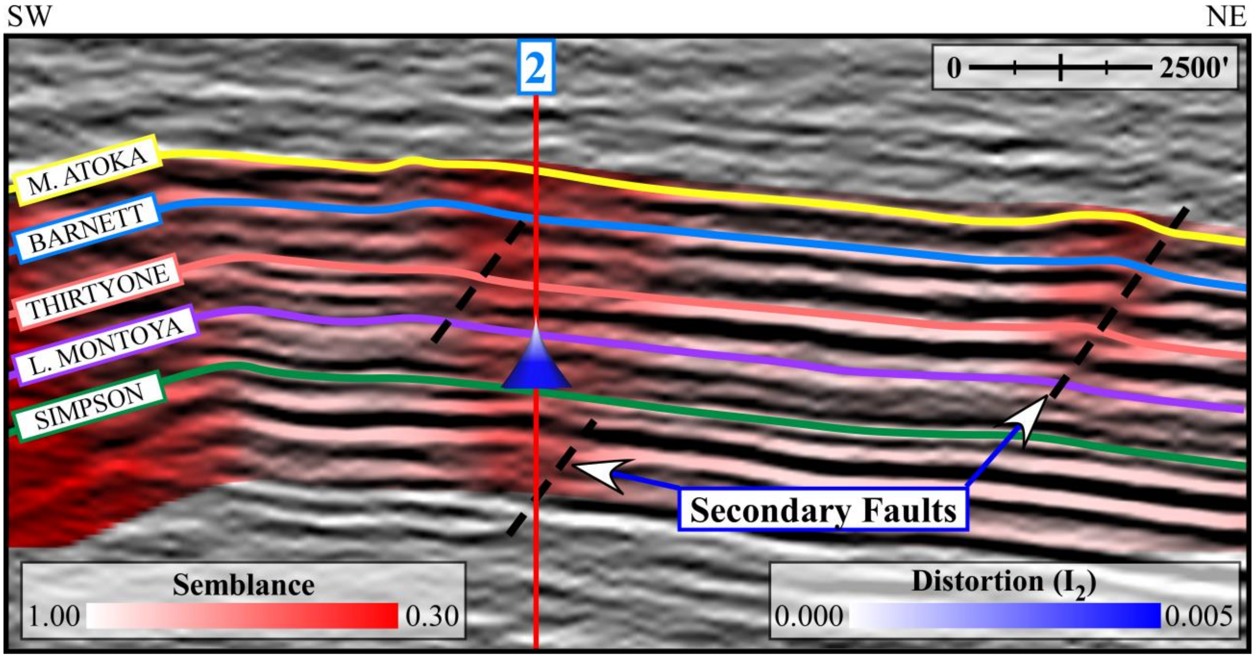

Figure 4.13: Seismic section through the location of Well-2. Semblance is overlain on the seismic reflector amplitudes. Distortional strain (I_2) is displayed along the Well-2 borehole within the Devonian-Montoya section. Well-2 was drilled in a region of decreased semblance, potentially due to the presence of secondary faulting. We suggest these small structures allow Montoya and Thirtyone to be in pressure communication, as indicated by the production spike after Montoya was shut-in (Figure 4.10). See text for details.

interval around Well-2. This facilitated pressure communication between the Montoya and Thirtyone reservoirs, thus explaining the observed Thirtyone production trends. After initial Thirtyone production, this interval begins to experience the initial stages of transient-state decline, while production from the Montoya continued (Figure 4.10B). However, immediately following shut-in of the Montoya interval, there was an abrupt spike in Thirtyone production, followed by typical production decline. We suggest the secondary faults within the low semblance region beneath and around the Montoya and Thirtyone reservoirs near Well-2 facilitated vertical communication between the Montoya and Devonian reservoirs.

Well-3

Well-3 constitutes a suite of three wells drilled in the backlimb of the Central Saddle Anticline (Figure 4.3). Well-3a is a legacy vertical section that produced from a perforated zone in the uppermost section of the Thirtyone reservoir. Total production included 1.8 BCF gas and 160 kbbl water. Water cut was initially low and increased during transient-state decline of gas production. Abraxas re-entered this vertical and drilled Well-3b, a horizontal well drilled with an ENE azimuth (Figure 4.3). This lateral targeted the Montoya reservoir, immediately below the Thirtyone (Figure 4.4). An image log of the lateral indicates the lateral encountered a prominent fracture set in the reservoir. These fractures had a dominant strike of ~N25W. Despite this seemingly ideal penetration of a natural fracture set perpendicular to the horizontal section, Well-3b experienced extremely low flow rates, totaling 9.0 MMCF gas and 32 kbbl water during the 10 months of production (Billingsley, 2006). The lack of economic flow rates suggests the penetrated fracture set did not produce sufficient secondary permeability to aid production. There are several mechanisms by which fractures will not enhance permeability and aid production. For example, under the appropriate stress conditions or in the presence of mechanical heterogeneities, natural fractures may not maintain dilatancy (e.g. Fischer & Jackson, 1999; Laubach et al., 2009). Similarly, open-mode fractures can be cemented soon after rupture depending on the structural fabric of the fracture set or when the rate of crystal growth exceeds the fracture propagation rate (e.g. Gale et al., 2010). It is worth noting that two or more dominant fracture orientations are common in contractional structures (e.g. Bellahsen et al., 2006), which can occur when two principal stresses have similar magnitudes or if stresses of unequal magnitude rotate. If economic flow rates require vertical charge from an adjacent region in this region of the Oates SW field, perhaps the fracture set encountered by Well-3b is confined to the producing reservoir interval, preventing charge and economic recovery (e.g. Odling et al., 1999). Alternatively, one or more additional fracture sets may dominate reservoir permeability and divert fluid flow away from a reservoir. An additional fracture set orientated approximately orthogonal to those imaged in Well-3b would likely go undetected by the image log.

After shut-in of the first lateral, Abraxas drilled Well-3c, a deviated well with a NNW azimuth, approximately perpendicular to the azimuth of Well-3b. Well-3c produces from the Lower Devonian Thirtyone reservoir, ~1650 ft (~500 m) SW from Well-2, but in the same structure (Figure 4.3). To date, Well-3c has produced 1.6 BCF gas, ~64% of the production from the Thirtyone production line of Well-2 (Figure 4.10C). However, Well-3c has produced 640% more water than the Thirtyone production line of Well-2 (Figure 4.10C).

Figure 4.14 presents the extracted dilation along the Well-3c lateral section and a cross-section across the Central Saddle fold. Strain is quite low along the entire borehole, and around the region of the lateral away from the fold crest (Figure 4.7). However, the strain and semblance patterns indicate a distinct zone of elevated strain and low semblance that is concentrated just beyond the heel of the lateral, within the forelimb of the Central Saddle anticlinal fault-bend fold

(Figure 4.7, 4.14). This zone of high strain is vertically continuous within the forelimb fold, extending through the Devonian reservoir into the underlying formations, including the Ellenberger (Figure 4.14). We speculate that the presence of vertical permeability associated with this highly strained zone near Well-3c may have facilitated water incursion from the Ellenburger Group, an abundant water source in the Permian basin (Loucks, 2006). In this interpretation, vertical flow paths from the Ellenburger to shallower sections are responsible for the elevated water cut in Well-3c relative to other wells in the field (Figure 4.10).

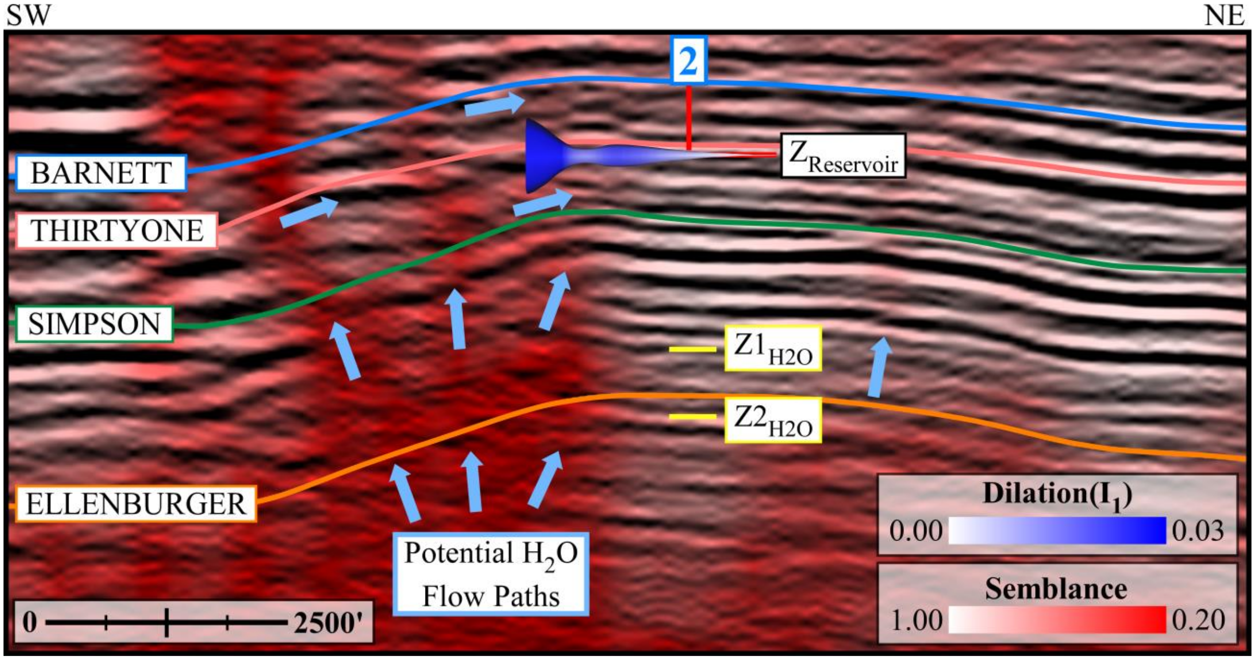

Figure 4.14: Seismic section through the Central Saddle Anticline in the vicinity of Well-3. Semblance is overlain on the seismic reflector amplitudes. Dilatation is displayed along the Well-3 borehole. We extend the display of I_1 from the heel of the lateral section to the anticlinal crest. Measured water temperatures at the wellhead suggest water produced from this location of the Thirtyone reservoir originates from a minimum depth that corresponds to the base Simpson or the uppermost Ellenburger. We suggest high strains developed during anticlinal fault-bend folding of the Central Saddle anticline formed vertical fault or fracture networks that facilitate water incursion from the Ellenburger Group water up the anticlinal crest of the Central Saddle structure into the Thirtyone reservoir (e.g., Figure 4.7, 4.8). See text for details.

To evaluate this prospect of vertical charge from the Ellenburger, we examine the water temperature encountered in Well-3c to infer its origin depth. The depth of the Well-3c lateral is ~13,390 ft (~4,080 m) subsea. Initial production from Well-3 recorded water temperature at the wellhead to be 198°F (92.2°C). The geothermal gradient has been modeled using temperature data from thousands of industry wells for the Delaware-Val Verde Basin region as:

$$Z = 3200.9 * \ln(T) - 10461$$

where Z is depth in meters, and T is temperature in degrees Celsius (Erdlac, 2006). Using wells only in Pecos County (Figure 4.2), the modeled geothermal gradient is:

$$Z = 3399.9 * \ln(T) - 11198$$

(Erdlac, 2006). These temperature gradients suggest the initial water production corresponds to depths of 13,200 ft (~4,025 m) and 13,725 ft (~4,185 m) subsea, respectively, consistent with the depth of Well-3c (Figure 4.14). Thus, we conclude the initial co-produced water originated from the Thirtyone reservoir. However, co-produced water temperature started to exceed this initial temperature soon after initial production, with a maximum measured temperature of 238°F (114°C) at the wellhead. From the regional and county-specific geothermal gradients, this maximum temperature corresponds to an aquifer depth of 15,450 ft (~4,710 m) and 16,130 ft (4,920 m) subsea, respectively. These depths correspond to the lower Simpson or uppermost Ellenburger (Figure 4.14). However, this water was likely sourced deeper than suggested by our temperature analysis due to cooling effects associated decompression and diffusion during open-hole production from the Well-3 lateral to the wellhead. This would place the water source fully within the Ellenberger Formation. Our basic temperature analysis – in addition to the intense water production observed throughout the history of Well-3c (Figure 4.10) – suggests there is an effective charge pathway between the Devonian and Ellenburger sections. Our geomechanical restorations define a vertically continuous zone of high strain adjacent to the well that we interpret to correspond to a potential charge pathways for water incursion (Figure 4.8, 4.13). The thrust ramp below the Central Saddle Anticline and within the Ellenberger Formation may also contribute to water charge pathways. In contrast, faulting and related folding within the Elsinore Anticline does not extend into the Ellenberger section. Thus, wells within the Elsinore structure – including Well-1 – generally have lower water cuts.

Conclusions

1. The prominent structural traps in the Oates SW Field, Pecos County, West Texas are characterized as basement-involved anticlinal fault-bend folds and fault-propagation folds. The Top Ellenburger serves as a regional detachment surface for these structures. Structural timing appears to be soon after Lower Pennsylvanian, and the fault-bend folds appear to have developed in a break-forward thrusting sequence.
2. The 3D geomechanical restoration tool used in this study accurately predicts strain patterns across the Lower Devonian Thirtyone reservoir in the Oates SW field. These geomechanical restorations accurately describe strain patterns over a range of scales, including trap-scale features as well as smaller, secondary faults and kink bands. It is especially encouraging that these subtle strains are predicted despite that secondary structures are not explicitly represented in the restoration models.
3. Model-II regressions validate strain-semblance correlations, and suggest that geophysical attributes and restoration strains can be used effectively to describe reservoir properties.
4. We document how strain predictions from our restoration tool accurately describe several production trends in the Oates SW field including variations in gas production, water cut, and reservoir fluid temperatures. This illustrates the ability of geomechanical restorations to accurately predict tectonic strains in deformed reservoirs, which can be used to drive development decisions and potentially inform operators of reservoir properties in advance of field development.

Care should be taken in the application of these methods to reservoir characterization studies, given the current limitations of the constitutive relations used by the restoration tool, and the uncertainties associated with defining the appropriate reservoir properties and boundary conditions. Nevertheless, this case study illustrates that by testing a range of material properties and geologically constrained boundary conditions, in addition to objective comparisons of restoration strains with independent strain attributes (e.g., geophysical attributes; well data), robust correlations between restoration strains and reservoir properties can be established. Such relationships provide a valuable tool that can help forecast reservoir properties in ways that help explain well performance and can be used in reservoir simulations to optimize field development.

Appendix A: Chapter 1 Supplemental Figures

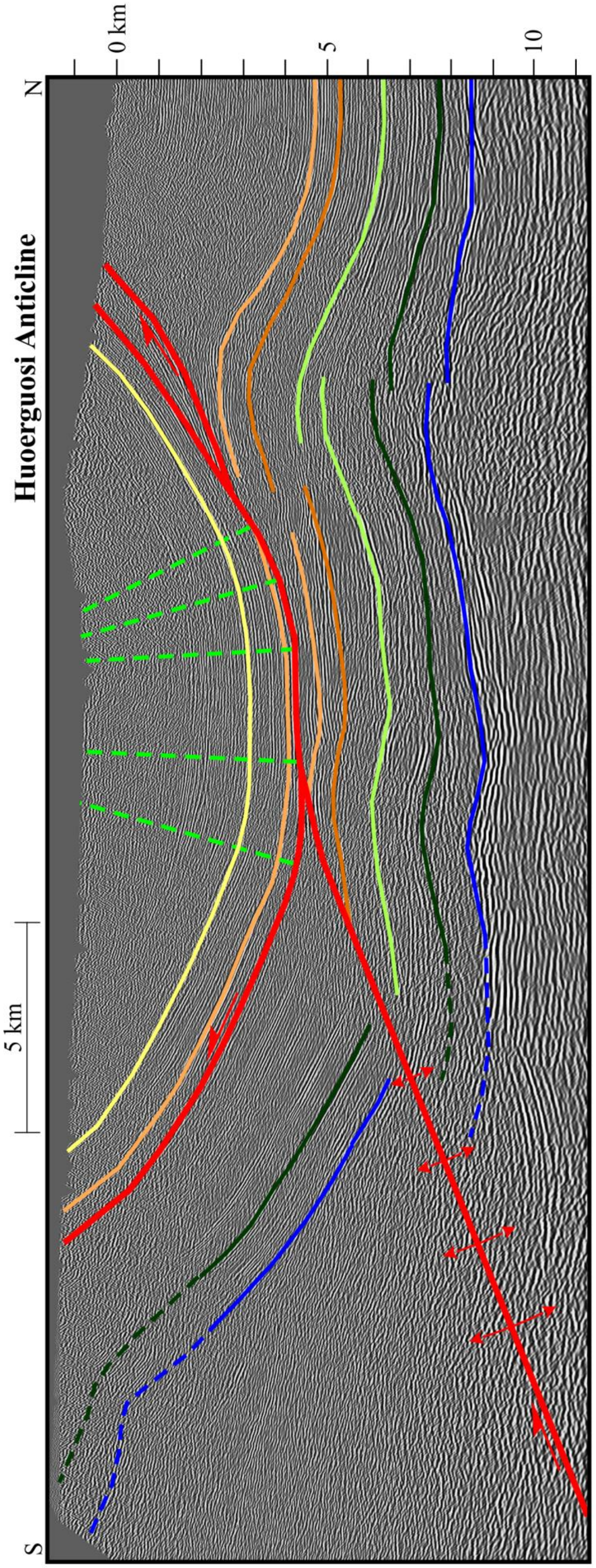

Supplemental Figure A1: Interpretation of the SJT across the Huoerguosi anticline and the northern Tian Shan rangefront.

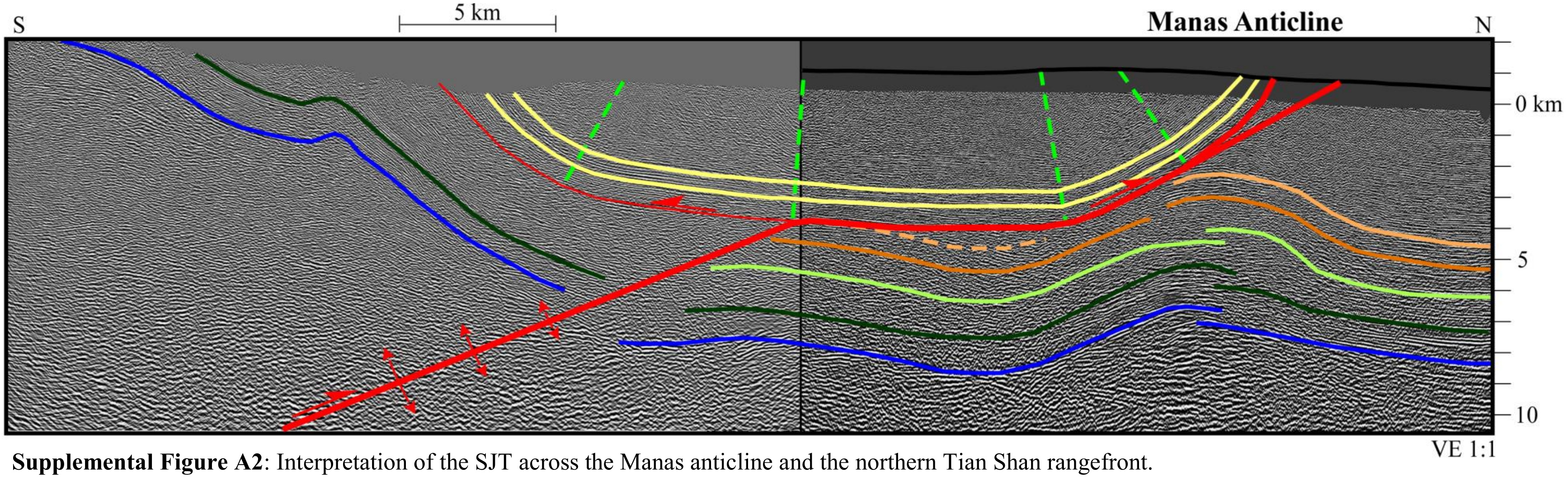

Supplemental Figure A2: Interpretation of the SJT across the Manas anticline and the northern Tian Shan rangefront.

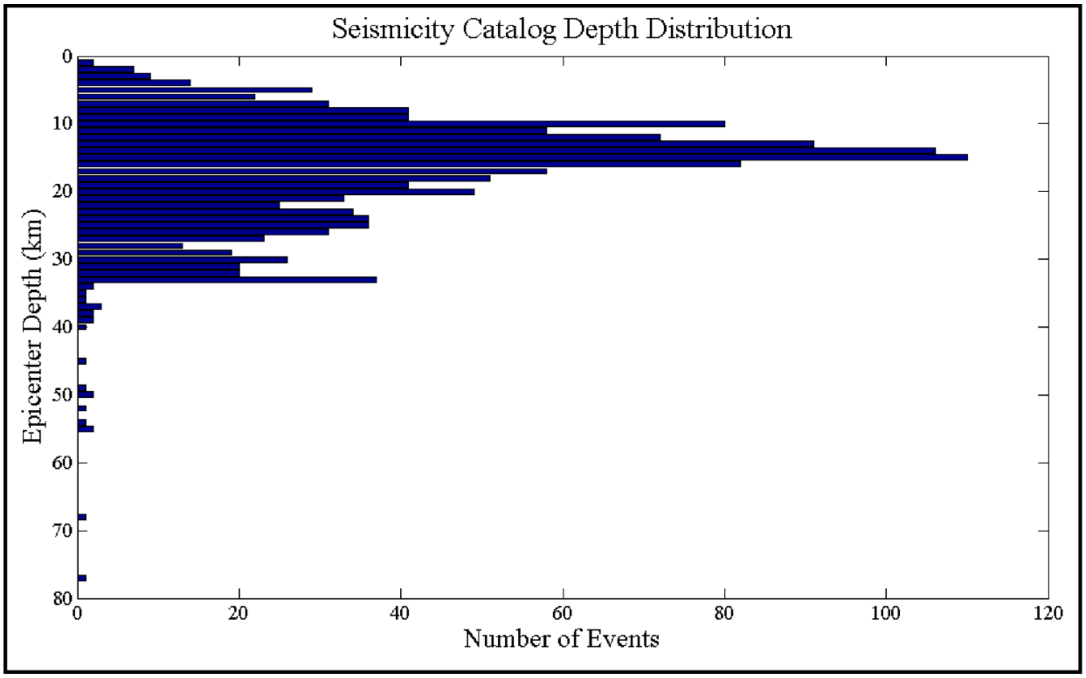

Supplemental Figure A3: Depth distribution of the seismicity catalog used to model the base of the seismogenic crust in Chapter 1.

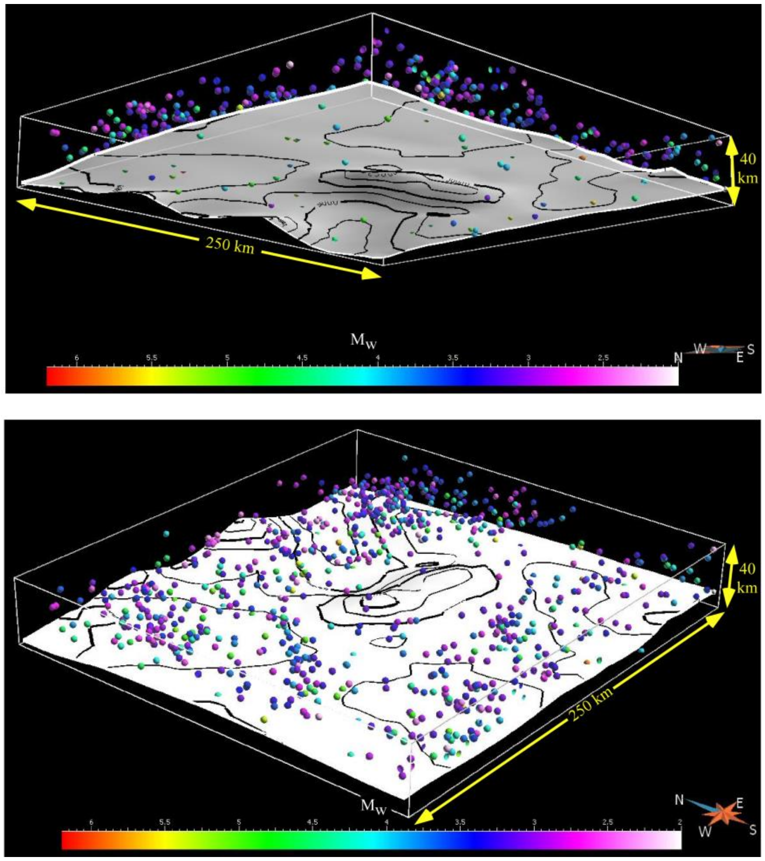

Supplemental Figure A4: Base of seismogenic crust and seismicity data from Chapter 1.

Appendix B: Evaluating Alternative SJT Kinematic Models

We present our preferred interpretation of the SJT fault bend from its Eocene detachment (θ_0=3.4°) to a steeper planar ramp dip (θ_2=27.4°) in Figure 2.5. In this interpretation, we follow classic fault-bend folding (Suppe, 1983; Medwedeff and Suppe, 1997) where folding occurs across an instantaneous change in fault dip and axial surfaces bisect the hanging wall syncline fold. An equally permissible interpretation allows for a curved-hinge fault bend fold (e.g. Suppe et al., 1997) that progressively increases the fault dip over a ~2,100 m zone of finite width. A third possibility is a listric fault-bend fold (Seeber and Sorlien, 2000; Amos et al., 2007). This possibility has important implications on the expected folding kinematics as listric fault-bend folds develop by limb rotation (Figure 2.2E) whereas either of the viable fault-bend fold models deform by kink-band migration (Figure 2.2A-B).

In listric fault-bend fold kinematic model (Seeber and Sorlien, 2000), entry and exit axial surfaces are oriented perpendicular to the entry (e.g. θ_0=3.4°) and exit (e.g. θ_2=27.4°) thrust fault dips. These axial surfaces meet at a point in the hanging wall of the thrust sheet, defining the origin and radius of a circle (Seeber and Sorlien, 2000). From our interpretation of the SJT and hanging wall fold, this solution defines a 4,500 m radius of curvature. The origin of the circle is located in the backlimb of the Tugulu fold, in the vicinity of where we have observed a distinct fanning of terrace fold dips (Figure 2.4B). However, the origin of the defined circle is ~1,200 m above sea level. The absolute elevations of these terraces south of the backlimb fold limb are ~1,000-1,100 m. Thus, terrace folding would be forced to occur over a very narrow horizontal distance. In this kinematic model, portions of terraces above the planar ramp beyond the region of fault curvature (θ_2), terraces would be rigidly uplifted and would not undergo folding by limb rotation (Seeber and Sorlien, 2000; Amos et al., 2007; Hu et al., 2015). In contrast, we observe

Quaternary terraces (T0-T3) folded across the entire extent of the θ_2 fault ramp. We note that the width of the T3 fold limb is ~1.8 km whereas the width of the T4 fold limb is ~900 m. Thus, in this interpretation, the T3 terrace would have experienced significantly more slip than T4 equating to ~1-2 orders of magnitude more fault slip than suggested by the structural relief (Table 2). Based on this analysis, we conclude that a listric fault-bend fold kinematic model (Seeber and Sorlien, 2000; Amos et al., 2007; Hu et al., 2015) is not consistent our integrated surface and subsurface data constraints. We note that in the absence of our subsurface data, the listric fault-bend fold model may be permissible because we would not have independent constraints on the width of the fault curvature (e.g. Amos et al., 2007; Hu et al., 2010). However, as we show with our mechanical model, fault-bend folding is consistent with both the surface and subsurface data constraints for this thrust sheet. This highlights the importance of subsurface data constraints to develop accurate kinematic models of fold growth; the occurrence of progressive limb rotation in growth strata or terrace folds may be consistent with a fault-bend fold solution (e.g. Dolan et al., 2003; Benesh et al., 2007; Leon et al., 2007; 2009).

Appendix C: Terrace Profile Extraction Procedure

Terrace Mapping

We mapped terraces across the Tugulu anticline along the Taxi He valley using the 1-m digital elevation model data set. For the young river terraces along the active stream channel, we mapped the top of terrace treads by extracting linear profiles along several transects of terrace segments. Only the T4 terrace was fully continuous across one side of the Taxi He (Figure 2.3), requiring the T5 and T6 terraces to involve profiles from both sides of the river valley. We assumed that a terrace tread directly across a river valley (perpendicular to the flow direction) within <70cm change in elevation was considered a terrace of equal age. We found the terraces interpreted for T5 and T6 had elevation changes that were negligible when compared to the natural variability of these terrace elevations (~35 cm). Interpretations of discontinuous Quaternary terraces (Figure 2.4C) required mapping of a loess cap contact with the fluvial deposits beneath, marking the top of the terrace tread. These features were readily identifiable in the field and DEM, facilitating relatively straightforward mapping procedures. However, given their discontinuous state, these features required iterative quality control both internally when mapping with the topographic data, as well as confirmation in the field. All terrace interpretations were quality controlled in the field, when possible, over three separate along the Taxi He valley from 2012-2014.

Correcting for Depositional Gradient

In order to quantify tectonic deformation, the original depositional gradient should be determined to properly assess uplift and fold dips. The raw terrace profiles for T4-T6 terraces to the south of any axial surfaces should represent their depositional gradient as there are no known structures that would have warped or folded these terraces immediately south of Tugulu (Figure

2.3C). Each of these terraces parallel the present-day Taxi He channel, indicating this river has maintained a relatively constant gradient since the deposition of T4. We remove this regional dip of 1.1° to reorient terrace elevations relative to the Taxi He. In this reference frame, any significant deviations from negligible dip may indicate structural relief due to fault slip on the SJT. The T0-T3 terraces are farther removed from the present-day Taxi He channel (Figure 2.3C) and mimic a paleo-trajectory significantly different than the Holocene Taxi He meandering. The azimuths of these terraces more closely resemble a dry stream bed – which we refer to as the Tugulu He – that is adjacent to these terraces, west of the Taxi He. T0 and T1 are not preserved outside of the Tugulu backlimb (Figure 2.3C). T2 and T3 can be mapped south of the fold over a reasonable distance to constrain their original depositional gradients. Both terraces have an undeformed dip of 1.3°, parallel to the gradient of the Tugulu He. Given the apparently long-term steady river gradients from the Taxi and Tugulu systems, we assume T1 and T0 have the same 1.3° undeformed gradient. We remove this gradient and produce residual terrace profiles relative to the Tugulu He for T0-T3 (Figure 2.6C). All subsequent structural analysis is conducted using these residual terrace profiles. We document our assessment of uncertainties related to the vertical position of terrace interpretations in Appendix C.

Appendix D: Uncertainties in Slip and Slip Rate Calculations

Fault Slip

We use structural relief measured in fluvial terrace profiles to quantify total fault slip along the SJT since the times of terrace abandonment. We apply a 1.2 m uncertainty for the all of the terrace elevation data associated with variations in the gravel veneer thickness and the resolution limits of the topographic dataset (70 cm). For Quaternary terraces, we add an additional ±1.5m uncertainty due to horizontal measurement error when interpreting terraces to account the potential for steep gradients (~35° in places) at loess-gravel contacts, along which these older terraces were mapped. These uncertainties encompass those related to selecting a single elevation to represent the position of a natural terrace tread (e.g. natural variations). Dip measurements along the SJT fault geometry were estimated to be ~1.5° by considering the range of hanging wall reflector and thrust dip orientations permissible while still producing a viable cross-section across the entire A-A' section that is consistent with fault-bend folding (Suppe, 1983).

Slip Rate

The mean values of the terrace data across the Tugulu anticline indicate a maximum slip rate of ~7.0 mm/yr at ~250 ka that has since decreased to a constant rate of ~1.3 mm/yr throughout the Holocene. We assess our conclusion of a decelerating SJT slip rate with a straightforward f-test simulation that considers terrace age uncertainties as well as fault slip uncertainties. For each simulation, fit two functions to these data: 1st- and 2nd-order polynomials that both run through the origin. For both functions we evaluate the model residuals:

$$\chi^2 = \sum_i \frac{r_i^2}{\sigma_i^2}$$

where r_i are the slip residuals and σ_1 are the 1-sigma slip uncertainties. When χ^2 for the 2nd-order polynomial fit is less than that for the 1st-order polynomial fit to the data, a decelerating slip rate is considered to have passed our f-test. We run 5000 simulations that randomly draw from the terrace age distributions and perform the f-test for each simulation. All 5000 2nd-order polynomial fits pass this f-test. Thus, a decelerating slip rate is a more robust description of our terrace data than a linear slip rate model to describe the same data.

We further evaluate how well the 2nd-order polynomials describe the terrace data relative to linear slip rate models by evaluating the modified Akaike Information Criterion (AICc):

$$AICc = 2k - 2\ln L + \frac{2k(k+1)}{n-k-1}$$

where k is the number of parameters in the model, L is the maximum of the likelihood function for the studied model and n is the sample size. AIC can be used to evaluate the amount of information lost by a describing a dataset. The modified form used here (AICc) incorporates a penalty to avoid over-fitting to small datasets. The 2nd-order polynomial functions systematically reduce the amount of lost information (lower AICc) relative to the constant slip rate functions (Supplemental Figure D1). This result indicates that the decreasing slip rate models described by the 2nd-order polynomial functions to the terrace data are consistently a better fit than a linear function to the same data (Supplemental Figure D1).

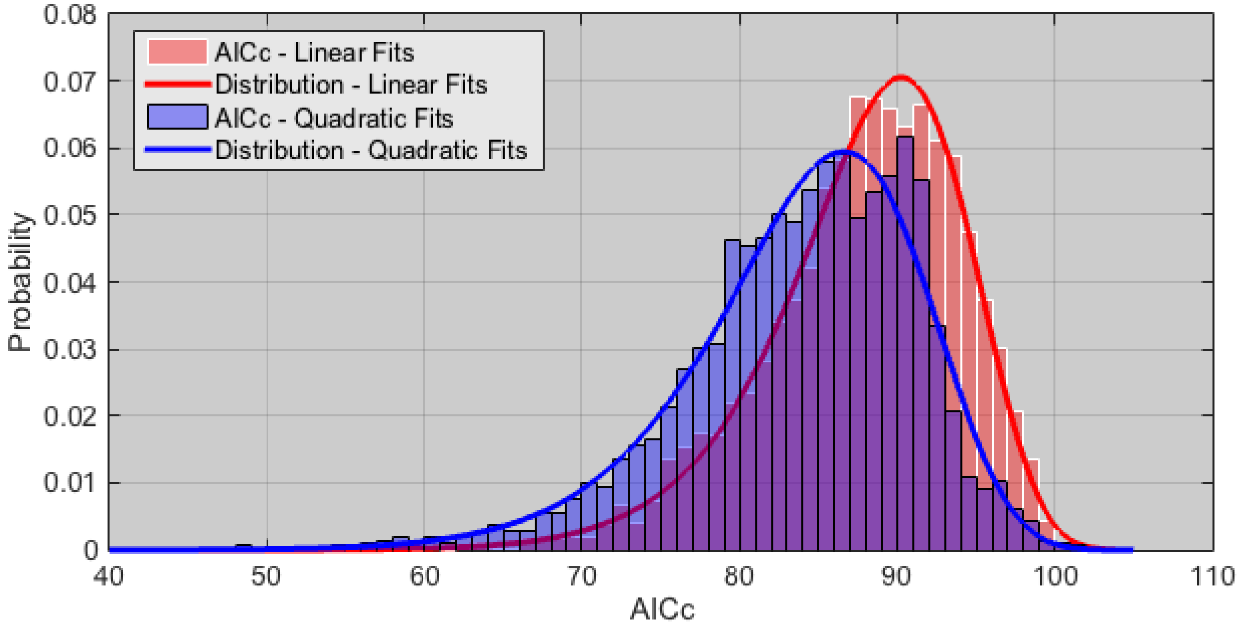

Supplemental Figure D1: AICc probability distributions from the simulations run to assess constant and decelerating slip rate models to describe the SJT terrace data. The 2nd-order polynomial fits systematically yield lower AICc magnitudes than the constant slip rate linear functions. This result suggests a decelerating slip rate more accurately describes the SJT terrace data, consistent with the f-test results.

Appendix E: Chapter 3 Supplemental Figures

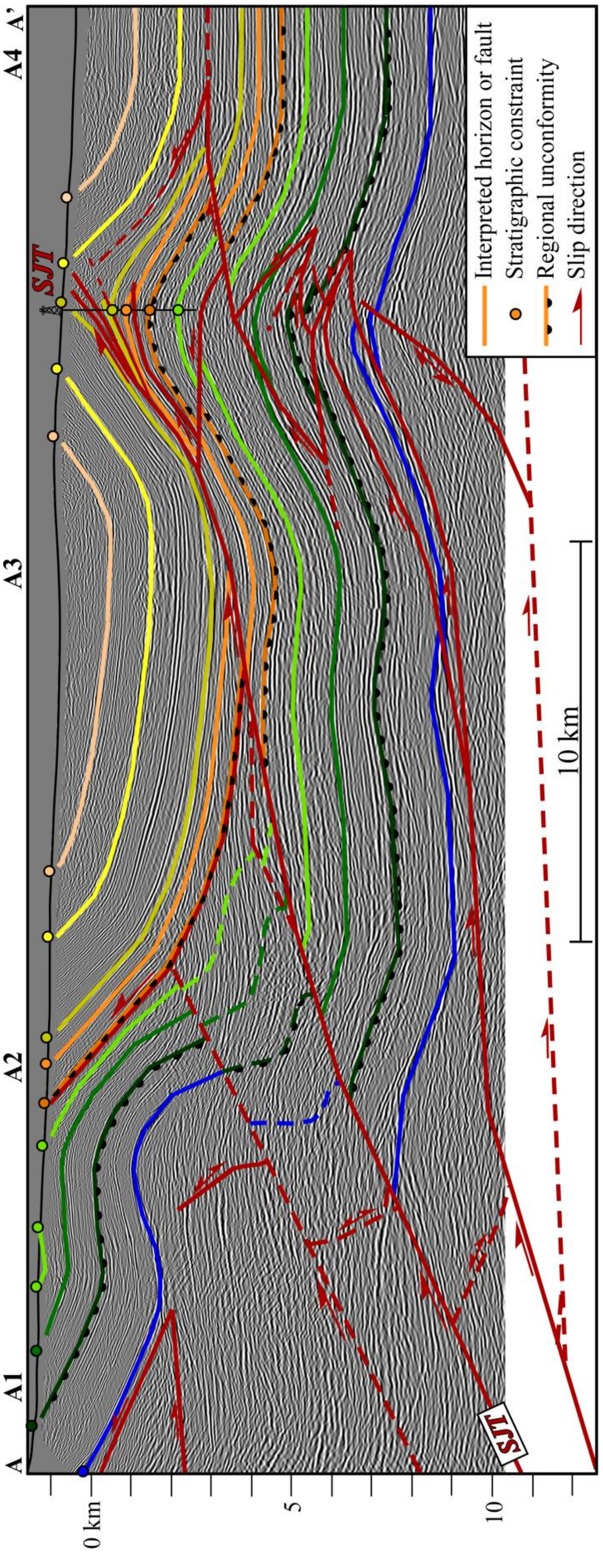

Supplemental Figure E1: Interpretation of Figure 3.4A. See Chapter 3 for details.

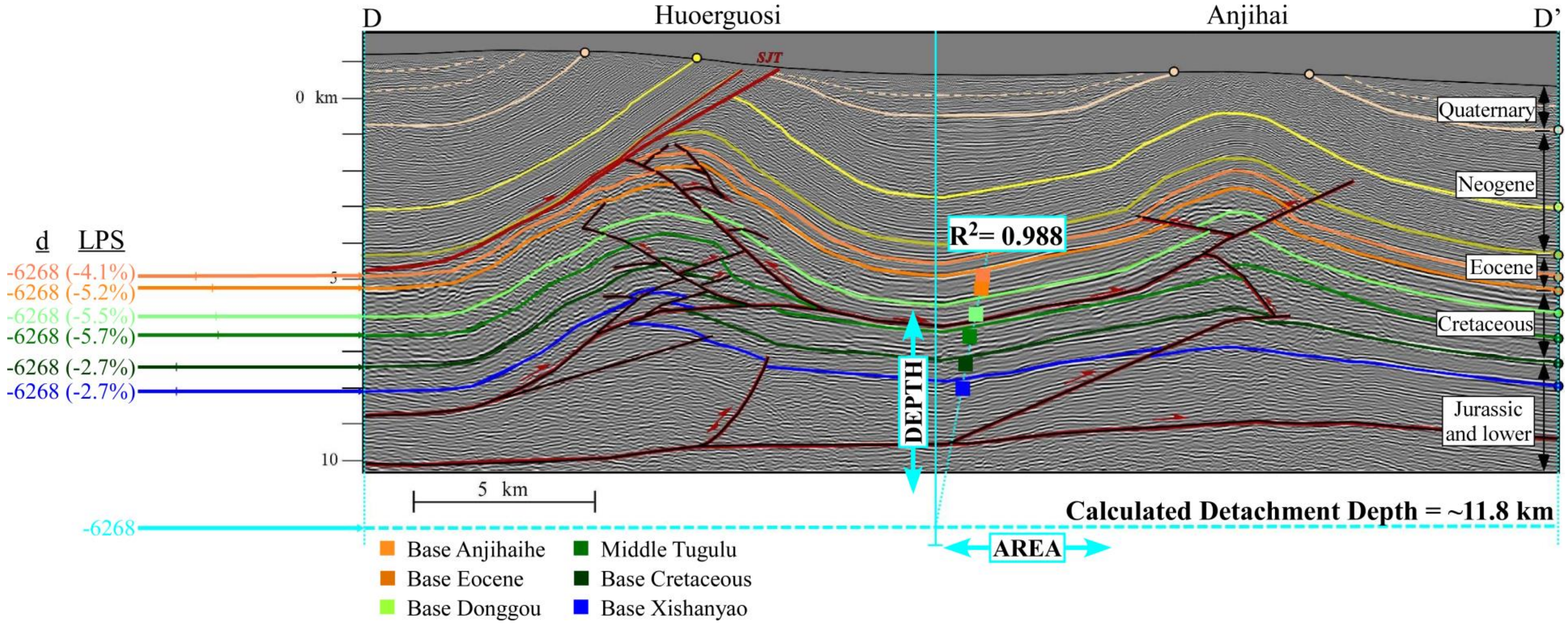

Supplemental Figure E2: Area-Depth plot generated in StructureSolver used to generate Figure 3.9B and 3.9C.

Appendix F: Fault Slip Constraints from Fold Limbs in Geomechanical Restoration Models

The 3-D seismic volume across Oates SW does not resolve any reflectors within the Ellenburger or older section that can be mapped across the field. Thus, we are unable to incorporate direct hanging wall and footwall cutoffs to serve as boundary conditions for the restoration models. Without these fault displacement constraints, the datum boundary condition and strain minimization technique of the geomechanical restoration tool generally produces a restored hanging wall that flattens in all directions. Clearly, such results are not physically reasonable.

To resolve this issue, we offset the down-dip boundary wall by the amount of slip that likely occurred along the thrust ramp to produce the observed anticlinal fault-bend fold. To do this, we first measure total slip on the upper detachment (S_1) from the width of the anticlinal forelimb fold (Suppe, 1983). We calculate this at all points along-strike from our 3-D structural model to obtain $S_1(x,y)$. Fault-bend folding theory predicts fault slip along the thrust ramp (S_0) to be consumed during anticlinal fold development when the angle between hanging wall strata and the thrust ramp (i.e. θ) is non-zero (Suppe, 1983). Thus, we infer that that $R(x,y)<1$, where $R=S_1/S_0$ (Suppe, 1983), for the interpreted fault-bend folds (Figure 5A). Following fault-bend fold theory, we use measures of fault and anticlinal fold geometries with measures of $S_1(x,y)$ to calculate $R(x,y)$ and, in turn, $S_0(x,y)$ for each fault-bend fold structural model. To implement this constraint in the restorations, we offset the down dip boundary wall by $S_0(x,y)$, (e.g., Figure 6B). This allows us to prescribe a fault offset boundary condition, even in the absence of cutoffs, and obtain a geologically reasonable restoration result.

Appendix G: Strain Tensor Invariants

Gradients in the restoration velocity field of each restoration yield the full strain tensor at all nodes of restoration models:

$$\begin{bmatrix} \varepsilon_{11} & \varepsilon_{12} & \varepsilon_{13} \\ \varepsilon_{12} & \varepsilon_{22} & \varepsilon_{23} \\ \varepsilon_{13} & \varepsilon_{23} & \varepsilon_{33} \end{bmatrix}$$

We express each tensor solely as a function of its eigenvalues (ε_i), avoiding off-diagonal components of the strain tensor:

$$\begin{bmatrix} \varepsilon_1 & 0 & 0 \\ 0 & \varepsilon_2 & 0 \\ 0 & 0 & \varepsilon_3 \end{bmatrix}$$

From this, we calculate the first invariant of the strain tensor (I_1) – dilation – at all nodes of a restoration model:

$$I_1 = \varepsilon_1 + \varepsilon_2 + \varepsilon_3$$

To calculate the second invariant of the strain tensor (I_2) – distortion – we first generate the deviatoric strain tensor by subtracting the mean strain (ε_m) from the diagonal components of the strain tensor:

$$\begin{bmatrix} \varepsilon_1 - \varepsilon_m & 0 & 0 \\ 0 & \varepsilon_2 - \varepsilon_m & 0 \\ 0 & 0 & \varepsilon_3 - \varepsilon_m \end{bmatrix}$$

where,

$$\varepsilon_m = (\varepsilon_1 + \varepsilon_2 + \varepsilon_3)/3$$

From this expression, we calculate I_2 at every node of a restoration model:

$$I_2 = (\varepsilon_1 - \varepsilon_m)(\varepsilon_2 - \varepsilon_m) + (\varepsilon_1 - \varepsilon_m)(\varepsilon_3 - \varepsilon_m) + (\varepsilon_2 - \varepsilon_m)(\varepsilon_3 - \varepsilon_m)$$

We are able to discriminate between volume increases or decreases (e.g., Figure 1D) and, similarly, the relative orientations of distortion using the signs of calculated strain invariants. The signs of strain are particularly helpful where we attempt to validate a restoration result (see section 4c). However, as we generate linear regressions between strain, a signed attribute, and semblance, a parameter defined between zero and one, we use the absolute values of strain for our correlation analysis in Section 5 (Figure 9).

References

Abdrakhmatov, K. Y., S. A. Aldazhanov, B.H. Hager, M. W. Hamburger, T. A. Herring, K. B. Kalabaev, V. I. Makarov, P. Molnar, S. V. Panasyuk, M. T. Prilepin, R. E. Reilinger, I. S. Sadybakasov, B. J. Souter, Y. A. Trapeznikov, V. Y. Tsurkov, A. V. Zubovich, 1996, Relatively recent construction of the Tien Shan inferred from GPS measurements of present-day crustal deformation rates: Nature, v. 384, p. 450-453.

Allen, M. B., A. M. C. Şengör and B. A. Natal'in, 1995, Junggar, Turfan and Alakol basins as late Permian to ?early Triassic extensional structures in a sinistral shear zone in the Altaid orogenic collage, central Asia: Journal of the Geological Society of London, v. 152, p. 327-338.

Allen, M. B., B. F. Windley, and C. Zhang, 1992, Paleozoic collisional tectonics and magmatism of the Chinese Tien Shan, central Asia: Tectonophysics, v. 220, p. 89-115.

Allen, M. B., B. F. Windley, C. Zhang, C., and J. H. Guo, 1993, Evolution of the Turfan Basin, Chinese Central Asia: Tectonics, v. 12, p. 889-896.

Allmendinger, R. W., 1998, Inverse and Forward numerical modeling of trishear fault-propagation folds: Tectonics, v. 17, p. 640–656.

Amos, C. B., D. W. Burbank, D. C. Nobes, and S. A. L. Read, 2007, Geomorphic constraints on listric faulting: implications for active deformation in the Mackenzie Basin, South Island, New Zealand: Journal of Geophysical Research, v. 112, B03S11.

Avouac, J. P., P. Tapponnier, M. Bai, H. You, G. Wang, 1993, Active thrusting and folding along the northern Tien Shan and late Cenozoic rotation of the Tarim relative to Dzungaria and Kazakhstan: Journal of Geophysical Research, v. 98(B4), p. 6755-6804.

Aydin, A., 2000, Fractures, faults, and hydrocarbon entrapment, migration and flow: Marine and Petroleum Geology, v. 17(7), p. 797-814.

Bahorich, M. and S. Farmer, 1995, 3-D seismic discontinuity for faults and stratigraphic features: The coherence cube: The Leading Edge, v. 14(10), p.1053-1058.

Bally, A. W., 1984, Tectogenèse et sismique réflexion: Bulletin de la Societe Gèologique de France, v. 2, p. 279–285.

Bellahsen, N., P. E. Fiore, and D. D. Pollard, 2006, From spatial variation of fracture patterns to fold kinematics: a geomechanical approach: Geophysical Research Letters, v. 33(2), L02301.

Benesh, N. P., 2010, The mechanics of fault-bend folding and tear-fault systems in the Niger Delta: Ph.D. Dissertation, Harvard University, Cambridge, Massachusetts, 109 p.

Benesh, N. P., A. Plesch and J. H. Shaw, 2014, Geometry, kinematics, and displacement characteristics of tear-fault systems: an example from the deep-water Niger Delta: AAPG Bulletin, v. 98(3), p. 465-482.

Benesh, N. P., A. Plesch, J. H. Shaw, and E. K. Frost, 2007, Investigation of growth fault bend folding using discrete element modeling: Implications for signatures of active folding above blind thrust faults: Journal of Geophysical Research: Solid Earth, v. 112(B3).

Billingsley, L., 2006, Exploiting the Devonian Reservoir in Oates SW Area, Western Delaware Basin, Texas: Houston Geological Society Bulletin, v. 49(4), p.41 (abs.).

Bowker, K. A., 2007, Barnett Shale gas production, Fort Worth Basin: issues and discussion: AAPG bulletin, v. 91(4), p. 523-533.

Brandenburg, J. P., 2013. Trishear for curved faults: Journal of Structural Geology, v. 53, p. 80-94.

Brown, N. D., E. J. Rhodes, J. L. Antinao, and E. V. McDonald, 2015, Single-grain post-IR IRSL signals of K-feldspars from alluvial fan deposits in Baja California Sur, Mexico: Quaternary International, v. 362, p.132-138.

Burchfiel, B. C., E. T. Brown, Q. Deng, X. Feng, J. Li, P. Molnar, J. Shi, Z. Wu, and H. You, 1999, Crustal shortening on the margins of the Tien Shan, Xinjiang, China: International Geology Review, v. 41, p. 665-700.

Carena, S., J. Suppe, and H. Kao (2004), Lack of continuity of the San Andreas Fault in southern California: three-dimensional fault models and earthquake scenarios: Jounal of Geophysical Research, v. 109, B04313, doi:10.1029/2003JB002643.

Carroll, A. R., S. C. Brassell, and S. A. Graham, 1992, Upper Permian lacustrine oil shales, southern Junggar basin, northwest China: AAPG Bulletin, v. 76, p. 1874-1902.

Charreau, J., J. P. Avouac, Y. Chen, S. Dominguez and S. Gilder, 2008, Miocene to present kinematics of fault-bend folding across the Huerguosi anticline, northern Tianshan (China), derived from structural, seismic, and magnetostratigraphic data: Geology, v. 36, p. 871-874.

Charreau, J., Y. Chen, S. Gilder, L. Barrier, S. Dominguez, R. Augier, S. Sevket, J. P. Avouac, A. Gallaud, F. Graveleau, and Q. Wang, 2009, Neogene uplift of the Tian Shan Mountains observed in the magnetic record of the Jingou River section (northwest China): Tectonics, v. 28, TC2008, doi:10.1029/2007TC002137.

Chauvin, B., A. Mazuyer and G. Caumon, 2015, Mechanics-based restoration: a physical and mathematical review: in Proceedings of the 35th Gocad Meeting – 2015 RING Meeting: Nancy, France, Association Scientifique pour la Geologie et ses Applications 34 pp.

Chen, K., C. Gumiaux, R. Auglier, Y. Chen, Q. Qang, W. Lin and S. Wang, 2011, The Mesozoic paleorelief of the northern Tian Shan (China): Terra Nova, v. 23, p. 195-205.

Chen, Y. G., Lai, K.-Y., Lee, Y.-H., Suppe, J., Chen, W.-S., Lin, Y.-N. N., Wang, Y., Hung, J.-H., Kuo, Y.-T., 2007, Coseismic fold scarps and their kinematic behavior in the 1999 Chi-Chi earthquake Taiwan: Journal of Geophysical Research, v. 112, B03S02.

Chopra, S. and K. J. Marfurt, 2010, Integration of coherence and volumetric curvature images: The Leading Edge, v. 29(9), p. 1092-1107.

Clayton, J. L., J. Yang, J. D. King, P. G. Lillis, A. Warden, 1997, Geochemistry of oils from the Junggar Basin, Northwest China: AAPG Bulletin, v. 81 , p. 1926-1944.

Cook, K. L., J. M. Turowski, and N. Hovius, 2014, River gorge eradication by downstream sweep erosion. Nature Geoscience, v. 7(9), p.682-686.

Cooke, M. L. and D. D. Pollard, 1997, Bedding-plane slip in initial stages of fault-related folding: Journal of Structural Geology, v. 19(3), p. 567-581.

Cristallini, E. O. and R. W. Allmendinger, 2002, Backlimb trishear: a kinematic model for curved folds developed over angular fault bends. Journal of Structural Geology, v. 24(2), p.289-295.

Cundall, P. A. and Strack, O. D., 1979, A discrete numerical model for granular assemblies: Geotechnique, v. 29(1), p.47-65.

Daëron, M., J. P. Avouac, J. Charreau, and S. Dominguez, 2007, Modeling the shortening history of a fault-tip fold using structural and geomorphic records of deformation: Journal of Geophysical Research, v. 12, B03S13.

Dahlstrom, C. D., 1969, Balanced cross sections: Canadian Journal of Earth Sciences, v. 6, p. 743-757.

Dahlstrom, C. D., 1970, Structural geology in the eastern margin of the Canadian Rocky Mountains: Bulletin of Canadian Petroleum Geology, v. 18(3), pp.332-406.

De Grave, J., M. M. Buslov and P. Van den haute, 2007, Distant effects of India-Eurasia convergence and Mesozoic intracontinental deformation in Central Asia: Constraints from apatite fission-track thermochronology: Journal of Asian Earth Sciences, v. 29, p. 188-204.

Deng, Q., P. Zhang, X. Xu, X. Yang, and S. Peng, 1996, Paleoseismology of the northern piedmont of Tianshan Mountains, northwest China: Journal of Geophysical Research, v. 101, p. 5895-5920.

Deng, Q., X. Y. Feng, P. Z. Zhang, X. W. Xu, X. P. Yang, S. Z. Peng, and J. Li, 2000, Active tectonics of the Tian Shan Mountains: Seismology Press, Beijing, 399 pp. (in Chinese).

Dickinson W. R. and W. S. Snyder, 1978, Plate tectonics of the Laramide orogeny, in Laramide Folding Associated with Basement Block Faulting in the Western United States, ed. V. Matthews III: Geological Society of America Memoir 151, p. 355-366, Boulder, CO.

Ding, A. N., R. Y. Hui, Z. N. Zhang, 2003, Hydrocarbon potential of Jurassic source rocks in the Junggar basin, NW China: Journal of Petroleum Geology, v. 26, p. 1747-5457.

Dolan, J. F., S. Christofferson, J. H. Shaw, 2003, Recognition of paleoearthquakes on the Puente Hills blind thrust fault, Los Angeles, California: Science, v. 300, p. 115-118.

Durand-Riard, P., G. Caumon and P. Muron, 2010, Balanced restoration of geological volumes with relaxed meshing constraints: Computers & Geosciences, v. 36(4), p. 441–542.

Durand-Riard, P., J. H. Shaw, A. Plesch and G. Lufadeju, G, 2013, Enabling 3D geomechanical restoration of strike-and oblique-slip faults using geological constraints, with applications to the deep-water Niger Delta: Journal of Structural Geology, 48, p. 33-44.

Durand-Riard, P., L. Salles, M. Ford, G. Caumon and J. Pellerin, 2011, Understanding the evolution of syn-depositional folds: coupling decompaction and 3D sequential restoration: Marine and Petroleum Geology, v. 28(8), p. 1530–1539

Egan, S. S., S. Kane, T. S. Buddin, G. D. Williams and D. Hodgetts, 1999, Computer modelling and visualisation of the structural deformation caused by movement along geological faults: Computers & Geosciences, v. 25(3), p. 283-297.

Eichelberger, N. W., A. N. Hughes, and A. G. Nunns, 2015, Combining multiple quantitative structural analysis techniques to create robust structural interpretations: Interpretation, v. 3, no. 4, SAA89-SAA104.

Engelder, T., G. G. Lash, and R. S. Uzcátegui, 2009, Joint sets that enhance production from Middle and Upper Devonian gas shales of the Appalachian Basin: AAPG Bulletin, v. 93(7), p. 857-889.

English, J. M., G. A. Lunn, L. Ferreira, and G. Yacu, 2015, Geologic evolution of the Iraqi Zagros, and its influence on the distribution of hydrocarbons in the Kurdistan region: AAPG Bulletin, v. 99, no. 2, p. 231-272.

Epard, J. L. and R. H. Groshong, 1993, Excess area and depth to detachment: AAPG Bulletin, v. 77, no. 8, p. 1291-1302.

Erdlac, Jr., R. J., 2006, A resource assessment of geothermal energy resources for converting deep gas wells in carbonate strata into geothermal extraction wells: a Permian Basin evaluation (Year 1 progress report): The University of Texas of the Permian Basin Center for Energy and Economic Diversification, DOE #DE-FG36-05GO85023, 113 pp. + 69 e-files.

Erickson, S. G. and W. R. Jamison, 1995, Viscous-plastic finite-element models of fault-bend folds: Journal of Structural Geology, v. 17(4), p. 561-573.

Erickson, S. G., 1996, Influence of mechanical stratigraphy on folding vs faulting: Journal of Structural Geology, v. 18(4), p. 443-450.

Erslev, E. A., 1991, Trishear fault propagation folding: Geology, v. 19, p. 617-620.

Fan, G., Z. Li, D. Yang W. Wang, 2012, Structural Evolution Research of Qigu Fault-folded Belts: Journal of Southwest Petroleum University, v. 34, p. 9-18.

Fischer, M. P. and J. B. Jackson, 1999, Stratigraphic controls on deformation patterns in fault-related folds: a detachment fold example from the Sierra Madre Oriental, northeast Mexico: Journal of Structural Geology, v. 21(6), p. 613-633.

Frankowicz, E. and K. R. McClay, 2010, Extensional fault segmentation and linkages, Bonaparte Basin, outer North west shelf, Australia: AAPG Bulletin, v. 94(7), p. 977-1010.

Frenzel, H. N., et al., 1988, The Permian basin region, in the geology of North America, sedimentary cover--North American craton: Geological Society of America, v. D-2, p. 261-306.

Fu, B., A. Lin, K. I. Kano, T. Maruyama and J. Guo, 2003 Quaternary folding of the eastern Tian Shan, northwest China: Tectonophysics, v. 369, no. 1, p. 79-101.

Galbraith, R. F., R. G. Roberts, G. M. Laslett, H. Yoshida, and J. M. Olley, 1999, Optical dating of single and multiple grains of quartz from jinmium rock shelter, northern australia: part i, experimental design and statistical models: Archaeometry, v. 41(2), p. 339-364.

Gale, J. F., R. H. Lander, R. M. Reed, and S. E. Laubach, 2010, Modeling fracture porosity evolution in dolostone: Journal of Structural Geology, v. 32(9), p.1201-1211.

Gale, J. F., S. E. Laubach, J. E. Olson, P. Eichhubl and A. Fall, 2014, Natural fractures in shale: a review and new observations: AAPG Bulletin, v. 98(11), p. 2165-2216.

Gao, J., M. Li, X. Xiao, Y. Tang, and G. He, 1998, Paleozoic tectonic evolution of the Tianshan Orogen, northwestern China: Tectonophysics, v. 287, p. 213-231.

Ghosh, K. and S. Mitra, 2009, Two-dimensional simulation of controls of fracture parameters on fracture connectivity: AAPG Bulletin, v. 93(11), p. 1517-1533.

Gibbs, A. D., 1984, Structural evolution of extensional basin margins: Journal of the Geological Society, v. 141, no.4, p. 609-620.

Glennie, K. W., and P. L. Boegner, 1981, Sole pit inversion tectonics, in L. V. Illing and G. D. Hobson, eds., Petroleum geology of the continental shelf of northwest Europe: London, Institute of Petroleum, p. 110–120.

Glorie, S., J. De Grave, M. M. Buslov, F. I. Zhimulev, D. F. Stockli, V. Y. Batalev, A. Izmer, P. Van den haute, F. Vanhaecke and M. A. Elburg, 2011, Tectonic history of the Kyrgyz south Tien Shan (Atbashi-Inylchek) suture zone: the role of inherited structures during deformation-propagation: Tectonics, v. 30, TC6016.

Gold, R. D., E. Cowgill, E., X. F. Wang, and X. H. Chen, 2006, Application of trishear fault-propagation folding to active reverse faults: examples from the Dalong Fault, Gansu Province, NW China: Journal of Structural Geology, v. 28(2), pp.200-219.

Gong, Z., Li, S. H., & Li, B., 2014, The evolution of a terrace sequence along the Manas River in the northern foreland basin of Tian Shan, China, as inferred from optical dating: Geomorphology, v. 213, p. 201-212.

Gonzalez-Mieres, R., and J. Suppe, 2006, Relief and shortening in detachment folds: Journal of Structural Geology, v. 28, no.10, p. 1785-1807.

Graham, S. A., M. S. Hendrix, C. L. Johnson, D. Badamgarav, G. Badarch, J. Amory, M. Porter, R. Barsbold, L. E. Webb, and B. R. Hacker, 2001, Sedimentary record and tectonic implications of Mesozoic rifting in southeast Mongolia: Geological Society of America Bulletin, v. 113, no.12, p. 1560-1579.

Graham, S. A., T. Cope, C. L. Johnson and B. Ritts, 2012, Sedimentary basins of the late Mesozoic extensional domain of China and Mongolia, in D.G. Roberts and A.W. Bally eds., Regional geology and tectonics: phanerozoic rift systems and sedimentary basins: Elsevier, Amsterdam, p. 443–461.

Griffiths, P., S. Jones, N. Salter, F. Schaefer, R. Osfield, and H. Reiser, 2002, A new technique for 3-D flexural-slip restoration: Journal of Structural Geology, v. 24(4), p. 773-782.

Groshong, R. H., 1990, Unique determination of normal-fault shape from hanging-wall bed geometry in detached half grabens: Eclogae Geologicae Helvetiae, v. 83, p. 455-471.

Groshong, R. H., 2015, Quality control and risk assessment of seismic profiles using area-depth-strain analysis: Interpretation, v. 3, no. 4, SAA1-SAA15.

Groshong, R. H., M. O. Withjack, R. W. Schlische and T. N. Hidayah, 2012, Bed length does not remain constant during deformation: recognition and why it matters, Journal of Structural Geology, v. 41, p. 86-97.

Guzofski, C., J. H. Shaw, G. Lin, and P. M. Shearer, 2007, Seismically active wedge structure beneath the Coalinga anticline, San Joaquin basin, California: Journal of Geophysical Research, v. 112, B03S05.

Guzofski, C., J. Müeller, J. H. Shaw, P. Muron, D. Medwedeff, F. Bilotti and C. Rivero, 2009, Insights into the mechanisms of fault-related folding provided by volumetric structural restorations using spatially varying mechanical constraints: AAPG Bulletin, v. 93(4), p. 479–502.

Hamblin, W. K., 1965, Origin of “reverse drag” on the downthrown side of normal faults: Geological Society of America Bulletin, v. 76, p. 1145–1164.

Hanks, T. C., and W. H. Bakun, 2002, A bilinear source-scaling model for M-log A observations of continental earthquakes: BSSA, v. 92, 1841-1846.

Hardy, S. and C. D. Connors, 2006, Short note: a velocity description of shear fault-bend folding: Journal of Structural Geology, v. 28, no. 3, p. 536-543.

Hardy, S. and Poblet, J., 1994, Geometric and numerical model of progressive limb rotation in detachment folds: Geology, v. 22(4), p. 371-374.

Harris, R. A., and S. M. Day, 1999, Dynamics of fault interaction: parallel strike-slip faults: Journal of Geophysical Research, v. 98, 4461-4472.

Hendrix, M. S., S. C. Brassell, A. R. Carroll, S. A. Graham, 1995, Sedimentology, organic geochemistry, and petroleum potential of Jurassic coal measures; Tarim, Junggar, and Turpan basins, northwest China: AAPG Bulletin, v. 79, p. 929-959.

Hendrix, M. S., T. A. Dumitru, and S. A. Graham, 1994, Late Oligocene-early Miocene unroofing in the Chinese Tian Shan: An early effect of the India-Asia collision: Geology, v. 22, 487-490.

Hendrix, M.S., S. A. Graham, A. R. Carroll, E. R. Sobel, C. L. McKnight, B. J. Schulein, Z. Wang, 1992, Sedimentary record and climatic implications of recurrent deformation in the Tien Shan: evidence from the Mesozoic strata of the north Tarim, south Junggar, and Turpan basins, northwest China: Geological Society of America Bulletin, v. 104, p. 53–79.

Hennings, P. H., J. E. Olson and L. B. Thompson, 2000, Combining outcrop data and three-dimensional structural models to characterize fractured reservoirs: an example from Wyoming: AAPG Bulletin, v. 84(6), p. 830-849.

Hills, J. M., 1985, Structural evolution of the Permian basin of west Texas and New Mexico: Structure and Tectonics of Trans-Pecos Texas, West Texas Geological Society Publication, v. 85-81, p. 89-99.

Hu, X., B. Pan, E. Kirby, H. Gao, Z. Hu, B. Cao, H. Geng, Q. Li, and G. Zhang, 2015, Rates and kinematics of active shortening along the eastern Qilian Shan, China, inferred from deformed fluvial terraces: Tectonics, v. 34(12), p. 2478-2493.

Hubbard, J., and J. H. Shaw, 2009, Uplift of the Longmen Shan and Tibetan plateau, and the 2008 Wenchuan (M=7.9) earthquake, Nature, v. 458, 194-197, doi:10.1038/nature07837.

Hubbard, J., J. H. Shaw, and Y. Klinger, 2010, Structural setting of the 2008 Mw 7.9 Wenchuan, China earthquake, BSSA, v. 100, p. 2713-2735, doi:10.1785/0120090341.

Hubert-Ferrari, A., J. Suppe, R. Gonzalez-Mieres, X. Wang, 2007, Mechanisms of active folding of the landscape (southern Tian Shan, China): Journal of Geophysical Research, v. 112, B03S09

Hughes, A. N. and J. H. Shaw, 2014, Fault displacement-distance relationships as indicators of contractional fault-related folding style: AAPG Bulletin, v. 98(2), p.227-251.

Hughes, A. N., N. P. Benesh, and J. H. Shaw, 2014, Factors that control the development of fault-bend versus fault-propagation folds: insights from mechanical models based on the discrete element method (DEM): Journal of Structural Geology, v. 68, p. 121-141.

Hughes, A.N. and J. H. Shaw, 2015, Insights into the mechanics of fault-propagation folding styles: Geological Society of America Bulletin, v. 127(11-12), p.1752-1765.

Ishiyama, T., K. Mueller, H. Sato, and M. Togo, 2007, Coseismic fault-related fold model, growth structure, and the historic multisegment blind thrust earthquake on the basement involved Yoro thrust, central Japan: Journal of Geophysical Research, v. 112(B3), 22 pp.

Jia, C., 2012, Characteristics of Chinese Petroleum Geology: Springer Berlin Heidelberg, 599 p.

Johnson, C. L., K. C. Constenius, S. A. Graham, G. Mackey, T. Menotti, A. Payton, and J. Tully, 2015, Subsurface evidence for late Mesozoic extension in western Mongolia: tectonic and petroleum systems implications: Basin Research, v. 27, no. 3, p. 272-294.

Johnson, K. N. and Finnegan, N. J., 2015. A lithologic control on active meandering in bedrock channels. Geological Society of America Bulletin, v. 127(11-12), pp.1766-1776.

Jolivet, M., S. Dominguez, J. Charreau, Y. Chen, Y. Li and Q. Wang, 2010, Mesozoic and Cenozoic tectonic history of the central Chinese Tian Shan: reactivated tectonic structures and active deformation: Tectonics, v. 29, TC6019.

Laubach, S. E., J. E. Olson, and M. R. Gross, 2009, Mechanical and fracture stratigraphy: AAPG Bulletin, v. 93(11), p.1413-1426.

Lavé, J., and J. P. Avouac, 2000, Active folding of fluvial terraces across the Siwaliks Hills, Himalayas of central Nepal: Journal of Geophysical Research, v. 105(B3), p. 5735-5770.

Le Béon, M., J. Suppe, M. K. Jaiswal, Y. G. Chen and M. E. Ustaszewski, 2014, Deciphering cumulative fault slip vectors from fold scarps: Relationships between long-term and coseismic deformations in central Western Taiwan: Journal of Geophysical Research: Solid Earth, v. 119(7), p.5943-5978.

Leon, L. A., J. F. Dolan, J. H. Shaw, and T. L. Pratt, 2009, Evidence for large Holocene earthquakes on the Compton thrust fault, Los Angeles, California: Journal of Geophysical Research: Solid Earth, v. 114(B12).

Leon, L. A., S. A. Christofferson, J. F. Dolan, J. H. Shaw, and T. L. Pratt, 2007, Earthquake-by-earthquake fold growth above the Puente Hills blind thrust fault, Los Angeles, California: implications for fold kinematics and seismic hazard: Journal of Geophysical Research: Solid Earth, v. 112(B3).

Leonard, M., 2010, Earthquake fault scaling: self-consistent relating of rupture length, width, average displacement, and moment release, BSSA, 100, p. 1971-1988, doi:10.1785/0120090189.

Li, B., S. Guan, Z. Chen, D. He, J.H. Shaw, Y. Lei, X. Shi, and C. Zhang, 2010a, Fault-related fold theory and application: Case study on structural geology in southern Junggar basin, Petroleum Industry Press, Beijing, China (in Chinese).

Li, Y., D. Jia, J.H. Shaw, J. Hubbard, A. Lin, M. Wang, L. Luo, H. Li, and L. Wu, 2010b, Structural interpretation of the coseismic faults of the Wenchuan earthquake: Three-dimensional modeling of the Longmen Shan fold-and-thrust belt, J. Geophys. Res., 115, B04317, doi:10.1029/2009JB006824.

Li, Z., S. Zhang and G. Chen, 1998, Discussion on the extensional dynamic setting in the south border of Junggar basin, Xinjiang, China: Geological Journal of China Universities v. 4, no.1, p. 73–78 (in Chinese with English abstract).

Liu, H. F., Z. C. Wang, B. X. Xiong, Y. L. Li, L. Q. Liu, and J. Z. Zhang, 2000, Coupling analysis of Mesozoic-Cenozoic foreland basin and mountain system in central and western China. Earth Science Frontiers, v. 7, no. 3, p. 55–72 (in Chinese with English abstract)

Lorenz J. C. and S. J. Finley, 1989, Differences in fracture characteristics and related production: Mesaverde Formation, Northwestern Colorado: SPE Formation Evaluation, v. 4(1), p. 11-16.

Loucks, R. G., 2008, Review of the lower Ordovician Ellenburger group of the Permian basin, West Texas, http://www.beg.utexas.edu/resprog/permianbasin/PBGSP_members/writ_synth/Ellenburger%20report.pdf: accessed 3 January 2016.

Lovely, P., E. Flodin, C. Guzofski, F. Maerten and D. D. Pollard., 2012, Pitfalls among the promises of mechanics-based restoration: addressing implications of unphysical boundary conditions: Journal of Structural Geology, v. 41, p.47-63.

Lu, H., D. W. Burbank and Y. Li, 2010a, Alluvial sequence in the north piedmont of the Chinese Tian Shan over the past 550 kyr and its relationship to climate change: Palaeogeography, Palaeoclimatology, Palaeoecology, v. 285, p. 343-353.

Lu, H., D. W. Burbank and Y. Li, and Y. Liu 2010b, Late Cenozoic structural and stratigraphic evolution of the northern Chinese Tian Shan foreland: Basin Research, 22(3), 249-269.

Maerten, L. and F. Maerten, 2006, Chronologic modeling of faulted and fractured reservoirs using geomechanically based restoration: technique and industry applications: AAPG Bulletin, v. 90(8), p. 1201–1226.

Magistrale, H. and S. Day, 1999, 3D Simulations of multi-segment thrust fault rupture, Geophys. Res. Lett., 26, 2093-2096.

Mallet, J. L., 1992, GOCAD: a computer aided design program for geological applications: Three-Dimensional Modeling with Geoscientific Information Systems: Springer, Netherlands, p. 123-141.

Marfurt, K. J., R. L. Kirlin, S. L. Farmer, and M. S. Bahorich, 1998, 3-D seismic attributes using a semblance-based coherency algorithm: Geophysics, v. 63(4), p. 1150-1165.

McClay, K. R., and P. G. Buchanan, 1992, Thrust faults in inverted extensional basins, in K. R. McClay ed., Thrust tectonics: Springer Netherlands, p. 93-104.

McClay, K. R., and P. G. Ellis, 1987, Geometries of extensional fault systems developed in model experiments: Geology, v. 15, p. 341-344.

Medwedeff, D. A., 1989, Growth fault-bend folding at southeast Lost Hills, San Joaquin Valley, California: AAPG Bulletin, v. 73, 54-67.

Medwedeff, D. A., 1992, Geometry and kinematics of an active, laterally propagating wedge thrust, Wheeler Ridge, California, in S. Mitra and G. Fisher eds., Structural Geology of Fold and Thrust Belts: John Hopkins Univ. Press, Baltimore, MD., p. 3-28.

Medwedeff, D.A. and J. Suppe, 1997, Multibend fault-bend folding: Journal of Structural Geology, v. 19(3), pp.279-292.

Molnar, P. and S. Ghose, 2000, Seismic moments of major earthquakes and the rate of shortening across the Tien Shan: Geophysical Research Letters, v. 27(16), p. 2377-2380.

Molnar, P., and P. Tapponier, 1975, Cenozoic tectonics of Asia: effects of a continental collision: Science, v. 189, p. 419-426.

Molnar, P., E. T. Brown, B. C. Burchfiel, Q. Deng, X. Feng, J. Li, G. M. Raisbeck, J. Shi, Z. Wu, F. Yiou, and H. You, 1994, Quaternary climate change and the formation of river terraces across growing anticlines on the north flank of the Tien Shan, China: The Journal of Geology, v. 102, p. 583-602.

Montgomery, S. L., 1998, Thirtyone Formation, Permian Basin, Texas: structural and lithologic heterogeneity in a Lower Devonian chert reservoir: AAPG Bulletin, v. 82(1), p. 1-24.

Mora, A., 2015, Petroleum systems of the Eastern Cordillera, foothill basins, and associated Llanos basin: impacts on the prediction of large scale foreland and foothill petroleum accumulations: AAPG Bulletin, v. 99(8), p. 1401-1406.

Moretti I., F. Lepage and M. Guiton, 2006, Kine3D: a new 3D restoration method based on a mixed approach linking geometry and geomechanics: Oil & Gas Science and Technology, v. 61(2), p. 277–289.

Morgan, J. K., 1999, Numerical simulations of granular shear zones using the distinct element method: 2. Effects of particle size distribution and interparticle friction on mechanical behavior. Journal of Geophysical Research: Solid Earth, 104(B2), pp.2721-2732.

Morgan, J. K., 2015, Effects of cohesion on the structural and mechanical evolution of fold and thrust belts and contractional wedges: discrete element simulations: Journal of Geophysical Research - Solid Earth, v. 120, p. 3870–3896.

Mount, V. S., K. W. Martindale, T. W. Griffith, and J. O. D. Byrd, 2011, Basement-involved contractional wedge structural styles: examples from the Hanna basin, Wyoming, in K. McClay, J. H. Shaw, and J. Suppe, eds., Thrust fault-related folding: AAPG Memoir 94, p. 271-282.

Mueller, K., J. Champion, M. Guccione, and K. Kelson, 1999, Fault slip rates in the modern New Madrid seismic zone: Science, v. 286(5442), p.1135-1138.

Muron, P. and J. L. Mallet, 2004, 3-D balanced unfolding and rock properties, in Proceedings of the 24th Gocad Meeting: Nancy, France, Association Scientifique pour la Geologie et ses Applications, 16 p.

Muron, P., 2005, Méthodes numériques 3D de restauration des structures géologiques faillées, Ph.D. Dissertation, Institut Polytechnique National de Lorraine, Nancy, France, 145 pp.

Murray, A. S. and Wintle, A.G., 2000, Luminescence dating of quartz using an improved single-aliquot regenerative-dose protocol: Radiation Measurements, v. 32, p. 57-73.

Nazareth, J. J., and E. Hauksson, 2004, The seismogenic thickness of southern California crust: BSSA, 94, 940-960.

Nelson, M. R., R. McCaffrey, P. Molnar, 1987, Source parameters for 11 earthquakes in the Tien Shan, Central Asia, determined by P and SH waveform inversion: Journal of Geophysical Research, v. 92(B12), p. 12629-12648.

Odling, N. E., P. Gillespie, B. Bourgine, C. Castaing, J. P. Chiles, N. P. Christensen, E. Fillion, A. Genter, C. Olsen, L. Thrane, and R. Trice, 1999, Variations in fracture system geometry and their implications for fluid flow in fractured hydrocarbon reservoirs: Petroleum Geoscience, v. 5(4), p. 373-384.

Plesch, A., J. H. Shaw and D. Kronman, 2007, Mechanics of low-relief detachment folding in the Bajiaochang field, Sichuan basin, China: AAPG Bulletin, v. 91(11), p. 1559–1575.

Plesch, A., J. H. Shaw, C. Benson, W. A. Bryant, S. Carena, M. Cooke, J. Dolan, G. Fuis, E. Gath, L. Grant, E. Hauksson, T. Jordan, M. Kamerling, M. Legg, S. Lindvall, H. Magistrale, C. Nicholson, N. Niemi, M. Oskin, S. Perry, G. Planansky, T. Rockwell, P. Shearer, C. Sorlien, P. Süss, J. Suppe, J. Trieman, and R. Yeats, 2007, Community fault model (CFM) for southern Califonia, BSSA, v. 97, p. 1793-1802.

Poblet, J., K. McClay, F. Storti, and J. A. Munoz, 1997, Geometries of syntectonic sediments associated with single layer detachment folds: Journal of Structural Geology, v. 19, p. 369–381.

Poisson, B. and J. P. Avouac, 2004, Holocene hydrological changes inferred from alluvial stream entrenchment in north Tian Shan (Northwestern China): The Journal of Geology, v. 112, p. 231-249.

Poisson, B., 2002, Impact du climat et de la tectonique sur l'évolution géomorphologique d'un piémont-Exemple du piémont Nord du Tian Shan depuis la fin du Pléistocène (Doctoral dissertation, Université Paris Sud-Paris XI).

Pope, M. C., 2014, High-resolution sequence stratigraphy of the Upper Ordovician Montoya Group, southern New Mexico and western Texas: outcrop analog of an unconventional chert and carbonate reservoir: AAPG Bulletin, v. 98(8), p. 1577-1597.

Pratt, T. L., J. H. Shaw, J. F. Dolan, S. Christofferson, R. A. Williams, J. K. Odum, and A. Plesch, 2002, Shallow folding imaged above the Puente Hills blind-thrust fault, Los Angeles, California: Geophysical Research Letters, v. 29, p. 18-1 - 18-4.

Rayner, J. M., 1985, Linear relations in biomechanics: the statistics of scaling functions: Journal of Zoology, v. 206(3), p. 415-439.

Rhodes, E. J., 2015, Dating sediments using potassium feldspar single-grain IRSL: initial methodological considerations: Quaternary International, v. 362, p.14-22.

Rich, J. L., 1934, Mechanics of low-angle overthrust faulting as illustrated by Cumberland thrust block, Virginia, Kentucky, and Tennessee: AAPG Bulletin, v. 18(12), pp.1584-1596.

Ritts, B. D., B. J. Darby and T. Cope, 2001, Early Jurassic extensional basin formation in the Daqing Shan segment of the Yinshan belt, northern North China Block, Inner Mongolia: Tectonophysics, v. 339, p. 239-258.

Rivero, C., and J. H. Shaw, 2011, Active folding and blind thrust faulting induced by basin inversion processes, inner California borderlands, in K. McClay et al. eds., Thrust Fault-Related Folding, AAPG Memoir 94, p. 187-214.

Rouby, D., H. Xiao and J. Suppe, 2000, 3-D restoration of complexly folded and faulted surfaces using multiple unfolding mechanisms: AAPG Bulletin, v. 84(6), p. 805-829.

Ruppel, S. C. and R. J. Barnaby, 2001, Contrasting styles of reservoir development in proximal and distal chert facies: Devonian Thirtyone Formation, Texas: AAPG Bulletin, v. 85(1), p. 7-33.

Ruppel, S. C. and S. D. Horvoka, 1995, Controls on reservoir development in Devonian chert, Permian Basin, Texas: AAPG Bulletin, v. 79(12), p. 1757-1785.

Saller, A., B. Ball, S. Robertson, B. McPherson, C. Wene, R. Nims, and J. Gogas, 2001, Reservoir characteristics of Devonian cherts and their control on oil recovery: Dollarhide field, west Texas: AAPG Bulletin, v. 85(1), p. 35-50.

Salomon-Mora, L. E., M. Aranda-Garcia, and J. R. Roman-Ramos, 2009, Contractional growth faulting in the Mexican Ridges, Gulf of Mexico, in C. Bartolini and J. R. Roman Ramos, eds., Petroleum Systems in the Southern Gulf of Mexico: AAPG Memoir 90, Tulsa, Oklahoma, p. 93–115.

Scharer, K.M., D. W. Burbank, J. Chen, R. J. Weldon, 2006, Kinematic models of fluvial terraces over active detachment folds: constraints on the growth mechanisms of the Kashi-Atushi fold system, Chinese Tian Shan: Geological Society of America Bulletin, v. 118(7-8), p. 1006-1021.

Schlische, R.W., R. H. Groshong, M. O. Withjack, and T. N. Hidayah, 2014, Quantifying the geometry, displacements, and subresolution deformation in thrust-ramp anticlines with growth and erosion: From models to seismic-reflection profile: Journal of Structural Geology, v. 69, p. 304-319.

Seeber, L. and C. C. Sorlien, 2000, Listric thrusts in the western Transverse Ranges, California: Geological Society of America Bulletin, v. 112(7), p. 1067-1079.

Shackleton, J. R. and M. L. Cooke, 2007, Is plane strain a valid assumption in non-cylindrical fault-cored folds?: Journal of Structural Geology, v. 29(7), p. 1229-1240.

Shaw, J. H. and J. Suppe, 1994, Active faulting and growth folding in the eastern Santa Barbara Channel, California: Geological Society of America Bulletin, v. 106, p. 607-626.

Shaw, J. H. and J. Suppe, 1996, Earthquake hazards of active blind-thrust faults under the central Los Angeles basin, California: Journal of Geophysical Research: Solid Earth, v. 101(B4), p. 8623-8642.

Shaw, J. H., A. Plesch, J. F.Dolan, T. Pratt, P. Fiore, 2002, Puente Hills blind thrust system, Los Angeles basin, California: BSSA, v. 92, p. 2946-2960.

Shaw, J. H., C. Connors, and J. Suppe, 2005, Seismic interpretation of contractional fault-related folds: An AAPG seismic atlas, AAPG Studies in Geology 53, 156 pp.

Shaw, J. H., F. Bilotti and P. A. Brennan, 1999, Patterns of imbricate thrusting: Geological Society of America Bulletin, v. 111(8), p. 1140-1154.

Shaw, J. H., F. Bilotti, and P. Brennan, 1999, Patterns of imbricate thrusting: Geological Society of America Bulletin, v. 111, p. 1140-1154.

Shaw, J. H., S. C. Hook, and E. P. Sitohang, 1997, Extensional fault-bend folding and synrift deposition: an example from the Central Sumatra Basin, Indonesia: AAPG Bulletin, v. 81, p. 367-379.

Shaw, J. H., S. C. Hook, and J. Suppe, 1994, Structural trend analysis by axial surface mapping: AAPG Bulletin, v. 78, p. 700-721.

Shokair, K. M., A. Plesch and J. H. Shaw, 2009, 3D structural restoration approach for fracture prediction – a case study from Kingdom of Saudi Arabia: in AAPG International Conference and Exhibition, Rio de Jan Janeiro, Brazil, AAPG, November 2009 (abs.).

Shumaker, R. C., 1992, Paleozoic structure of the Central Basin Uplift and adjacent Delaware Basin, West Texas: AAPG Bulletin, v. 76(11), p. 1804-1824.

Sibson, R. H., and G. Xie, 1998, Dip range for intracontinental reverse fault ruptures: truth stranger than friction?: Bulletin of the Seismological Society of America, v. 88, p. 1014-1022.

Sobel, E., 1999, Basin analysis of the Jurassic-Lower Cretaceous southwest Tarim basin, northwest China: Geological Society of America Bulletin, v. 111, p. 709-724.

Sobel, E., J. Chen, and R. V. Heermance, 2006, Late Oligocene-Early Miocene initiation of shortening in the Southwestern Chinese Tian Shan: implications for Neogene shortening rate variations, Earth and Planetary Science Letters, v. 247, p. 70-81, doi:10.1016/j.epsl.2006.03.048.

Stein, R. S., and G. C. P. King, 1984, Seismic potential revealed by surface folding: 1983 Coalinga, California, earthquake: Science, v. 224(4651), p. 869-872.

Stockmeyer, J. M., J. H. Shaw, and S. Guan, 2014, Seismic hazards of multisegment thrust-fault ruptures: insights from the 1906 M 7.4-8.2 Manas, China earthquake: Seismological Research Letters, v. 85, p. 801-808.

Strayer, L. M., and P. Hudleston, 1997, Numerical modeling of fold initiation at thrust ramps: Journal of Structural Geology, v. 19, p. 551–566.

Strayer, L. M., S. G. Erickson, and J. Suppe, 2004, Influence of growth strata on the evolution of fault-related folds—Distinct-element models: in K. R. McClay, ed., Thrust Tectonics and Hydrocarbon Systems: AAPG Memoir 82, p. 413– 437.

Suhm, R. W. and R. L. Ethington, 1975, Stratigraphy and conodonts of Simpson Group (Middle Ordovician), Beach and Baylor Mountains, West Texas: AAPG Bulletin, v. 59(7), p.1126-1135.

Suppe, J. and D. A. Medwedeff, 1990, Geometry and kinematics of fault-propagation folding: Eclogae Geologicae Helvetiae, v. 83(3), p. 409-454.

Suppe, J., 1983, Geometry and kinematics of fault-bend folding: American Journal of Science, v. 283, p. 684-721.

Suppe, J., C. D. Connors, Y. Zhang, 2004, Shear fault-bend folding, in McClay, K.R., ed., Thrust Tectonics and Hydrocarbon Systems: AAPG Memoir 82, p. 303-323.

Suppe, J., F. Sabat, J. Muñoz, J. Poblet, E. Roca, and J. Vergés, 1997, Bed-by-bed fold growth by kink-band migration: Saint Llorenç de Morunys, eastern Pyrenees, Journal of Structural Geology, v. 19, p. 443-461.

Suppe, J., G. T. Chou, and S. C. Hook, 1992, Rates of folding and faulting determined from growth strata, in K. R. McClay ed., Thrust Tectonics: Springer, p. 105- 121.

Tapponnier, P. and P. Molnar, 1979, Active faulting and Cenozoic tectonics of the Tien Shan, Mongolia, and Baykal regions: Journal of Geophysical Research, v. 84, p. 3425-3459.

Thompson, C. T., R. J. Weldon, C. M. Rubin, K. Abdrakhmatov, P. Molnar, and G. W. Berger, 2002, Late Quaternary slip rates across the central Tien Shan, Kyrgyzstan, central Asia: Journal of Geophysical Research, v. 107(B9), ETC 7-1–7-32.

Vidal-Royo, O., N. Cardozo, J. A. Muñoz, S. Hardy and L. Maerten, 2012, Multiple mechanisms driving detachment folding as deduced from 3d reconstruction and geomechanical restoration: the Pico del Águila anticline (External Sierras, Southern Pyrenees): Basin Research, v. 23, p. 1-19.

Wang, C. Y., Z. E. Yang, H. Luo, and W. D. Mooney, 2004, Crustal structure of the northern margin of the eastern Tien Shan, China, and its tectonic implications for the M~7.7 Manas earthquake: Earth and Planetary Science Letters, v. 223, p. 187-202.

Wells, D. L., and K. J. Coppersmith, 1994, New empirical relationships among magnitude, rupture length, rupture width, rupture area, and surface displacement, BSSA, v. 94, p. 974-1002.

Wesnousky, S. G., 2006, Predicting the endpoints of earthquake ruptures, Nature, v. 444, p. 358-360, doi:10.1038/nature05275.

Wesnousky, S. G., 2008, Displacement and geomechanical characteristics of earthquake surface ruptures: issues and implications for seismic-hazard analysis and the process of earthquake rupture, BSSA, v. 98, p. 1609-1632, doi:10.1785/0120070111.

Williams, G. D., C. M. Powel, and M. A. Cooper, 1989, Geometry and kinematics of inversion tectonics, in M. A. Cooper and G. D. Williams, eds., Inversion Tectonics: Geological Society Special Publication 44, p. 3–15.

Windley, B. F., M. B. Allen, C. Zhang, C., Z. Y. Zhao, and G. R. Wang, 1990, Paleozoic accretion and Cenozoic redeformation of the Chinese Tien Shan range, central Asia: Geology, v. 18, p. 128-131.

Xiang, B., N. Zhou, W. Ma, M. Wu, and J. Cao, 2015, Multiple stage migration and accumulation of Permian lacustrine mixed oils in the central Junggar basin (NW China): Marine and Petroleum Geology, v. 59, p. 187-201.

Xiao, H., and J. Suppe, 1992, Origin of rollover: AAPG Bulletin, v. 76, p. 509–525.

Xu, C. M., X. S. He, X. Z. Wu, and X. Y. Yao, 1992, Structure analysis and petroleum exploration prospect of Tostai area in Junggar Basin: Xinjing Petroleum Geology, v. 13, p. 197-205.

Yang, W., M. Jolivet, G. Dupont-Nivet, Z. Guo, Z. Zhang, and C. Wu, 2013, Source to sink relations between the Tian Shan and Junggar Basin (northwest China) from late Paleozoic to Quaternary: evidence from detrital U-Pb zircon geochronology: Basin Research, v. 25, p. 219-240.

Yeats, R. F., K. Sieh, and C. R. Allen, 1997, The geology of earthquakes, Oxford University Press, 568.

Yin, A., 2010, Cenozoic tectonic evolution of Asia: a preliminary synthesis: Tectonophysics, v. 488, p. 293-325.

Yin, A., S. Nie, P. Craig, T. M. Harrison, F. J. Ryerson, Q. Xianglin, and Y. Geng, 1998, Late Cenozoic tectonic evolution of the southern Chinese Tian Shan: Tectonics, v.17, p. 1-27.

Yue, L. F., J. Suppe, and J. H. Hung, 2005, Structural geology of a classic thrust belt earthquake: the 1999 Chi-Chi earthquake Taiwan (Mw = 7.6), Journal of Structural Geology, v. 27, p. 2058-2083.

Yue, L. F., J. Suppe, and J. H. Hung, 2011, Two contrasting kinematic styles of active folding above thrust ramps, Western Taiwan: in Thrust Fault Related Folding, eds. McClay K. et al.: Thrust Fault-Related Folding, AAPG Memoir 82, p. 413– 437.

Zhang, P., F. Mao, and D. B. Slemmons, 1999, Rupture terminations and the size of segment boundaries from historical earthquake ruptures in the Basin and Range Province: Tectonophysics, v. 308, p. 37-52.